

## The role of asymmetries in Nordic Seas dynamics

Ypma, S.L.

**DOI**

[10.4233/uuid:cbb5165a-7e9f-4416-97e1-010599c75324](https://doi.org/10.4233/uuid:cbb5165a-7e9f-4416-97e1-010599c75324)

**Publication date**

2020

**Document Version**

Final published version

**Citation (APA)**

Ypma, S. L. (2020). *The role of asymmetries in Nordic Seas dynamics*. [Dissertation (TU Delft), Delft University of Technology]. <https://doi.org/10.4233/uuid:cbb5165a-7e9f-4416-97e1-010599c75324>

**Important note**

To cite this publication, please use the final published version (if applicable).  
Please check the document version above.

**Copyright**

Other than for strictly personal use, it is not permitted to download, forward or distribute the text or part of it, without the consent of the author(s) and/or copyright holder(s), unless the work is under an open content license such as Creative Commons.

**Takedown policy**

Please contact us and provide details if you believe this document breaches copyrights.  
We will remove access to the work immediately and investigate your claim.

# **THE ROLE OF ASYMMETRIES IN NORDIC SEAS DYNAMICS**



# **THE ROLE OF ASYMMETRIES IN NORDIC SEAS DYNAMICS**

## **Proefschrift**

ter verkrijging van de graad van doctor  
aan de Technische Universiteit Delft,  
op gezag van de Rector Magnificus Prof. dr. ir. T.H.J.J. van der Hagen,  
voorzitter van het College voor Promoties,  
in het openbaar te verdedigen op  
woensdag 30 september 2020 om 12:30 uur

door

**Stefanie Leonore YPMA**

Master of Science in Meteorology, Physical Oceanography and Climate  
Universiteit Utrecht, Nederland  
geboren te Wijchen, Nederland.

Dit proefschrift is goedgekeurd door de

promotor: Prof. dr. J.D. Pietrzak en copromotor: dr. C.A. Katsman

Samenstelling promotiecommissie:

Rector Magnificus,	voorzitter
Prof. dr. J.D. Pietrzak,	Technische Universiteit Delft, promotor
Dr. C.A. Katsman,	Technische Universiteit Delft, copromotor

*Onafhankelijke leden:*

Dr. L. Chafik	University of Stockholm, Zweden
Prof. dr. A. Biastoch	GEOMAR Helmholtz-Zentrum für Ozeanforschung Kiel, Duitsland
Prof. dr. P.E. Isachsen	University of Oslo, Noorwegen
Prof. dr. ir. M. Verlaan	Technische Universiteit Delft
Prof. dr. ir. S.G.J. Aarninkhof	Technische Universiteit Delft, reservelid

*Overige leden:*

Prof. dr. H.A. Dijkstra	Universiteit Utrecht
-------------------------	----------------------



*Printed by:* Gildeprint

*Cover design:* Franke Margrete | [www.frankemargrete.nl](http://www.frankemargrete.nl)

Copyright © 2020 by S.L. Ypma

ISBN 978-94-6384-156-6

An electronic version of this dissertation is available at

<http://repository.tudelft.nl/>.

*Notre tête est ronde,  
pour permettre à la pensée de changer de direction*

Francis Picabia



# CONTENTS

<b>Samenvatting</b>	<b>ix</b>
<b>Summary</b>	<b>xiii</b>
<b>1 Introduction</b>	<b>1</b>
1.1 Global climate and the Nordic Seas . . . . .	3
1.2 General characteristics of the Nordic Seas. . . . .	5
1.2.1 Topographic features. . . . .	5
1.2.2 Hydrography and circulation . . . . .	5
1.2.3 Forcing mechanisms. . . . .	7
1.3 Watermass transformation processes . . . . .	8
1.3.1 Deep convection. . . . .	8
1.3.2 Interior-boundary current exchanges . . . . .	10
1.3.3 Difference between the Nordic Seas and the Labrador Sea. . . . .	11
1.4 Introduction to data and methods . . . . .	12
1.4.1 Observational records of the Nordic Seas . . . . .	12
1.4.2 Numerical ocean simulations . . . . .	13
1.4.3 Lagrangian methods . . . . .	14
1.5 Objectives and outline of this thesis. . . . .	18
<b>2 A two-basin conceptual model for the Nordic Seas</b>	<b>21</b>
2.1 Introduction . . . . .	22
2.2 Methods . . . . .	24
2.2.1 Idealized numerical model simulation of the Nordic Seas . . . . .	25
2.2.2 A conceptual model with one basin and a single boundary current . . . . .	28
2.3 Conceptual model for a two-basin marginal sea . . . . .	31
2.3.1 A two-basin approach without a frontal current . . . . .	31
2.3.2 A two-basin approach with a frontal current . . . . .	34
2.4 Sensitivity to atmospheric buoyancy forcing . . . . .	39
2.5 Discussion and conclusions. . . . .	42
2.A Appendix: sensitivity to non-uniform atmospheric forcing . . . . .	46
<b>3 Pathways of the NwAFC</b>	<b>51</b>
3.1 Introduction . . . . .	52
3.2 Methods . . . . .	54
3.2.1 Trajectories from observations . . . . .	54
3.2.2 Trajectories from a realistic ocean model . . . . .	55
3.2.3 Trajectories from an idealized numerical configuration . . . . .	56

3.3	Along- and across-frontal pathways. . . . .	58
3.4	Importance of frontal instability for watermass transformation. . . . .	62
3.5	Conclusions and discussion. . . . .	67
3.A	Appendix: heat exchange across the mid-ocean ridge. . . . .	70
<b>4</b>	<b>Pathways of the NIIC</b>	<b>77</b>
4.1	Introduction . . . . .	78
4.2	Methods . . . . .	81
4.2.1	Global ocean model configurations . . . . .	81
4.2.2	Tracking the Atlantic Water north through Denmark Strait. . . . .	82
4.3	Model performance in the Nordic Seas . . . . .	84
4.3.1	Hydrographic properties. . . . .	84
4.3.2	Nordic Seas Circulation . . . . .	86
4.3.3	Hydrographic properties at Kögur section . . . . .	87
4.4	Pathways of the NIIC watermass in the Nordic Seas. . . . .	89
4.5	Watermass transformation along the pathways . . . . .	94
4.5.1	Contribution of the NIIC water to overflow waters . . . . .	95
4.5.2	Location of watermass transformations . . . . .	98
4.6	Discussion and conclusions. . . . .	100
<b>5</b>	<b>Discussion and outlook</b>	<b>103</b>
5.1	Asymmetry in a two-basin marginal sea. . . . .	103
5.2	The Norwegian Atlantic Front Current . . . . .	105
5.3	The North Icelandic Irminger Current. . . . .	106
5.4	Overarching conclusions and discussion . . . . .	106
5.4.1	Revised circulation scheme of the Nordic Seas . . . . .	106
5.4.2	The importance of the hydrographic asymmetry. . . . .	108
5.4.3	The importance of the front current instability. . . . .	109
5.5	Outlook. . . . .	109
	<b>Bibliography</b>	<b>111</b>
	<b>Acknowledgements</b>	<b>125</b>
	<b>List of Publications</b>	<b>129</b>
	<b>About the author</b>	<b>131</b>

# SAMENVATTING

Het milde klimaat in Europa is voor een groot deel te danken aan oceaanstromingen die warm en zout water van de evenaar naar het noorden transporteren. Dit transport vindt plaats in de bovenste laag van de oceaan. Eenmaal in het noorden aangekomen vindt er een sterke koeling plaats door het grote contrast tussen de warme oceaan en de koude lucht erboven. Het water dat is afgekoeld heeft een hogere dichtheid en zal dus zinken. Diep in de waterkolom stroomt dit hoge dichtheidswater terug naar het zuiden. Deze zogenoemde Atlantische thermohaline circulatie wordt deels aangedreven door de wind en deels door de grote verschillen in temperatuur en zoutgehalte tussen de evenaar en de polen. Klimaatverandering in het noordpoolgebied leidt tot warmere en zoetere oceanen waardoor de aandrijving van de grootschalige oceaancirculatie verzwakt. Voornamelijk het proces dat het (warme) water met een lage dichtheid in het (koude) water met een hoge dichtheid verandert, is erg gevoelig voor veranderingen in atmosferische temperaturen en zoet water in de waterkolom. De regio waar deze thesis op focust is de regio waar een groot deel van deze transformaties plaatsvindt; de Europese Noordzee. Deze zee ligt tussen Groenland en Noorwegen en bestaat uit diverse sub-zeeën, zoals de Groenlandse Zee, de Noorse Zee en de IJslandse Zee. Het doel van dit proefschrift is om de dynamische processen die een rol spelen in de transformatie van warm naar koud in de Europese Noordzee beter te begrijpen.

Geografisch heeft de Europese Noordzee een bijzondere positie, gezien via deze zee de voornaamste uitwisseling tussen de Atlantische Oceaan en de Arctische Oceaan (de Noordelijke IJszee) plaatsvindt. Ten oosten van IJsland komt warm en zout water vanuit de Atlantische Oceaan de Europese Noordzee binnen. Vanuit het noorden stroomt koud en zoet water door de Fram Straat tussen Groenland en Spitsbergen. Als gevolg hiervan is er een grote asymmetrie in de zout- en temperatuurverdeling in de Europese Noordzee; in het oosten is het water warm en zout (de Noorse Zee), in het westen koud en zoet (de Groenlandse Zee). Menging tussen deze watermassa's wordt beperkt door een topografische richel, als het ware een onder water gelegen bergkam, die van zuid naar noord dwars door de Europese Noordzee loopt. Net als voor de globale oceaan, spelen deze verschillen in temperatuur en zoutgehalte een belangrijke rol voor de circulatie en mengprocessen in de Europese Noordzee. Het water dat de Europese Noordzee uiteindelijk verlaat richting de Atlantische Oceaan heeft een erg hoge dichtheid en vormt daardoor een belangrijke connectie met de thermohaline circulatie.

In het eerste deel van dit proefschrift wordt onderzocht hoe de hydrografie en circulatie beheerst worden door dynamische processen in de Europese Noordzee. Hiervoor is een theoretisch raamwerk ontwikkeld, gebaseerd op de wet van energie- en massabehoud. Voorheen is een vergelijkbare aanpak gebruikt om eenvoudige verbanden te kunnen herleiden tussen de sterkte van de atmosferische koeling, de temperatuur van het zeewater en de warmteflux van stromingen en wervels. Echter werd als referentie vaak een oceaan zoals de Labradorzee gebruikt, gekarakteriseerd door een enkel bassin met

een enkele stroming langs de kust. Om de hydrografische asymmetrie van de Europese Noordzee correct weer te geven zijn op zijn minst twee bassins nodig. Daarnaast loopt de stroming niet alleen langs de kusten van Noorwegen en Groenland, maar ook langs het dichtheidsfront tussen oost en west. Het nieuwe theoretische raamwerk neemt deze aspecten mee en laat zien dat de Noorse Zee en de Groenlandse Zee niet gelijkwaardig reageren op veranderingen in de sterkte van de atmosferische koeling. Hierdoor is het dichtheidsverschil tussen oost en west niet constant, wat gevolgen heeft voor de stroomsnelheid langs het front. Gezien de response van de oceaan niet uniform is, zijn er twee atmosferische regimes aan te duiden waar de veranderingen in oceaanstromingen en hydrografie tegengesteld zijn voor dezelfde verandering in atmosferische koeling. De resultaten duiden daarom het belang aan om te weten in welk regime de huidige Europese Noordzee zit om te kunnen voorspellen hoe het systeem reageert op klimaatveranderingen.

De afgeleide verbanden in het eerste deel van dit proefschrift laten ook de belangrijke rol van het dichtheidsfront zien. Niet alleen blijkt de stroming langs het front een connectie te vormen met de stroming langs de kust, het front kan ook een bron van warmte zijn voor het binnenste van de bassins ten oosten en westen van het front via wervels. Deze wervels, en de daarbij behorende warmteflux, worden gevormd door de onstabiele van het front. Deze uitwisseling tussen de grensstromingen en het binnenste van de bassins heeft gevolgen voor de transformatie van warm naar koud. Het is daarom belangrijk om te begrijpen welke paden het warme Atlantische water neemt door de Europese Noordzee. Deze paden en de mogelijke uitwisselingen met gebieden buiten deze paden kunnen nader onderzocht worden door gebruik te maken van een Lagrangiaanse methode. Dit betekent dat de eigenschappen van het water worden geanalyseerd in een bewegend referentiekader, de stroming volgend, in plaats van op vaste geografische posities.

In het tweede deel van dit proefschrift wordt de route geanalyseerd van het water dat ten oosten van IJsland de Europese Noordzee instroomt en vervolgens langs het front naar het noorden stroomt. Hiervoor worden ARGO robotsondes en drijfboeien bestudeerd die in de buurt van het front komen. Beide instrumenten drijven met de stroming mee en hun posities worden opgeslagen door gebruik te maken van een satelliet. Hierdoor kunnen drijfboeien informatie verschaffen over de circulatie aan het oppervlak, en ARGO robotsondes over stromingen dieper in de waterkolom. Er hebben tot op heden maar een paar honderd van deze instrumenten door de Europese Noordzee gedreven, en slechts tientallen zijn in de buurt gekomen van het front zelf. Om de significantie van de resultaten te bepalen, zijn ook numerieke deeltjes geanalyseerd die virtueel stromen door de snelheidsvelden van oceaansmodellen. Gebruik makend van beide datasets is duidelijk geworden dat het pad langs het front wordt gevormd door een sterk onderbroken stroming, niet de continue stroming die tot op heden altijd wordt weergegeven op schematische stromingskaarten. Er vindt veel uitwisseling plaats tussen de stroming langs de kust van Noorwegen en de stroming langs het front. Dit impliceert een afhankelijkheid tussen deze twee stromingen, welke invloed heeft op de propagatie van eigenschappen van de Atlantische Oceaan naar de Arctische Oceaan. Ook geven de geanalyseerde paden informatie over de onstabiele van het front en de uitwisseling tussen de Noorse Zee en de Groenlandse Zee. De resultaten duiden aan dat het warme water dat

langs het onstabiele front stroomt transformeert naar kouder en zoeter water dan het warme water dat het pad langs de Noorse kust volgt.

In het laatste deel van dit proefschrift worden de verschillende paden onderzocht van water dat ten westen van IJsland de Europese Noordzee instroomt. Tot nu toe werd aangenomen dat dit water sterk wordt afgekoeld ten noorden van IJsland, van richting verandert, en zodoende de belangrijkste bron vormt voor de Noord IJslandse Onderstroom; een stroming met een erg hoge dichtheid die de Europese Noordzee verlaat door de zeestraat tussen Groenland en IJsland. In dit proefschrift wordt deze warme watermassa die naar binnen stroomt gevolgd door opnieuw gebruik te maken van virtuele deeltjes in twee realistische oceaan modellen. De resultaten laten zien dat maar een klein deel van deze stroming verbonden is met de Noord IJslandse Onderstroom. Het overgrote deel van de stroming volgt verschillende paden door de Europese Noordzee, waar de vervolgroute afhangt van de transformatieprocessen ten noorden van IJsland. Een analyse van de realistische oceaanmodellen die worden gebruikt voor deze studie laat zien dat de kwaliteit van de representatie van de Europese Noordzee sterk afhankelijk is van de configuratie van het model. In deze studie leiden verschillen in de koppeling tussen de oceaan en het zeeijs tot grote verschillen in hydrografie en paden voor het Atlantische water.

Een van de grootste uitdagingen is dan ook het ontwikkelen van een klimaatmodel met een correcte representatie van de Europese Noordzee, om uiteindelijk te begrijpen hoe horizontale en verticale processen bijdragen aan de transformatie van het warme Atlantische water dat de diepe stroming van de thermohaline circulatie aandrijft. Resultaten gepresenteerd in dit proefschrift tonen aan dat het Atlantische water op verschillende manieren van dichtheid kan veranderen, afhankelijk van het pad dat het water neemt door de Europese Noordzee. Ook laten de resultaten zien dat de asymmetrische eigenschappen van de Europese Noordzee een belangrijke rol spelen voor de gevoeligheid van deze regio voor veranderingen in de atmosfeer. Een realistische voorspelling van hoe de transformatieprocessen zullen reageren op klimaatveranderingen kan daarom alleen bereikt worden als klimaatmodellen de paden van het Atlantische water en de hydrografische asymmetrie in de Europese Noordzee correct weergeven en als onderzocht wordt welke transformatieprocessen in welk gebied dominant zijn.



# SUMMARY

The oceanic transport of heat and salt from the equator northward is one of the main reasons for the mild climate of Europe. This transport occurs in the upper layer of the ocean. In the north, strong cooling occurs due to the large difference in temperature between the ocean surface and the atmosphere. The cooled watermass has a higher density and therefore sinks and returns toward the south at depth. This so-called Atlantic Meridional Overturning Circulation is driven in part by the wind and in part by the difference in temperature and salinity between the equator and the poles. Polar climate change will result in warmer and fresher oceans which will likely weaken this global overturning circulation. Especially processes that concern the transformation from the light (warm) watermasses to dense (cold) watermasses are sensitive to changes in buoyancy forcing. This thesis focuses on an area where a large part of this transformation from light to dense watermasses takes place; the Nordic Seas. The Nordic Seas are located between Greenland and Norway and consist of several sub-basins, like the Lofoten Basin, the Greenland Basin and the Norwegian Basin. The main aim of this thesis is to better understand the dynamical processes involved in the watermass transformation in the Nordic Seas.

Geographically, the Nordic Seas are important as they provide the main passageway between the Atlantic Ocean and the Arctic Ocean. East of Iceland, a warm and saline watermass enters the Nordic Seas from the Atlantic Ocean. From the north, fresh and cold watermasses enter through Fram Strait between Greenland and Svalbard. As a consequence, the Nordic Seas display a large hydrographic asymmetry; the east is warm and salty (the Lofoten and Norwegian Basins), the west is cold and fresh (the Greenland Basin). Mixing between these regions is limited due to the presence of a mid-ocean ridge (an underwater mountain range), that cuts through the Nordic Seas from south to north. Similar to the global ocean, these temperature and salinity differences play an important role for the circulation and mixing processes in the Nordic Seas. The watermass that eventually leaves the Nordic Seas toward the Atlantic Ocean has a very high density and contributes significantly to the lower branch of the Atlantic Meridional Overturning Circulation.

The first part of this thesis addresses how the hydrography and circulation of the Nordic Seas are controlled by dynamical processes. A conceptual model is developed by deriving a buoyancy budget for the Nordic Seas. Previously, a similar approach has been used to obtain theoretical relations between the atmospheric forcing, the temperature of the ocean and the heat flux carried by the mean velocity field and by eddies. However, these conceptual models were based on a marginal sea like the Labrador Sea, which is characterized by a single basin and a single boundary current. To capture the hydrographic asymmetry of the Nordic Seas, at least two basins are needed. Furthermore, in addition to the boundary current along Norway and Greenland, a front current exists flowing northward along the mid-ocean ridge. The newly derived conceptual model in-

corporates this two-basin approach and shows that the eastern (Lofoten) basin and the western (Greenland) basin respond differently to changes in atmospheric buoyancy forcing. Consequently, the density difference between east and west is not constant which in turn impacts the strength of the front current. Due to the non-uniform response of the two-basin marginal sea to changes in atmospheric forcing, there are two different atmospheric regimes where the response of the circulation and hydrography is opposite for the same amount of change in forcing. Therefore, the results indicate that it is important to understand in which regime the Nordic Seas presently are, in order to predict their response to climate change.

The results of the conceptual model also show the importance of the front. Not only do they suggest a correlation between the front current and the slope current, the front can also form a source of heat for the interior through eddy fluxes. These eddies and the associated heat flux are a result of the instability of the front. The associated exchange between the boundary and the interior is important for watermass transformations. It is therefore essential to know which pathways Atlantic Water takes through the Nordic Seas. These Atlantic Water pathways and the exchange between boundary and interior can be studied in detail using a Lagrangian approach. This means that the properties of the water are analyzed in a moving frame of reference, following the flow, instead of at fixed positions.

In the second part of this thesis, the pathways of Atlantic Water entering the Nordic Seas east of Iceland are analyzed that continue their path to the north along the front. In order to do so, trajectories of ARGO floats and surface drifters are used that have come near the mid-ocean ridge. Both instruments drift with the flow and their positions are recorded using satellites. Therefore, the surface drifters provide information about the surface circulation and the ARGO floats provide information about the circulation at mid-depth. Up until now, a few hundred floats and drifters have been in the Nordic Seas, but only a few came close to the mid-ocean ridge. In order to corroborate the results from the observational floats, the data set is extended by trajectories of numerical particles that were released in the 3D velocity fields of ocean simulations. Results from both the observational and numerical floats indicate that the flow along the front is not as continuous as it is often schematized in circulation maps of the Nordic Seas. Instead, flow exchange occurs between the front current and the slope current along the continental slope of Norway. This means that these flows are not independent, which impacts the propagation of anomalies from the Atlantic Ocean to the Arctic Ocean. Furthermore, the trajectories provide information on the frontal current instability and the exchange between the Lofoten and the Greenland Basins. The results indicate that the transformation along the unstable front leads to colder and fresher watermasses than the transformation along the slope current.

The third part of this thesis investigates the pathways of the Atlantic Water that enters the Nordic Seas west of Iceland. It is assumed that this watermass is strongly cooled north of Iceland, changes direction and provides the main source of dense water for the North Icelandic Jet; the densest watermass leaving the Nordic Seas through Denmark Strait. In this thesis, this pathway is traced using numerical particles in two realistic ocean models. The results show that only a small part of the warm watermass is connected to the North Icelandic Jet. The remainder continues its path to the east along the

coast of Iceland, where the fate of the pathway is controlled by transformation processes north of Iceland. Validation of the two ocean models shows that the ability of these models to correctly represent the Nordic Seas strongly depends on the model configuration. In this study, the differences in the sea-ice configurations lead to differences in hydrography and Atlantic Water pathways.

Therefore, in order to fully understand the zonal and meridional processes contributing to the watermass transformation in the Nordic Seas, one of the main challenges is to develop a model that correctly represents this region. The results presented in this thesis show the importance of the Atlantic Water pathways through the Nordic Seas for its transformation to dense waters that contribute to the Atlantic Meridional Overturning Circulation. Furthermore, the results indicate that the asymmetric properties of the Nordic Seas play a key role in the sensitivity of this region to changes in the environment. Therefore, meaningful predictions of future changes in the Nordic Seas can only be achieved by a correct representation of the Atlantic Water pathways and the hydrographic asymmetry and by an improved understanding of which watermass transformation processes are dominant where.



# 1

## INTRODUCTION

*Learn how to mark the movements of the ocean and to discern how its turmoil ebbs and swells; for that is knowledge which all must possess who wish to trade abroad.*

The King's mirror, AD1250

*Wise words from a father to his son written in a 13th century Norwegian manuscript. The importance of trade, the presence of rich fish stocks in Norwegian waters and Vikings' nature to explore, all drove an early understanding of Nordic Seas climate and circulation. Nested between Greenland and Norway, the Nordic Seas form the main connection between the Atlantic Ocean and the Arctic Ocean. This connection is important, as nowadays the motivation to 'learn' is no longer driven by local socio-economic reasons, but by a global interest as oceanographers became aware of the importance of Nordic Seas processes for the global climate. Despite the early knowledge on the main circulation and the rather large observational data set compared to other regions, there are still many questions regarding the origin and variability of watermasses leaving the Nordic Seas and the response of the Nordic Seas to climate change. This thesis contributes to understanding of the Nordic Seas in light of the predicted global warming, in particular by investigating processes that control the connection between boundary currents and basin interiors. This introductory chapter elaborates on the importance of the Nordic Seas for local and global climate and provides a description of the main characteristics of the region. This is followed by an explanation of the main processes and methods on which this thesis builds. The research questions, including their motivation, are introduced and an outline of this thesis is provided.*

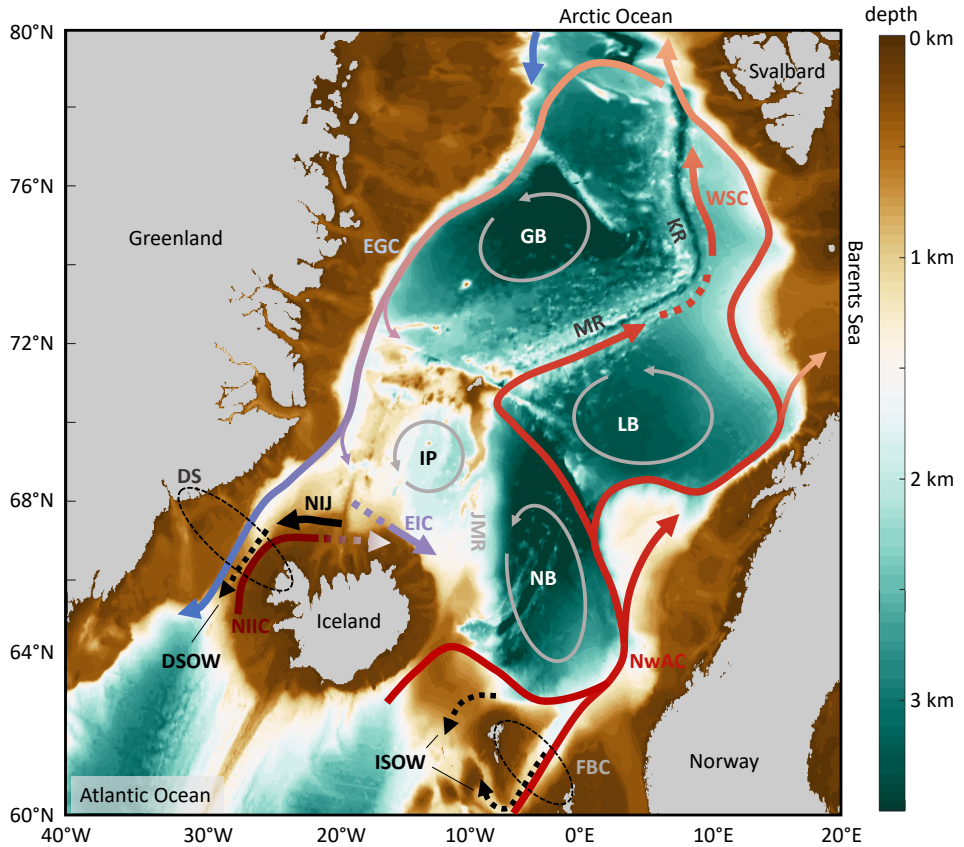


Figure 1.1: Schematic overview of the circulation in the Nordic Seas (arrows) and bathymetry (shading, from ETOPO1, *Smith and Sandwell*, 1997). Shown in red are the warm and salty inflowing currents: the North Icelandic Irminger Current (NIIC), the Norwegian Atlantic Current (NwAC) and its continuation, the West Spitsbergen Current (WSC). Blue and black lines indicate the fresh and cold returning currents and the overflows: the East Greenland Current (EGC), the East Icelandic Current (EIC), the North Icelandic Jet (NIJ), the Denmark Strait Overflow Water (DSOW) and the Iceland Scotland Overflow Water (ISOW). Abbreviations for bathymetric features and regions are: the Norwegian Basin (NB), the Lofoten Basin (LB), the Greenland Basin (GB), the Icelandic Plateau (IP), Denmark Strait (DS), Faroe Bank Channel (FBC), the Jan Mayen Ridge (JMR), the Mohn Ridge (MR) and the Knipovich Ridge (KR).

## 1.1. GLOBAL CLIMATE AND THE NORDIC SEAS

Bounded by Norway and Greenland in the zonal direction and Iceland and Svalbard in the meridional direction (Figure 1.1), the Nordic Seas consist of four sub-basins; the Norwegian Sea, the Lofoten Basin, the Greenland Basin and the Icelandic Plateau (together sometimes referred to as the GIN-Seas). As they are connected to the Atlantic Ocean and to the Arctic Ocean, the Nordic Seas form a buffer zone between the warm and saline watermasses from the south and the cold and fresh watermasses from the north. The watermass that enters the Nordic Seas from the south (the Atlantic Water, AW) is anomalously warm compared to ocean watermasses at similar latitudes (*Rahmstorf and Ganopolski, 1999*). As such, the presence of AW gives rise to various processes important for local and global climate.

Locally, the Norwegian waters owe their rich fish stocks to the warm and nutrient rich AW layer (e.g. *Helland-Hansen and Nansen, 1909; Skogen et al., 2007*). This is one of the reasons why Norway was the first country to have a separate Ministry of Fisheries and why nowadays, the country is the second largest exporter of fish in the world (e.g. *Johansen et al., 2019*). With climate change, warm anomalies within the AW layer can propagate further north (*Spielhagen et al., 2011*). As these temperature anomalies are linked to the presence of specific fish species, understanding of how the AW propagates can provide insight to where certain fish species will likely thrive (*Årthun et al., 2018*).

Another motivation to study pathways of AW in the Nordic Seas, is its potential to melt sea ice and ice sheets. Sea-ice melt is mainly driven by atmospheric forcing as the sea ice is isolated from the warm AW layer below by a layer of fresh and cold water. However, when sea ice is lost, the stratification erodes and the AW, now able to reach the surface, amplifies the ice melt (*Onarheim et al., 2014; Carmack et al., 2015; Polyakov et al., 2017*). Also submarine melt, an important process leading to the retreat and acceleration of Greenland outlet glaciers, is driven by the presence of AW (*Hanna et al., 2009; Straneo et al., 2010; Straneo and Heimbach, 2013*). As melt from Greenland has the potential to raise the sea level, it is important to understand the propagation of AW toward these fjords (e.g. *Gelderloos et al., 2017*).

In addition to its effect on ice, the transport of warm waters into the Nordic Seas also impacts the climate on land. Especially in winter, the heating of the atmosphere by the ocean can exceed that from solar net radiation and as such affect the climate downwind (*Rhines et al., 2008*). Recent analysis of observational records has shown that the climate variability of North Western Europe and the Arctic can be predicted up to a decade in advance, by measuring the heat anomalies within the ocean (*Årthun et al., 2017*). So, the properties and pathways of the Atlantic Water in the Nordic Seas are important locally, for climate and economy, and also remotely via their role for sea-ice melt and sea-level rise.

On an even larger scale, the warm and saline Atlantic Water that enters the Nordic Seas, returns to the Atlantic Ocean as either light and fresh surface waters or as dense and cold overflow waters. The corresponding processes that lead to these water mass transformations are of immense importance for the global ocean circulation and climate. This thesis mainly focuses on the latter transformation, from Atlantic Water to the formation of the overflows. The Atlantic Water that flows into the Nordic Seas is part of the upper limb of the Atlantic Meridional Overturning Circulation (AMOC). The AMOC

is responsible for the ventilation of the upper 2000 m of the Atlantic Ocean by bringing warm and saline water across the equator to the north. Cooling in the north transforms the watermasses to denser waters, which sink and return south at depth to form the lower limb of the AMOC. The AMOC is the main mechanism that stores heat and CO<sub>2</sub> in the deep ocean (e.g. *Levitus et al.*, 2005; *Takahashi et al.*, 2009) and, as it redistributes heat, its strength and variability impact global climate in various ways.

On average, the Northern Hemisphere is slightly warmer than the Southern Hemisphere due to the northward transport of heat by the AMOC (*Buckley and Marshall*, 2016). Furthermore, dense water formation processes impact the sea level, explaining for example the lower sea level in the northern Atlantic compared to the northern Pacific (e.g. *Wijffels et al.*, 1992; *Levermann et al.*, 2005). On short timescales, the AMOC variability causes sea surface temperature changes in the Atlantic Ocean (e.g. *Buckley and Marshall*, 2016), but on longer timescales, the AMOC is known to be bistable (*Stommel*, 1961). Abrupt climate shifts in the past have been linked to changes in the AMOC, or even a shutdown of the circulation (e.g. *Kuhlbrodt et al.*, 2007; *Henry et al.*, 2016). For the coming century, many modeling studies predict a slowdown of the AMOC due to anthropogenic forcing (e.g. *Rahmstorf et al.*, 2015).

However, these models show considerable differences in their representation of both the strength and variability of the AMOC (*Danabasoglu et al.*, 2014). In order to monitor changes in the AMOC and to provide a validation of the models, measuring arrays have been installed across the Atlantic Ocean. Measurements from the RAPID array, installed in March 2004 at 26.5°N, reveal a large variability of the AMOC on multiple time scales, which are not yet fully understood (*Rayner et al.*, 2011). More recently, data has been analyzed from the OSNAP array. This array was completed in August 2014 and ranges from Scotland to the southern tip of Greenland and across the Labrador Sea. First results suggest that the transformation processes taking place in the northeastern part of the Atlantic Ocean are the main driver of the AMOC variability, instead of processes in the Labrador Sea as previously thought (*Lozier et al.*, 2019).

*Chafik and Rossby* (2019) showed that especially processes within the Nordic Seas play a major role for the strength of the AMOC, as more than 60% of the total heat loss in the northern North Atlantic Ocean is estimated to occur in this region. The Nordic Seas are linked to the AMOC via the inflow of AW from the south and via the overflow of dense water back to the Atlantic Ocean. The transport of the overflows and the subsequent entrainment of lighter waters on its way south, adds up to about two-thirds of the lower limb of the AMOC (*Hansen and Østerhus*, 2000). In addition, the formation of the overflows is accompanied by a persistent low sea level in the Nordic Seas. This creates a pressure gradient that in part drives the inflow of warm waters into the Nordic Seas (*Hansen et al.*, 2010). The formation of the overflow waters mainly occurs by the transformation of the AW inflow into the Nordic Seas (*Mauritzen*, 1996; *Eldevik et al.*, 2009) and in part by deep convection processes in the interior of the Nordic Seas (*Eldevik et al.*, 2005; *Messias et al.*, 2008; *Våge et al.*, 2015, see also section 1.3). It is therefore important to understand the physical mechanisms involved in dense water formation and the subsequent pathways of this watermass in the Nordic Seas, as these processes play a key role in the response of the climate to anthropogenic forcing.

## 1.2. GENERAL CHARACTERISTICS OF THE NORDIC SEAS

As seen in the previous section, the pathways and watermass transformation of Atlantic Water in the Nordic Seas are important for the global ocean circulation and climate. However, due to lack of observational data and insufficient resolving capacity of climate models (see section 1.4), there are still many uncertainties regarding the connection between the warm inflow and the dense overflow in the Nordic Seas. This section provides a short summary of the topographic features, hydrography, circulation and forcing mechanisms of the Nordic Seas.

### 1.2.1. TOPOGRAPHIC FEATURES

The topography in the Nordic Seas is rather complex and is shown in Figure 1.1. In the south, the Greenland-Scotland Ridge (GSR) forms a barrier between the Atlantic Ocean and the Nordic Seas. As such, the inflow and outflow are mainly confined to the deeper passages across this ridge: the Denmark Strait (620 m depth) and the Faroe Bank Channel (840 m depth, *Hansen and Østerhus, 2000*). Within the Nordic Seas, a continuation of the Mid-Atlantic Ridge separates the east from the west; the Kolbeinsey Ridge, the Mohn Ridge and the Knipovich Ridge. The mean depth of these ridges varies from 1000 m to 2000 m, but the topography is rough and there are many deep gaps and large peaks (see Figure 1.1). In combination with the Jan Mayen- Ridge and Fracture Zone, the submarine ridges divide the Nordic Seas in four sub-basins; The Norwegian Basin and the Lofoten Basin in the east, and the Greenland Basin and the Icelandic Plateau in the west. Apart from the latter, these basins are more than 3000 m deep. To the north, the Nordic Seas are connected to the Barents Sea via the Barents Sea Opening and to the Arctic Ocean via Fram Strait. The topographic slopes along the continental shelves are steep, especially near the Lofoten Islands. Together with the topographic structure discussed above, this feature plays an important role in setting the hydrographic zonal asymmetry and circulation in the Nordic Seas as discussed in the next section.

### 1.2.2. HYDROGRAPHY AND CIRCULATION

What makes the Nordic Seas unique in comparison to other marginal seas like the Labrador Sea is its large hydrographic asymmetry. The eastern basins, the Lofoten and Norwegian Basins, are largely affected by the inflow of Atlantic Water from the south and are therefore relatively warm and saline. The western basins, the Greenland Basin and Icelandic Plateau, are colder and fresher as they are influenced by watermasses coming from the Arctic Ocean (Figure 1.2a, e.g. *Hansen and Østerhus, 2000*).

The main inflow of Atlantic Water into the Nordic Seas occurs along two branches east of Iceland that form the Norwegian Atlantic Current (NwAC, red arrows in Figure 1.1). Warm-core anticyclonic eddies spread the AW through the eastern basin, providing a source of heat to the interior while at the same time cooling the boundary current. These eddies originate from the NwAC near the Lofoten Islands. There, the continental slope steepens which increases the instability of the boundary current (see also section 1.3.2). The newly-formed eddies travel in a cyclonic direction through the Lofoten Basin, but are blocked by the Mohn and Knipovich Ridges. In the centre of the Lofoten Basin these eddies can merge and form a semi-permanent anticyclonic vortex (e.g. *Köhl, 2007*). As the eddies cannot cross the mid-ocean ridges, a warm AW layer of 500 m thickness

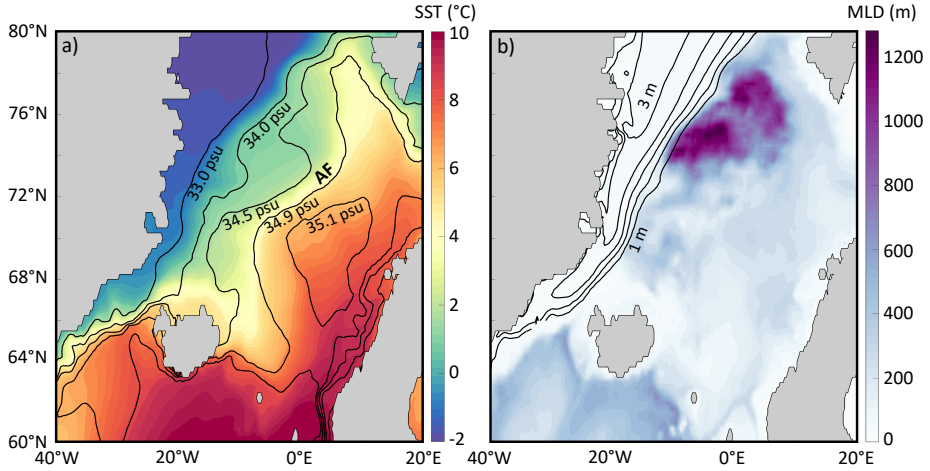


Figure 1.2: (a) Sea surface temperature (shading) and sea surface salinity (contours) averaged over years 1993-2015. (b) March mixed layer depth (shading) and sea-ice thickness (contours) averaged over years 1993-2015. The 34.9 psu isohaline denotes the location Arctic Front (AF). Data is obtained using the GLORYS reanalysis product (GLOBAL\_REANALYSIS\_PHY\_001\_025) from the EU Copernicus Marine Services (<https://marine.copernicus.eu>).

is confined to the eastern basin. The strong density front aligned with the mid-ocean ridges is called the Arctic Front (AF, Figure 1.2a).

The separation of the warm and saline watermass in the east from the cold and fresh watermass in the west by the mid-ocean ridges has various consequences. The warm surface layer in the east does not allow sea-ice formation and hence sea ice can only be found in the western basins. Furthermore, due to this hydrographic asymmetry, the NwAC has a two-branch structure. The Norwegian Atlantic Slope Current (NwASC, hereinafter ‘slope current’) follows the continental slope of Norway and transports  $\sim 3.4$  Sv of AW (Hansen and Østerhus, 2000,  $1 \text{ Sv} = 10^6 \text{ m}^3 \text{ s}^{-1}$ ). Due to the negative horizontal density gradient across the AF, geostrophy requires a northward flow along the front; the Norwegian Atlantic Front Current (NwAFC, hereinafter ‘front current’). Although previously estimated to be rather weak, direct measurements indicated a front current transport of  $\sim 3.2$  Sv (Bosse and Fer, 2019). As such, the front current forms an equally important pathway for AW as the slope current. In addition to these two branches, a small portion of AW,  $\sim 1$  Sv, enters the Nordic Seas west of Iceland within the North Icelandic Irminger Current (NIIC), which follows the Icelandic slope toward the northeast (Jónsson and Valdimarsson, 2005).

On its way northward, part of the AW watermass flows into the Barents Sea or into the Arctic Ocean. However, about half of the AW recirculates within Fram Strait (Marnele et al., 2013) and returns south at depth as part of the East Greenland Current. This watermass is often referred to as the Returning Atlantic Water (RAW) as it is colder and fresher than the original AW inflow. The upper layer of the EGC is characterized by the fresh and cold Polar Waters (PW) from the Arctic Ocean. Together with the East Green-

land Continental Current, the EGC forms the main pathway for light watermasses that leave the Nordic Seas through Denmark Strait.

The densest watermasses leave the Nordic Seas via the overflows. As already addressed in section 1.1, the overflows contribute significantly to the lower limb of the AMOC. Any watermass denser than  $1027.8 \text{ kg m}^{-3}$  is commonly defined as being overflow water. About half of the total overflow transport,  $\sim 3.2 \text{ Sv}$ , takes place through Denmark Strait; the Denmark Strait Overflow Water (DSOW, e.g. *Jochumsen et al.*, 2017). Assuming that the flow through the strait is controlled hydraulically, the volume flux of DSOW depends on the density difference up- and downstream of the sill and on the height difference between the DSOW and the sill depth (e.g. *Köhl et al.*, 2007). The other half of the overflow transport takes place between Iceland and Scotland, mainly through the Faroe Bank Channel (see Figure 1.1). Pathways of the overflow after leaving the Nordic Seas are studied by e.g. *Lozier et al.* (2013), but their variability and origin are still a matter of debate (see section 1.3).

### 1.2.3. FORCING MECHANISMS

The circulation in the Nordic Seas (and in the global oceans) is driven by wind forcing and buoyancy forcing (e.g. *Gill*, 1982). Wind exerts a stress on the sea surface, which can cause mixing and can drive large-scale gyre circulations. As such, wind input is mainly a mechanical source of energy. In contrast, buoyancy forcing can provide potential energy by changing temperature or salinity properties at the sea surface that are mixed downward. Examples of buoyancy forcing are incoming short-wave solar radiation (heating) and ice melt (decreasing salinity) or formation (increasing salinity via brine rejection).

Although often studied separately, wind forcing and buoyancy forcing are not independent of each other. Wind-induced mixing can propagate density variations at the surface to deeper layers and wind itself can change density at the sea surface via cooling or evaporation. In turn, the strength of the stratification dictates to what extent the wind can impact deeper layers in the water column. In areas of weak stratification, like in the interior basins of the Nordic Seas, wind variations are the dominant mechanism for the flow variability (*Isachsen et al.*, 2003). Despite the fact that these interior basins are very deep, the momentum over the full water column is sustained by the wind stress (*Nøst and Isachsen*, 2003) where  $f/H$  contours are closed, and therefore, even the surface circulation is strongly influenced by topography.

As the Nordic Seas are characterized by a positive wind stress curl, each basin supports a cyclonic gyre circulation (Figure 1.1). Where the  $f/H$  contours are no longer closed, buoyancy forcing becomes important. Especially the separation of the NwAC into a front current and a slope current can only be explained when including the thermal wind shear in addition to the wind stress. *Nøst and Isachsen* (2003) showed that using only wind stress and thermal wind shear, the resulting circulation compares remarkably well with the observed velocity field in the Nordic Seas; near the bottom, the flow is aligned with  $f/H$  contours, towards the surface the flow turns according to the horizontal density gradients.

Various studies have investigated the mechanisms that drive the variability of the Nordic Seas' circulation. The exchange between the Atlantic Ocean and the Nordic Seas has received most attention as this forms the direct connection with the AMOC. Whether

wind or buoyancy variations are important depends on the time scale of interest (*Bringedal et al.*, 2018). Wind variations seem to dominate the in- and outflow variability mainly on a seasonal timescale, buoyancy variations dominate on a (multi)decadal timescale.

*Spall* (2011) has shown, using an idealized model framework, that the exchange between the Atlantic Ocean and the Nordic Seas is primarily driven by buoyancy forcing, where a quasi-stationary balance is found on a timescale of  $\sim 30$  years. The convection process in the interior basins of the Nordic Seas creates a pressure gradient at depth that drives the dense water towards the Atlantic (*Hansen and Østerhus*, 2000). The overflows are compensated by the Atlantic Water inflow. 70% of this Atlantic Water is then transformed to overflow, driven by thermohaline processes. The other 30% of AW is transformed to a fresher and therefore lighter watermass (*Østerhus et al.*, 2019). So far, this partition of Atlantic Water transformation into dense and light waters has been rather stable, but it might shift with changing environmental conditions.

### 1.3. WATERMASS TRANSFORMATION PROCESSES

The overflows that leave the Nordic Seas across the Greenland-Scotland Ridge form the main connection to the lower limb of the AMOC, and understanding their origin and variability is therefore of global interest. As discussed in the previous section, a large part of the overflow originates from the transformation of Atlantic Water in the Nordic Seas. The watermass transformation of AW depends on many features, like the intensity of atmospheric forcing and mixing processes. To understand how the overflow will respond to changes in climate, it is therefore necessary to know its exact origins and how sensitive the processes that create the overflows are to changes in the environment. The complexity of the Nordic Seas, due to i.e. the large variety in watermasses and dynamics (see section 1.2), has made it difficult to reach a consensus on what process drives the overflow variability and where the overflows are formed. Especially the importance of deep convection, which mainly occurs in the Greenland Basin, with respect to the gradual transformation of AW along its pathways in the eastern basins has been a matter of debate. This section addresses some of the mechanisms involved for AW watermass transformations and how the Nordic Seas are different from other regions where dense water is created that contributes to the lower limb of the AMOC.

#### 1.3.1. DEEP CONVECTION

As mentioned in the introduction of this section, deep convection processes in the Greenland Basin create watermasses with a very high density, which potentially contribute to the overflows. Deep convection typically occurs in regions where the basin is characterized by a weak flow in the interior (*Marshall and Schott*, 1999), like the Labrador Sea, the Irminger Sea and the Greenland Basin. These regions have a cyclonic circulation and therefore they display a doming of isopycnals. This makes them favorable regions for deep convection, as the shape of the isopycnals brings the weakly stratified water closer to the surface. During deep convection the ocean experiences a large loss of buoyancy resulting in a homogeneous dense body of water that can extend to depths of 2000m. The process is often subdivided in three stages; preconditioning during late autumn and early winter, deep convection during the second half of winter and restratification in

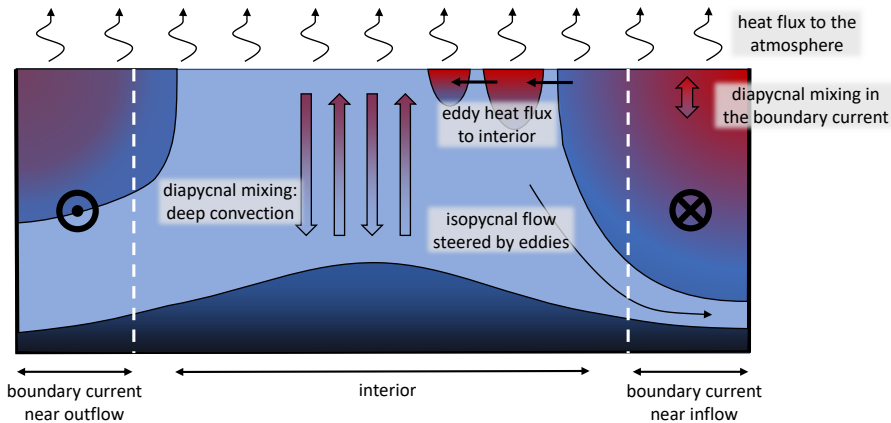


Figure 1.3: Schematic representation of watermass transformation processes in a marginal sea.

early spring (*Marshall and Schott, 1999*). During preconditioning the ocean stratification is weakened. Then, deep convection takes place in localized ‘plumes’ of  $\sim 1$  km width due to large heat loss to the atmosphere. As a result, the heat and salt inside the plume is homogenized and a deep mixed layer is created. Large downward transport takes place within the plumes, which is compensated by upwelling surrounding the plumes (up and down arrows in Figure 1.3). Therefore, no net downward mass transport takes place. Lateral mixing homogenizes the dense area. In the last stage, the area of deep convection is restratified by eddies that exchange the water properties between the convection area and the surroundings.

In the Nordic Seas, wintertime convection in the Greenland Basin can sometimes extend to the bottom (Figure 1.2b), forming the Greenland Sea Deep Water (GSDW, *Helland-Hansen and Nansen, 1909; Carmack and Aagaard, 1973; Malmberg, 1983; Aagaard et al., 1985*). This is one of the densest watermasses found in the Nordic Seas. The intensity of convection events in the Greenland Basin is very sensitive to environmental conditions. Since the late 1970s convection is less deep and the watermass created is lighter. This has been attributed to a decreased wind stress curl, a reduction in sea ice formation (less brine release and therefore increased stratification, *Meincke et al., 1992*) and a reduced atmospheric heat loss (*Moore et al., 2015*). More recently, an increase in mixed layer depth is observed, possibly due to increased salinities (*Brakstad et al., 2019*).

However, where large variations are observed for the formation and properties of dense water in the Greenland Basin, the strength of the overflows leaving the Nordic Seas has been relatively constant (*Eldevik et al., 2009*). As pathways of dense water from the Greenland Basin to the overflows are not yet fully understood (*Brakstad et al., 2019*), it is not clear to what extent the convection in the Greenland Basin actually contributes to the overflows. Recall that regions where convection takes place are characterized by a weak mean flow. Therefore, a mechanism is needed that connects the interior to the

boundary current, such that the dense watermass can be exported.

### 1.3.2. INTERIOR-BOUNDARY CURRENT EXCHANGES

The connection between the interior where deep convection occurs and the cyclonic boundary current that exports dense waters is facilitated by eddies. These vortices originate from the baroclinically unstable boundary current and transport buoyant water from the boundary to the interior (Figure 1.3). This mechanism has been thoroughly investigated using conceptual models of generic marginal seas subject to buoyancy loss. These show that the properties of the watermasses leaving the marginal sea depend on the balance between the eddy heat flux from the boundary current to the interior and the heat lost to the atmosphere (Spall, 2004; Straneo, 2006a; Spall, 2012). Furthermore, due to the exchange with the interior and direct cooling by the atmosphere, the boundary current itself becomes more dense and more barotropic (Figure 1.3).

The relatively easy concept of a balance between the heat provided by the instability of the boundary current and the heat lost to the atmosphere has a number of implications for how the deep convection process is controlled. For example, a very stable boundary current will result in a dense interior, but less export of dense water since there is less water exchanged by eddies (Spall, 2004). This shows that there is no simple relation between the amount of cooling or the density of the waters formed in the interior and the strength of the AMOC. Instead, the density gradient in the downstream direction of the boundary seems to provide a better estimate for the strength of the large scale AMOC (Spall and Pickart, 2001).

As the instability of the boundary current plays a crucial role for the properties and export of dense waters, many studies addressed the theoretical mechanisms behind this instability. Often the classical Eady theory is referenced that, when assuming quasi-geostrophic flow, provides an estimate for the growth rate and length scale of the instability (Eady, 1949). Blumsack and Gierasch (1972) extended this stability analysis to include the effects of a bottom slope. They show that the growth rate of the boundary current instabilities depends on the ratio of the bottom slope and the slopes of the isopycnals. Steeper isopycnals lead to a more unstable boundary current, whereas a steeper bottom slope leads to a more stable boundary current. Where the first relation is well known, the second relation does not hold in some regions that are characterized by a steep continental slope, like near the west coast of Greenland and near the Lofoten Islands. At these locations, intense eddy shedding is observed leading to the so-called Irminger Rings in the Labrador Sea and the Lofoten Eddies in the Lofoten Basin. Isachsen (2015) showed that the Eady theory is not sufficient to explain the increased instability in these regions with steep topography, and that interior potential vorticity gradients need to be considered and nonlinear effects become important.

The Irminger Rings in the Labrador Sea form the main buoyancy supply for restratification of the convective area (Katsman *et al.*, 2004; Gelderloos *et al.*, 2011) and play a key role for the sinking of dense watermasses. As during deep convection no net downward transport takes place (Send and Marshall, 1995), net sinking can only occur near boundaries. The sinking itself is observed, both in the ocean (Spall and Pickart, 2001) and in laboratory experiments (Cenedese, 2012). Also in global-scale numerical ocean simulations with sufficient horizontal resolution, sinking occurs in a narrow region near

the continental boundaries and the amount of downwelling varies regionally (*Katsman et al.*, 2018; *Sayol et al.*, 2019). Especially where the Irminger Rings are shed, large downward motion is seen (*Georgiou et al.*, 2019). Using an idealized numerical simulation, *Brüggemann and Katsman* (2019) showed that the eddies stir dense watermasses that are created in the interior towards the boundary along isopycnals well below the mixed layer (figure 1.3). Furthermore, they concluded that the sinking observed near the boundaries is not a signal of local diapycnal transport. Instead, the net downward movement of isopycnals is due to the eddy shedding.

### 1.3.3. DIFFERENCE BETWEEN THE NORDIC SEAS AND THE LABRADOR SEA

As seen in the previous section, eddies originating from the boundary current balance the heat loss of the interior to the atmosphere and create a pathway for dense interior watermasses to the boundary current. These findings are mainly based on idealized model studies that use the Labrador Sea as a reference and that assume that the main source of the dense outflow is the watermass created by deep convection in the interior.

The Labrador Sea is the classical example of a marginal sea with a single basin, one cyclonic buoyant boundary current and deep convection in the interior. The outflow of dense water from the Labrador Sea can by no means be compared to the overflows from the Nordic Seas, as the Nordic Seas consist of multiple basins, with multiple boundary currents and with very different hydrographic characteristics. One similarity with the Labrador Sea is the amplified eddy activity near the Lofoten Islands. However, the eddies can not reach the region with deep convection in the Greenland Basin as they are blocked by the mid-ocean ridges (section 1.2).

Furthermore, the contribution of the open-ocean convection in the Greenland Basin to the overflow is unclear. Several studies propose that it is more likely that the overflow is connected to the gradual transformation of Atlantic Water as it circulates the Nordic Seas (*Eldevik et al.*, 2009). For example, *Mauritzen* (1996) argues that the Atlantic Water returning through the Fram Strait is already dense enough for the overflow and the importance of the Greenland Sea and Iceland Sea is therefore questionable. The seasonality of the hydrography derived from ARGO floats shows that the main densification of the Atlantic inflow indeed takes place in the Norwegian and Lofoten Basin and that the Greenland Sea only slightly impacts the characteristics of the overflow water through mixing (*Latarius and Quadfasel*, 2016). As the Lofoten Basin is anomalously warm and is continuously replenished by eddies from the boundary current that increase the residence time of AW in this basin, a huge amount of heat can be lost in this area (*Bosse et al.*, 2018).

The discovery of the North Icelandic Jet (NIJ) renewed the interest in convection in the Greenland Basin and near the Icelandic Plateau (*Jonsson and Valdimarsson*, 2004). The NIJ contributes about one third of the densest overflow through Denmark Strait and seems to transport watermasses formed in the interior of these basins (*Våge et al.*, 2011). Furthermore, *Eldevik et al.* (2009) estimate that interior watermasses of the Greenland Basin and Icelandic Plateau form the main contribution to the overflow through the Faroe Bank Channel.

Even when the exact origin of the overflows would be known, multiple modeling studies suggest that the composition may change due to the sensitivity of the circula-

tion to changes in wind forcing (e.g. *Eldevik et al.*, 2005; *Köhl*, 2010). It therefore remains a challenge to correctly predict the response of the overflow characteristics to a changing climate.

## 1.4. INTRODUCTION TO DATA AND METHODS

There are many different ways to study the ocean using observations, models and numerous techniques to analyze and understand the data. In this section a brief introduction is provided to the observational data sets (1.4.1), the type of ocean models (1.4.2) and the Lagrangian approach (1.4.3) that are used for the work presented in this thesis.

### 1.4.1. OBSERVATIONAL RECORDS OF THE NORDIC SEAS

A significant increase in our understanding of the physics of the oceans was initiated by Scandinavian oceanographers at the end of the 19th century. One of the most famous expeditions, the Fram expedition, was led by the Norwegian explorer Fridtjof Nansen. Although Nansen's group was supposed to be focusing on fisheries resources and to develop new fisheries technology, the ocean expeditions that followed firmly established Norway in polar research. Nansen never managed to achieve his goal to reach the North Pole (which they found out was not situated on land), but the expeditions resulted in several groundbreaking findings on ocean dynamics (*Skreslet*, 2007).

Nowadays, ocean observations are still important to increase our understanding of the ocean physics, especially in the deep ocean. Additionally, continuous monitoring of the ocean system is needed to understand how the oceans will respond to changes in climate. Furthermore, as future predictions are based on climate model outcome, the observations can provide a means to validate the ocean models.

Observational data used in this study can be separated in three types; in-situ measurements, satellite observations and combined products. In-situ measurements are taken by measurement devices located in the ocean or at the ocean surface. There are various shipboard transects within the Nordic Seas, where observations are taken at specified stations. Examples of these transects are the Kögur and Látrabjarg section that are both located in vicinity of Denmark Strait. To measure ocean properties continuously in time, fixed moorings are used.

Instead of fixed observations in space, floats can be used that measure ocean properties while following the ocean movement. This way, the spatial coverage of observations is increased. There are different kind of floats. Today (Jan 6, 2020), 1572 surface drifters are floating at the surface of the global ocean<sup>1</sup>. The surface drifter program (SDP) started in 1979 and has greatly improved our knowledge on the ocean surface circulation. Since the early 2000s, the float data set is extended by ARGO floats that typically flow at a depth of 1000 m. Every 10 days, these floats make a vertical profile measuring conductivity, temperature and pressure and their data and position is collected by satellites once they surface. The ARGO float data set (today 4183 active floats) has increased the vertical resolution of observational data sets and gave insight to the circulation at depth (e.g. *Voet et al.*, 2010). An additional set of floats are the RAFOS floats that are neutrally buoyant and use an acoustic method to determine their position as they do not surface. They can

---

<sup>1</sup><https://aoml.noaa.gov/phod/gdp/>

be installed at a level of constant pressure or density and can therefore be useful to trace a specific watermass (e.g. *Rosby et al.*, 2009a).

The in-situ measurements have a very unevenly distributed temporal and spatial resolution especially in the Nordic Seas. Most observations are obtained in summer months and in the eastern basins of the Nordic Seas as a result of harsh winter conditions and sea-ice cover. Attempts are made to improve the coverage in the western basins. *Isachsen et al.* (2014) for example attached small devices to seals to measure salinity and temperature along their swimming path. The data is transmitted to satellites when the seals come to the surface to breathe. Although the seals' pathway is not representative for the circulation in the Nordic Seas, they do improve the data coverage on the Greenland shelf area and in the western basins (*Isachsen et al.*, 2014).

Since 1978, the temporal and spatial resolution of the available data increased as satellites started to monitor ocean properties, like sea surface height, temperature and sea-ice concentration. These measurements provided a global monitoring system, but are unfortunately limited to properties at the sea surface and to sea-ice free regions.

Efforts have been made to interpolate all available observations to obtain a so called climatology of the ocean. An example for the Nordic Seas is the Climatological Atlas of the Nordic Seas, that provides interpolated properties from the unevenly distributed platforms onto a  $0.25^\circ \times 0.25^\circ$  lon x lat grid with 29 vertical levels (*Korablev et al.*, 2014). The atlas covers a large time period from the end of the 19th century to 2012. However, interpolation errors are large due to the strong seasonal and spatial biases.

More useful in this case are ocean reanalyses. The reanalyses are output from a model simulation that is constrained by assimilation of observations: every timestep the modeled fields are corrected based on observations. This way, there are no interpolation errors as for the climatology's and as it is a model, many more diagnostics can be evaluated than originally observed. As many different choices can be made on surface forcing and how to assimilate the observations, there are various reanalyses available<sup>2</sup>. For derivation of Figure 1.2 the GLORYS2V4 is used, which is forced by the ERA-interim (atmospheric) reanalysis and uses all in-situ and satellite measurements available.

### 1.4.2. NUMERICAL OCEAN SIMULATIONS

As discussed in the previous section, observational studies of the Nordic Seas are strongly limited in time and space and are subject to the harsh winter conditions in this area, which makes the study of the processes discussed in section 1.3 difficult. Ocean models can be very useful to improve the physical understanding of specific processes in the Nordic Seas or to predict the sensitivity of the system to changes in environmental parameters. These models can typically be separated in two categories.

The first category consists of models that solve the Navier-Stokes equations (the momentum equations), the continuity equation and other conservation equations numerically, to reach a trustworthy representation of reality. Some of these models are global and coupled to an atmospheric model and an ice model; the general circulation models (GCMs). GCMs are huge and demand a network of high-capacity computers to perform the calculations needed to provide predictions for the future climate on Earth. To keep the simulations manageable, the spatial and temporal resolution of the model is lim-

<sup>2</sup><https://reanalyses.org/ocean/overview-current-reanalyses>

ited. Therefore, many physical processes are not explicitly resolved and represented by parameterizations. To resolve eddies for example, the horizontal resolution needs to be smaller than the first baroclinic Rossby radius of deformation. This length scale depends on latitude, stratification and ocean depth (Hallberg, 2013) and is 3-7 km in the Nordic Seas (Nurser and Bacon, 2014). Furthermore, artificial diffusion is needed to secure the model stability (e.g. Tréguier *et al.*, 2005; Chassignet and Marshall, 2008). Many of the GCMs have a horizontal ocean resolution of  $\sim 40$  km and as a result, the model performance regarding the Nordic Seas is poor. The GCMs show a warm and saline bias and circulation patterns and convection sites differ in strength and location compared to observations (Yeager and Danabasoglu, 2012; Danabasoglu *et al.*, 2014).

A Nordic Seas simulation that compares better to observations requires a higher horizontal and vertical resolution. Choices have to be made for the duration of the simulation, the size of the domain, and the coupling to the atmosphere and sea ice, as the simulations are still limited by the computer power and storage capacities. The resulting high resolution regional ocean models can no longer be used to study long term climate change, but are very useful to study the role of small-scale processes for the dynamics in the system. Specific examples of such models are provided in **chapter 3**. Although resolving many more processes, even in these models parameterizations are necessary and i.e. lateral boundary conditions need to be applied. A way to improve both the GCMs and these high resolution simulations is to develop better parameterizations. This brings us to the second category of ocean models.

The second category of models are process oriented and often based on simplified geometry. They are designed to study basic physical mechanisms. Some of these models are 3D, still solving the full set of equations, but very idealized in their geometry. These idealized models can perform multiple sensitivity studies at a high resolution to resolve eddies, but without a high computational cost. An idealized approach allows for an increase in the complexity of the model step by step, which elucidates the connection and the physics behind many different processes. Another example of process-oriented models are models that reduce the complexity of the system to a core set of algebraic equations, like the famous box model of Stommel based on conservation equations indicating the bistability of the AMOC (Stommel, 1961). Also the conceptual frameworks developed by e.g. Spall (2004) discussed in section 1.3.2 are an example of such models. All these theoretical models have contributed to the general understanding of the AMOC. They provide a means to interpret observations and the complexity described by models from GCMs (Johnson *et al.*, 2019). The study performed in **chapter 2** is based on both a conceptual model and an idealized model simulation (see also section 1.5).

### 1.4.3. LAGRANGIAN METHODS

In moving fluids, like the ocean, the system can be described in a reference frame that is fixed in space, the Eulerian approach, or in a reference frame that is moving with the flow, the Lagrangian approach. Most ocean model data and observational data sets are Eulerian as they provide ocean properties at fixed locations that don't change in time. The surface drifters, ARGO and RAFOS floats described in section 1.4.1 are Lagrangian in nature, as they drift with the flow. Analyses of drifter pathways have often led to improved understanding of the ocean circulation. In addition, the data along the float trajectory

can be used to determine Eulerian properties of the velocity field (e.g. *Voet et al.*, 2010) and hydrography (e.g. *Latarius and Quadfasel*, 2016) when a sufficient number of floats is present in a specific region.

However, the number of ARGO and RAFOS floats in the Nordic Seas is limited (*Rosby et al.*, 2009b; *Latarius and Quadfasel*, 2016), and the surface drifters mainly occupy the eastern basins. An alternative option is to trace numerical particles using the velocity output from model simulations. There are multiple benefits in analyzing numerical particles instead of float trajectories. The number of floats that have been flowing through the Nordic Seas so far is limited to a few hundred and the length of their pathway depends on the lifetime of the float itself (see **chapter 3**). In contrast, numerical particles can often be released in subsets of tens of thousands of particles without too high computational cost for as many years as needed. Furthermore, not only velocity can be tracked; any diagnostic the model calculates (such as temperature or salinity) can be interpolated onto the particle pathway. Even special behavior can be added to the advection procedure of particles in order to simulate the flow of plastic or biological matter (e.g. *Van Sebille et al.*, 2018).

In case of the AMOC, many studies have used a Lagrangian approach to study the different branches of this circulation (e.g. *Rühs et al.*, 2013; *Lozier et al.*, 2013; *Bower et al.*, 2019). The strength of the AMOC is often characterized by a meridional stream function (zonally integrated transport as a function of latitude and depth, for example Figure 2b in *Rahmstorf et al.*, 2015). A downside of this characterization is that is seems like variations in the zonal direction are of lesser importance. Many idealized schematics of this ‘global conveyer belt’ can be found which all suggest that indeed, the circulation is mainly meridional, but also that the AMOC is a tightly connected system (*Bower et al.*, 2019). Lagrangian studies have helped to change this 2D view to a 3D understanding of the AMOC. These elucidated that the AMOC consists of multiple circulation cells and that a significant fraction of its transport is not carried by the mean flow, but by eddies instead (e.g. *Dengler et al.*, 2004; *Bower et al.*, 2009; *Gary et al.*, 2012; *Rühs et al.*, 2013). Therefore, barely any numerical particles or observational floats follow the pathways as originally schematized.

Technically, numerical particles are advected in the 3D velocity field output of an ocean model. There are several offline Lagrangian codes available that perform these calculations. Which code to use depends on the model configuration the code will be applied to, as many ocean models differ regarding their ocean grid. In this thesis, the Connectivity Modeling System (*Paris et al.*, 2013) and OpenDrift (*Dagestad et al.*, 2018) are used to track numerical particles. These codes use very similar schemes to integrate and interpolate the particle trajectories.

In theory, the next position of a particle is determined by a simple temporal integration:

$$\bar{X}(t + \Delta t) = \bar{X}(t) + \int_t^{t+\Delta t} \bar{v}(\bar{X}(\tau), \tau) \Delta \tau, \quad (1.1)$$

where  $\bar{X}$  and  $\bar{v}$  are vectors indicating the particle position and the velocity at that location, and  $t$  is time. As the model output is discrete, both in time and space, equation 1.1 cannot be solved analytically. Many Lagrangian codes apply a 4th order Runge Kutta (RK4) time-stepping scheme to advect particles in the 3D velocity fields using a discrete

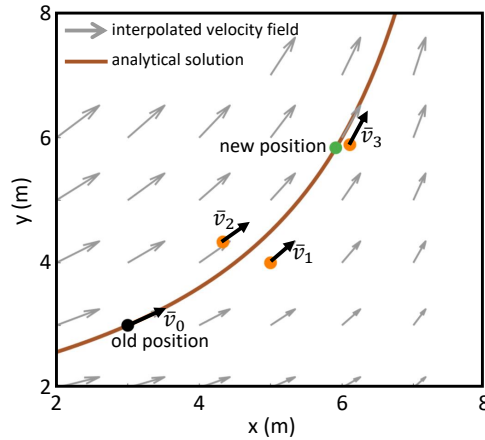


Figure 1.4: Example of the Runge Kutta time stepping solution. An example velocity field is used (gray arrows), given by:  $v_x = -x/3 + 3$  and  $v_y = y/3$  and for calculations  $\Delta t = 2$  s is chosen. The starting position and the final position estimated by the time stepping scheme are indicated by the black and green dot respectively. The orange dots show the intermediate positions used for the Runge Kutta scheme. The Runge Kutta time stepping scheme determines the next position of a particle by combining the velocity at the starting position ( $\vec{v}_0$ ) with the velocities at intermediate positions ( $\vec{v}_{1-3}$ ). The solid line represents the analytical solution of the velocity streamfunction at  $x = y = 3$  m.

timestep  $\Delta t$ . To calculate the next position of a particle, several steps are taken<sup>3</sup>, which are visualized in Figure 1.4.

The velocity output of the model simulation is often stored at relatively low frequency to keep storage costs manageable. The time step used for the RK4 scheme is generally smaller than the frequency at which these velocity fields are saved. Furthermore, the particle location is not restricted to the resolution of the model grid. Therefore, in addition to the temporal integration, the Lagrangian codes need to interpolate the velocity fields in time and space as well. Especially the temporal interpolation can give rise to errors when the velocity output frequency is lower than time scale of the processes of interest (*Da Costa and Blanke, 2004; Qin et al., 2014*).

Also, depending on the model configuration, horizontal and vertical diffusion are often parameterized to account for unresolved processes (e.g. *Large et al., 1994*). Using only the 3D velocity fields for the Lagrangian calculation, the particle pathway is purely advective and therefore might misrepresent the spread of a specific tracer. It is possible to add additional diffusion to the particle pathway both in the horizontal and in the vertical, but it is unclear how well this would represent the parameterized diffusion of the model (*Dugstad et al., 2019a*). If the horizontal resolution of the model is low, it might be better to instead use a tracer that is advected online during the model simulation by the (partly parameterized) advective and diffusive processes represented by the model

<sup>3</sup>User's Guide Connectivity Modeling System v 2.0 at <https://github.com/beatrixparis/connectivity-modeling-system/blob/master/User-Guide-v2.pdf>

itself, instead of adding an artificial diffusion later on (Bower *et al.*, 2019). However, such a tracer calculation would require a much longer integration than needed for the offline particle advection. Also regarding the experimental design, particle analysis can offer more than tracers (Van Sebille *et al.*, 2018). Multiple studies have shown that pathways derived from floats and tracers are almost identical when the model is (partly) eddy-resolving, the temporal resolution of the output is sufficient to capture the variability of interest and sufficient particles are used (Gary *et al.*, 2012; Wagner *et al.*, 2019). The latter is true when similar results are obtained with only half the number of particles (Van Sebille *et al.*, 2018).

There are some major advantages of using particle trajectories over tracer calculations. The calculation of particles trajectories is done offline using the velocity field output, so particles can be traced both forward and backward in time. As such, it is for example possible to investigate the origin of a watermass, which can not be done using tracers (Van Sebille *et al.*, 2018). Furthermore, one can quantify the flow connectivity between different regions. For example, Rühls *et al.* (2013) investigated the connection between the Agulhas Leakage and the subtropical North Atlantic using Lagrangian particles, which led to improved understanding of the contribution of the Agulhas Leakage to the upper limb of the AMOC. When the velocity field used is nondivergent, a volume transport can be assigned to each particle which is conserved along the particle pathway (e.g. Döös, 1995). This way one can investigate how certain flow branches separate (Ypma *et al.*, 2016) or connect to other regions. This method cannot be used in velocity fields that are divergent, for example when only using the 2D flow output (Van Sebille *et al.*, 2018). That is also the reason why observational floats, that by default float at a constant depth, cannot be used to quantify connectivity.

As mentioned before, not only the volume transport can be tracked, but also particle constituents can be traced like temperature and salinity. These are however not conserved along the path, as they can be exchanged with adjacent particles through mixing (Van Sebille *et al.*, 2018). Especially when the local mixed layer depth is deeper than the particle's depth at a certain location, changes in density of the watermass that the particle represents can occur. Tracing temperature and salinity along a particle pathway can therefore be a useful tool to investigate watermass transformation processes (Bower *et al.*, 2019).

It is also possible to perform conditional statistics, which again, is not possible using tracers. Doing so, one assigns specific requirements the particles need to fulfill. Koszalka *et al.* (2013b) and Behrens *et al.* (2017) used this method to for example trace the Denmark Strait Overflow Water forwards and backwards in time (respectively) using a density threshold. Additionally, the resulting particle trajectories can be separated based on a specific property, for example pathway, to investigate the differences and similarities in their respective dynamics.

Regardless of the research interest, a statistical analysis is required as the strength of the Lagrangian approach lies in the number of particles used. Therefore, results are often visualized by probability distributions. One can for example use a binning method to quantify the number of particles per bin specified. The bins could represent longitude and latitude to visualize the pathways of the particles, but any property that is traced by

the particle can be used. Therefore, it is possible to determine the age of a watermass, the transit time through a basin, the temperature change along a pathway and so on. The possibilities are endless and depend entirely on the research questions asked.

## 1.5. OBJECTIVES AND OUTLINE OF THIS THESIS

Many studies in the past few decades addressed the Nordic Seas and its connection to the global climate system. Unfortunately, the spatial and temporal resolution of the observational data set is still limited (section 1.4.1), and there are still many questions to be answered. Furthermore, depending on the research methods used, hypotheses are provided and assumptions are used that have not yet been proven. In this thesis, an attempt has been made to fill some of these gaps by using various modeling strategies and observational data sets. The overarching goal is to improve the current understanding of the dynamics in the Nordic Seas, with a special focus on the transformation of Atlantic Water to dense water.

Theoretical frameworks are often used to investigate what controls the properties of watermass transformation and thermohaline circulation in marginal seas subject to buoyancy loss (see section 1.3). Unlike observational data sets and ocean simulations, the theoretical approach allows the investigation of properties for a wide range of parameters, as the Coriolis parameter, the strength of the forcing and basin geometries. This way, one can gain insight in the physical relations between different properties. Idealized model simulations corroborate many of the conclusions drawn from these conceptual models. One of the more recent results was the key role that eddies play for deep convection processes and for interior-boundary current exchanges (section 1.3.2). The conceptual models highlighted the non-local effect of eddy fluxes on the basin dynamics and it is therefore difficult to represent these eddy fluxes correctly in eddy-parameterizing numerical configurations (such as most ocean models used for climate simulations).

These conceptual models and idealized model simulations are designed to represent generic marginal seas subject to buoyancy loss. Often examples are provided, such as the Labrador Sea, where the results of the study apply to. However, it is unlikely that the results of a conceptual model representing a single basin, one homogeneous interior watermass and a single boundary current are valid for the Nordic Seas, regarding its complex bathymetry, circulation and large variations in watermass properties (see discussion in section 1.3.3). Although there are many characteristics of the Nordic Seas that set this region apart from other marginal seas, like the presence of sea ice and double diffusion processes, the focus in this thesis is on two main aspects that play an important role for watermass transformation processes; the hydrographic asymmetry between east and west and the multiple pathways of Atlantic Water into the Nordic Seas.

This thesis will start with a theoretical basin-wide approach in **chapter 2**. As a first step, the existing theoretical framework from *Spall* (2004, 2011) is extended to incorporate the two-basin character of the Nordic Seas. Doing so, the two-basin conceptual model, in contrast to the one-basin version, can account for the hydrographic asymmetry and the two-branch structure of the Norwegian Atlantic Current in the Nordic Seas. The main research question of this chapter is as follows:

1. *How are the dynamics, circulation and mean hydrography controlled in a two-basin*

*marginal sea subject to buoyancy loss such as the Nordic Seas?*

The results from the conceptual model are then compared to idealized numerical simulations that model a simplified basin geometry of the Nordic Seas. Using the newly developed theoretical framework, it is estimated how a two-basin system like the Nordic Seas would respond to changes in atmospheric forcing.

This chapter is followed by two case studies that investigate specific pathways of Atlantic Water through the Nordic Seas using observations, realistic numerical simulations and idealized numerical simulations. Results from **chapter 2** indicate that the dynamics in the Lofoten Basin and the Greenland Basin are interdependent due to their connection via the front current and the slope current (Figure 1.1). In **chapter 3** this is further investigated with a focus on the role of the Arctic Front for Atlantic Water pathways and transformation. In schematics of the Nordic Seas' circulation, the two-branch structure of the Atlantic Norwegian Current is often schematized as two independent branches that are maintained throughout the Nordic Seas (see Figure 1.1). **Chapter 3** examines this suggested separation of the front current and the slope current by exploring the connectivity between the frontal pathway along the Mohn Ridge and the frontal pathway along the Knipovich Ridge. As addressed in sections 1.1 and 1.3, understanding of pathways of Atlantic Water through the Nordic Seas is essential to comprehend the variability and composition of the overflows. The long residence time of Atlantic Water in the Lofoten Basin is one of the key components of AW transformation (e.g. *Bosse et al.*, 2018). *Dugstad et al.* (2019b) showed that pathways leading towards this region come from south of the Lofoten Basin and from the east where the slope current is most unstable. However, the front current is known to be unstable as well (*Koszalka et al.*, 2011; *Trodahl and Isachsen*, 2018). It is unclear whether the AW that follows this path experiences a different transformation than the AW that resides within the Lofoten Basin.

Therefore, the main research question that is addressed in **chapter 3** is as follows:

*2. How does the front current along the Mohn- and Knipovich Ridges affect the pathways and watermass transformation of Atlantic Water in the Nordic Seas?*

To answer this question, three different Lagrangian data sets are used; trajectories from surface drifters and ARGO floats, trajectories in a high resolution regional model simulation and trajectories in an idealized numerical simulation.

In **chapter 4** the focus shifts from the Atlantic Water that flows into the Nordic Seas east of Iceland to the branch of AW that enters via the North Icelandic Irminger Current west of Iceland. Although the transport along this branch is small in comparison to the NwAC, transformation of the NIIC is thought to form the main contribution to the North Icelandic Jet, the densest part of the Denmark Strait Overflow Water (see section 1.2.2). The formation and dynamics of the NIJ are still a matter of debate; the branch can be traced to its upstream location northeast of Iceland, but there, the signal is lost (e.g. *Våge et al.*, 2011). In its downstream direction, the NIJ volume transport increases, but it is unclear where the additional volume comes from (*Semper et al.*, 2019). *Pickart et al.* (2017) suggested a one-to-one connection between the NIIC and the NIJ via a local overturning loop. To test this hypothesis, two general circulation models are used in **chapter 4**

to investigate the connection between the NIIC and the overflows. The main research question addressed is as follows:

*3. Which pathways does the Atlantic Water that enters the Nordic Seas west of Iceland take and where is this watermass transformed?*

Again, this research question is answered using a Lagrangian approach. Numerical particles are seeded in the NIIC and their pathways are traced in high resolution realistic numerical simulations. As section 1.4.2 already mentioned, global ocean models have difficulties correctly simulating deep convection processes and often display a warm and saline bias. For this reason, the NIIC watermass is traced in not only one, but two ocean simulations. The simulated circulation and hydrographic fields are different for each simulation. Therefore, it is possible to investigate how the different representation of the Nordic Seas' characteristics could lead to different pathways and transformation of the Atlantic Water.

Finally, in **chapter 5** the results obtained in chapters 2-4 are summarized and answers to the research questions proposed in this section are provided. Furthermore, the implication of the results presented in this thesis for understanding of the dynamics of the Nordic Seas are discussed. Research often leads to more questions and therefore recommendations for further research are provided as well.

# 2

## THE CONTRASTING DYNAMICS OF THE BUOYANCY-FORCED LOFOTEN AND GREENLAND BASINS

*When using a theoretical framework, the Nordic Seas are commonly described as a single basin to investigate their dynamics and sensitivity to environmental changes. Here, we introduce a conceptual model for a two-basin marginal sea that better represents the Nordic Seas geometry. In our conceptual model, the marginal sea is characterized by both a cyclonic boundary current and a front current as a result of different hydrographic properties east and west of the mid-ocean ridge. The theory is compared to idealized model simulations and shows good agreement over a wide range of parameter settings, indicating that the physics in the two-basin marginal sea is well captured by the conceptual model. The balances between the atmospheric buoyancy forcing and the lateral eddy heat fluxes from the boundary current and the front current differ between the Lofoten and the Greenland Basins, since the Lofoten Basin is more strongly eddy-dominated. Results show that this asymmetric sensitivity leads to opposing responses to variations in the strength of the atmospheric buoyancy forcing. Additionally, the front current plays an essential role for the heat and volume budget of the two basins, by providing an additional pathway for heat towards the interior of both basins via lateral eddy heat fluxes. The variability of the temperature difference between east and west influences the strength of the different flow branches through the marginal sea and provides a dynamical explanation for the observed correlation between the front current and the slope current of the Norwegian Atlantic Current in the Nordic Seas.*

---

Results presented in this chapter have been published as: S.L. Ypma, Spall, M.A., Lambert, E., Georgiou, S., Pietrzak, J.D., and Katsman, C.A., 2020, The contrasting dynamics of the buoyancy-forced Lofoten and Greenland Basins, *Journal of Physical Oceanography*, 50(5), 1227–1244

## 2.1. INTRODUCTION

The Nordic Seas form an important gateway between the Atlantic Ocean and the Arctic Ocean. Warm and saline waters enter the Nordic Seas from the south and facilitate a rich ecosystem and a mild climate in Norway (e.g. *Rhines et al.*, 2008; *Mork and Skagseth*, 2010). The western side of the Nordic Seas is filled with fresh and cold waters originating from the Arctic. Mixing of watermasses from these different sources in addition to severe winter conditions make the Nordic Seas a crucial region for dense watermass formation (e.g. *Eldevik et al.*, 2005; *Messias et al.*, 2008; *Våge et al.*, 2015). The dense waters flow across the Greenland-Scotland Ridge into the Atlantic via the overflows and contribute to the lower limb of the Atlantic Meridional Overturning Circulation (AMOC, *Dickson and Brown*, 1994; *Hansen and Østerhus*, 2000). Therefore, changes in the properties and dynamics of the Nordic Seas impact not only the local climate and ecosystem, but also the global climate through changes in the ocean circulation.

Global mean atmospheric temperatures are expected to increase by 3.7°C under the RCP8.5 ('high emission') scenario by the end of the century (*IPCC*, 2013). Due to the Arctic Amplification, the expected warming above the Nordic Seas will exceed that of the midlatitudes by at least a factor two (e.g. *Screen and Simmonds*, 2010). The warming is expected to enhance the positive trend of the North Atlantic Oscillation (NAO) observed since the 1960s (e.g. *Hurrell et al.*, 2001). A positive NAO phase often coincides with reduced heat loss from the Nordic Seas to the atmosphere and increased precipitation and river runoff (*Furevik et al.*, 2005). Both mechanisms tend to reduce convection events by stabilizing the water column. However, in recent years, mixed layer depths in the Greenland Basin have deepened, possibly associated with increased near-surface salinities (*Brakstad et al.*, 2019). Due to the rather complex nature of the Nordic Seas it is therefore difficult to predict how it will respond to climate change and which physical mechanisms drive its response.

Paleo records show that the Nordic Seas have undergone large changes in both hydrography and dynamics in the past (e.g. *Fronval and Jansen*, 1996; *Andersen et al.*, 2004). However, the spatial and temporal resolutions of these records are low and the underlying mechanisms of the observed changes are not clear. Unfortunately, fully coupled climate models lack the resolution to properly resolve the dynamical processes that play a role in the Nordic Seas (e.g. *Tréguier et al.*, 2005; *Danabasoglu et al.*, 2014; *Langehaug et al.*, 2017). An alternative way to shed light on what actually controls dynamical changes in marginal seas like the Nordic Seas is to use an idealized approach.

Conceptual models described by e.g. *Spall* (2004), *Walín et al.* (2004), *Straneo* (2006a) and *Iovino et al.* (2008) have been applied to generic marginal seas subject to buoyancy loss. These studies characterize the marginal sea by a motionless interior and a single buoyant boundary current. They have proven to give reasonable predictions for watermass properties in marginal seas like the Labrador Sea. Furthermore, the analytical frameworks developed in these studies have increased the understanding of the role of eddies and topography on the dynamics in these regions and they provide means to interpret projections from climate models and observed changes in the past. The comparison between results from the conceptual models with high resolution (idealized) model simulations is surprisingly good, considering the number of simplifications made to enable analytical solutions.

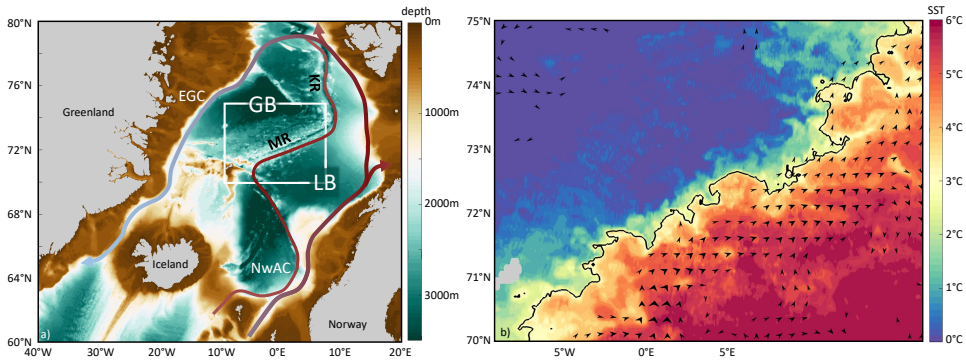


Figure 2.1: a) Schematic of the circulation in the Nordic Seas and bathymetry. b) Sea surface temperature (SST) from AVHRR sensor; image of April 29, 2017, showing the temperature of the Lofoten Basin and the Greenland Sea at the location of the white box indicated in the left panel (black line is the 3°C contour). The black arrowheads show the 2017 mean geostrophic velocity from AVISO satellite altimetry for velocities stronger than 0.04 m/s. NwAC: Norwegian Atlantic Current, EGC: East Greenland Current, LB: Lofoten Basin, GB: Greenland Basin, MR: Mohn Ridge, KR: Knipovich Ridge.

The theories developed in *Straneo* (2006a) and *Spall* (2004) were motivated by the properties of convection in the Labrador Sea, whereas the studies by *Iovino et al.* (2008) and *Spall* (2011) focused on the Nordic Seas by adding the dynamical role of the Greenland-Scotland Ridge. The latter studies still describe the Nordic Seas by one interior basin and a single boundary current. However, observations show that the eastern side of the Nordic Seas (the Lofoten Basin) differs from the western side (the Greenland Basin) regarding hydrography and dynamics (see Figure 2.1).

A warm and saline watermass fills the upper 500 m of the Lofoten Basin, whereas the Greenland Basin is filled with fresh and cold waters (Figure 2.1b, e.g. *Blindheim and Østerhus*, 2005; *Nilsen and Falck*, 2006; *Latarius and Quadfasel*, 2016). A conceptual model using a single interior basin is not able to capture this large difference in hydrography, making a two-basin approach more suitable. The difference in watermasses between east and west creates a strong front aligned with the Mohn-Knipovich Ridge (*Bosse and Fer* (2019), see satellite image in Figure 2.1b). As a consequence, the Atlantic Water that flows through the Nordic Seas takes different paths; one along the slope of the Norwegian continental margin (the inner branch of the Norwegian Atlantic Current, NwAC) and one along the front (the outer branch of the NwAC, Figure 2.1a, e.g. *Voet et al.*, 2010). Observations indicate an anticorrelation between the strength of the front current and the slope current on seasonal and decadal timescales (*Mork and Blindheim*, 2000; *Bosse and Fer*, 2019; *Broomé et al.*, 2019; *Raj et al.*, 2019), implying that these currents are dynamically connected. For the description of a marginal sea such as the Nordic Seas, one therefore needs to consider not only a boundary current, but also a front current.

Previous studies have shown that the mid-ocean ridge is essential in separating the east from the west (e.g. *Rosby et al.*, 2009b; *Spall*, 2010). Another important topographic feature in the Nordic Seas is the steepening of the coastal slope near the Lofoten Islands. Due to the increased instability of the inner branch of the NwAC near this topographic

steepening, anticyclonic eddies continuously replenish the interior of the Lofoten Basin with warm and saline waters from the boundary current (e.g. *Volkov et al.*, 2013; *Isachsen*, 2015; *Richards and Straneo*, 2015). Due to the wide horizontal extent of this warm water mass, the buoyancy loss over the Lofoten Basin is much larger than over the Greenland Basin (*Segtman et al.*, 2011). So, the Lofoten Basin differs from the Greenland Basin also from a dynamical point of view. Observations corroborate the view that the eastern and western basin are dynamically different as the basins do not change their properties uniformly over time (e.g. *Fronval and Jansen*, 1996; *Andersen et al.*, 2004; *Furevik et al.*, 2005).

The main aim of our study is to investigate the response of the Nordic Seas to a changing atmospheric temperature and to provide a physical understanding of the mechanisms involved. A conceptual model is proposed by extending the theoretical framework described in *Spall* (2011) to a two-basin marginal sea with both a slope current and a front current. The model is tested against numerical simulations for a wide range of parameters. We address the following questions:

1. How can the dynamics of a two-basin marginal sea be described by a conceptual model?
2. What controls the mean hydrography and volume transport in a two-basin marginal sea?
3. How does the addition of a ridge change the marginal sea response to changes in atmospheric buoyancy forcing?

Section 2.2 describes the numerical simulation and summarizes the conceptual model from *Spall* (2011) that is used as a base for our study. Section 2.3 provides the extended analytical framework describing a two-basin marginal sea and discusses the implications of this extension. In section 2.4, the sensitivity of the marginal sea to changes in atmospheric buoyancy forcing is investigated using both the conceptual model and the numerical simulations and a discussion on the results and conclusions are provided in section 2.5.

## 2.2. METHODS

To test the validity of the conceptual model described in section 2.3, estimates from the analytical framework are compared to diagnostics from an eddy-resolving regional ocean circulation model. A short description of the numerical simulations is given in section 2.2.1, including details on the model configuration (part 1) and a description of the reference simulation (part 2). The idealized approach to the model set-up allows for straightforward comparison between the output and the estimates from the theoretical framework (part 3). For the conceptual model, we build upon the one-basin framework derived by *Spall* (2011) and use a similar approach but applied to a two-basin marginal sea rather than a single basin. For reference, the main derivation and assumptions of *Spall* (2011) are summarized in section 2.2.2.

### 2.2.1. IDEALIZED NUMERICAL MODEL SIMULATION OF THE NORDIC SEAS

An idealized configuration of the Massachusetts Institute of Technology (MIT) general circulation model is used in this study (Marshall *et al.*, 1997). The aim of the simulations is to capture the two-basin character of the Nordic Seas; an eddy-rich and warm basin in the east, a cold basin in the west, a strong front between the eastern and western basin aligned with a mid-ocean ridge, and the branching of the inflow from the south.

#### MODEL CONFIGURATION

The model domain consists of a 1000x1400 km<sup>2</sup> basin (the bathymetry is shown in Figure 2.2a). The horizontal grid spacing is 5 km and the model has 33 levels in the vertical with thickness ranging from 20 m in the upper layers to 200 m near the bottom. At  $y = 500$  km an island is located (representing Iceland), separating the north ('the Nordic Seas') from the south ('the North Atlantic Ocean'). At this latitude the in- and outflow is partly obstructed by a sill of 1000m depth (representing the Greenland-Scotland Ridge). A mid-ocean ridge of 1200m depth (representing the Mohn-Knipovich Ridge) separates the eastern (Lofoten) basin from the western (Greenland) basin. The slopes of the mid-ocean ridge, the island and the perimeter of the basin are linear with a factor of 0.012. In the east, the topographic slope varies from 0.012 to 0.062 to resemble the region of steep topography near the Lofoten Islands (see contours in Figures 2.2a-b).

A buoyant cyclonic boundary current is forced along the perimeter of the model domain by restoring temperature and velocity in a region south of the island (white box in Figure 2.2a). A short restoring time scale of 2 hours is used. In the restoring region, temperature is restored to 10 °C at the surface, and to constant vertical and meridional buoyancy gradients of  $N_0^2 = 4 \times 10^{-6} \text{ s}^{-2}$  and  $M_0^2 = 1.6 \times 10^{-8} \text{ s}^{-2}$  respectively. Using thermal wind balance and assuming zero flow at the bottom, these values result in a restoring target of the zonal velocity of 0.4 m s<sup>-1</sup> at the surface, reducing linearly to the bottom. This yields a first baroclinic deformation radius of ~10 km. The velocity is restored in order to limit the spin-up time of the simulation.

The transport across the sill is variable and depends on the surface forcing applied north of the sill. There, the ocean is cooled by restoring the surface temperature toward a prescribed atmospheric temperature  $T_A$ , where the resulting heat flux over an area  $S$  is given by

$$Q = \int_S (T - T_A) \Gamma dA. \quad (2.1)$$

Here,  $\Gamma$  is the restoring strength in  $\text{W m}^{-2} \text{ K}^{-1}$ . Note that the heat flux  $Q$  is positive when the ocean is losing heat to the atmosphere. The simulations are run for 60 years after which equilibrium is reached. Means over the final 5 years of the simulation are used for the analyses presented in this chapter. Further details on the model configuration can be found in Spall (2011), who uses a similar configuration without the mid-ocean ridge.

#### HYDROGRAPHIC AND DYNAMICAL PROPERTIES OF THE REFERENCE SIMULATION

The parameters for the reference simulation are chosen such to show closest resemblance to reality. To match the observed heat loss over the Lofoten Basin and the Greenland Basin,  $\Gamma = 16 \text{ W m}^{-2} \text{ K}^{-1}$  and  $T_A = 4 \text{ °C}$  are used. These yield a surface heat loss of 46  $\text{W m}^{-2}$  over the western basin and 70  $\text{W m}^{-2}$  over the eastern basin (NCEP-2 estimates

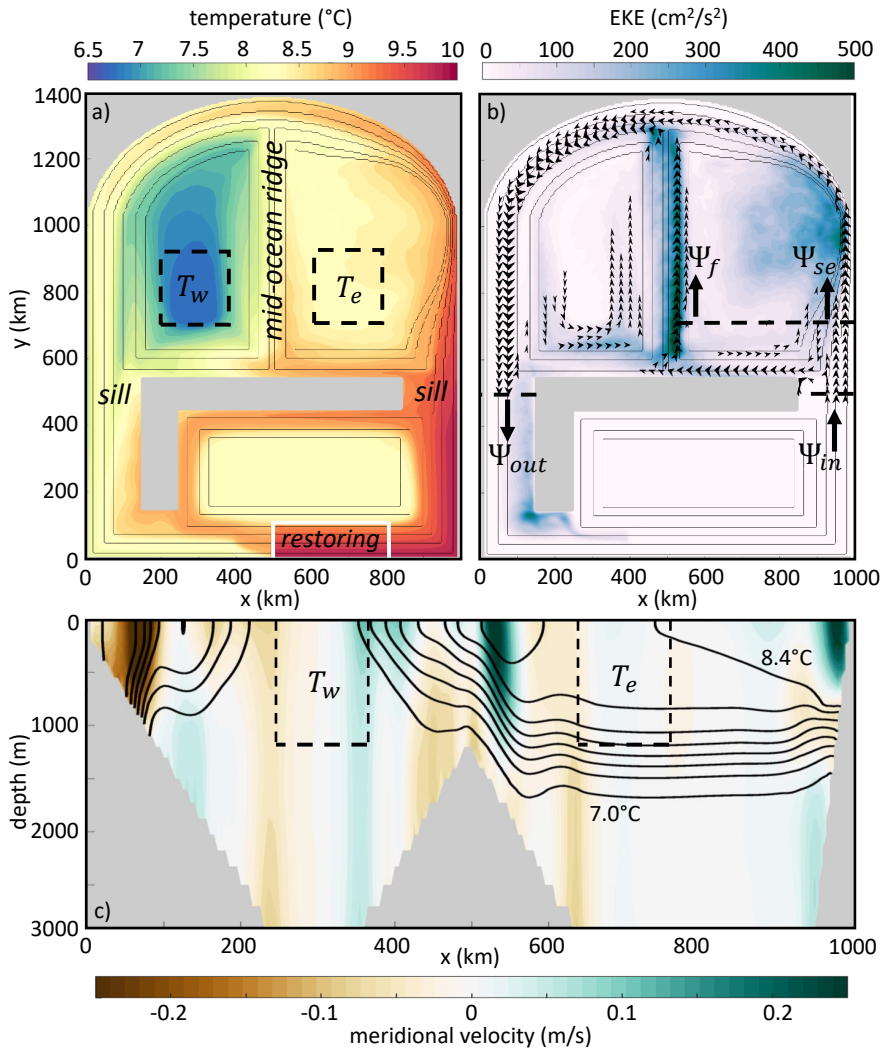


Figure 2.2: a) 5-year mean sea surface temperature (color) and bathymetry (black contours) of the reference simulation. The black boxes indicate regions over which the mean interior eastern basin temperature ( $T_e$ ) and western basin temperature ( $T_w$ ) are calculated. b) 5-year mean surface eddy kinetic energy (shading) and surface velocity  $> 0.05 \text{ m s}^{-1}$  north of the sill (black arrowheads). The horizontal dashed lines indicate where the transport of the inflow ( $\Psi_{in}$ ), the outflow ( $\Psi_{out}$ ), the slope current along the eastern basin ( $\Psi_{se}$ ) and the front current ( $\Psi_f$ ) are evaluated. c) Cross section at  $y = 750 \text{ km}$  of the 5-year mean meridional velocity (shading) and mean temperature (contours, contour interval  $0.2^\circ\text{C}$ ).

give respectively  $43 \text{ W m}^{-2}$  and  $67 \text{ W m}^{-2}$  for the Greenland and the Lofoten Basin, see *Segtnan et al.* (2011)). Note that, just as in observations (*Isachsen et al.*, 2007), the net buoyancy loss to the atmosphere over the Lofoten Basin is much larger than over the Greenland Basin. In the numerical simulations the atmospheric temperature  $T_A$  is uniform. Therefore, the temperature of the eastern and western basin differ due to internal ocean dynamics, not due to a spatial difference in atmospheric buoyancy forcing (in the remainder of the chapter ‘forcing’ always relates to buoyancy forcing). Simulations with a non-uniform atmospheric buoyancy forcing are discussed in appendix 2.A.

In the reference simulation, the surface temperature (SST) of the eastern basin is on average  $1.4^\circ\text{C}$  higher than the western basin (Figure 2.2a and 2.2c). Recall that in the numerical model, density depends on temperature only. In observations, the temperature difference between the Lofoten and the Greenland Basins is much larger ( $\Delta T \sim 6^\circ\text{C}$ , *Bosse and Fer* (2019) and Figure 2.1), but the density difference is for a large part compensated by salinity ( $\Delta\rho \sim 0.30 \text{ kg m}^{-3}$ , *Piechura and Walczowski*, 1995; *Bosse and Fer*, 2019). Therefore, the density difference, which governs the dynamics along the front, in the reference simulation ( $\Delta\rho \sim 0.28 \text{ kg m}^{-3}$ ) is similar to the observations.

The inflow east of the island separates into a current along the eastern boundary (hereinafter the slope current) and a current along the mid-ocean ridge (hereinafter the front current, see arrows in Figure 2.2b). The structure of both branches is clearly visible in the cross-section in Figure 2.2c (green shading at  $x = 550 \text{ km}$  and  $x = 950 \text{ km}$ ). The slope and front current represent the inner and outer branches of the NwAC and display a gradual cooling in the downstream direction (Figure 2.2a). Both currents are unstable; the eddy kinetic energy (EKE) shown in Figure 2.2b reveals enhanced eddy activity along the mid-ocean ridge and near the region where the topography is steep. This region of steep topography leads to increased instability of the boundary current resulting in warm-core eddy shedding as observed near the Lofoten Islands (e.g. *Poulain et al.*, 1996; *Spall*, 2010; *Isachsen et al.*, 2012). It is this enhanced lateral eddy heat flux in the east that leads to a warmer Lofoten Basin than Greenland Basin, and therefore a larger surface heat loss in the east than in the west (see also *Spall* (2010)).

#### DEFINITION OF PARAMETERS USED FOR COMPARISON WITH THE CONCEPTUAL MODEL

The idealized model simulations serve as a tool to test the conceptual model described in section 2.3 for a wide range of parameter settings. To enable comparison between the numerical simulations and the solutions from the conceptual framework, different quantities need to be derived. The conceptual model described in section 2.3 provides estimates for the interior basin temperature in the east ( $T_e$ ) and in the west ( $T_w$ ), for the temperature of the outflowing watermass ( $T_{out}$ ) and for the volume transport of the inflow ( $\Psi_{in}$ ), the slope current ( $\Psi_{se}$ ) and the front current ( $\Psi_f$ ).

The interior basin temperature is calculated by taking the depth average of the regions indicated by the boxes in Figure 2.2a. The temperature of the inflowing and outflowing watermass is determined by taking the transport-weighted mean of the in- and outflow at the sill (horizontal lines in Figure 2.2b at  $y = 500 \text{ km}$ ). The transport of the slope current along the eastern boundary ( $\Psi_{se}$ ) and the front current ( $\Psi_f$ ) are calculated at  $y = 700 \text{ km}$  (horizontal dashed line Figure 2.2b). The transport of the slope current ( $\Psi_{se}$ ) is given by the northward flow east of  $x = 950 \text{ km}$  in the upper 1000 m (see Figure

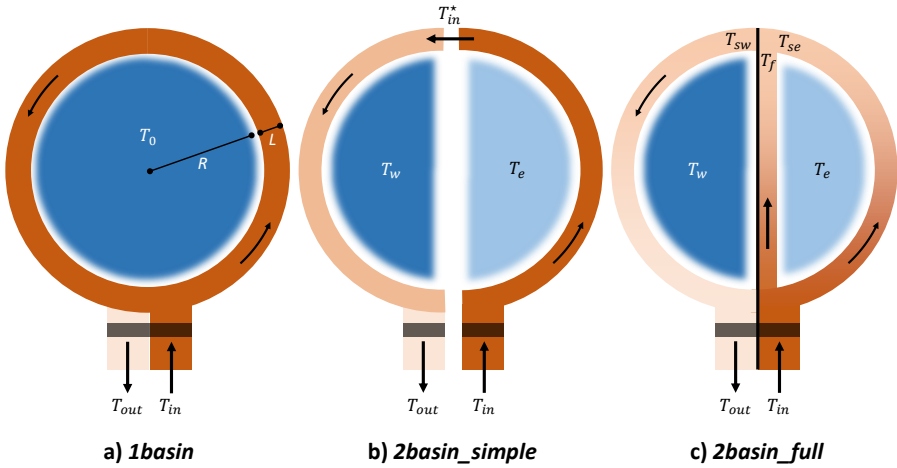


Figure 2.3: Schematic of the conceptual model (a) based on *Spall* (2011) and extended to a two basin system (b) without and (c) with a front current; the black vertical line indicates the location of the mid-ocean ridge, the black horizontal line represents the sill.

2.2c). The front current is meandering and consists of a northward and southward flowing part that is not always clearly distinguishable. Therefore, the transport of the front current ( $\Psi_f$ ) is derived by taking the difference between the total transport across the transect at  $y = 700$  km and the slope current transport.

### 2.2.2. A CONCEPTUAL MODEL WITH ONE BASIN AND A SINGLE BOUNDARY CURRENT

In section 2.3 a conceptual model for a two-basin marginal sea will be derived using a similar approach as the conceptual model described in *Spall* (2011). The domain used by *Spall* (2011) consists of two main regions; the interior and the slope current (hereinafter the *1basin*-framework, schematic Figure 2.3a). Using simple heat balances, solutions can be found for the interior temperature ( $T_0$ ) and the temperature of the outflowing watermass ( $T_{out}$ ). This section summarizes the various assumptions made in *Spall* (2011) and motivates the extension of the initial *1basin*-framework to a two-basin marginal sea.

In the *1basin*-framework, the slope current flows around the interior in a cyclonic direction, while losing heat to the atmosphere via surface fluxes and to the interior via eddy fluxes. The mean flow in the interior, where deep convection takes place, is assumed motionless. There, heat lost to the atmosphere is balanced by the lateral eddy heat gain from the buoyant slope current:

$$\frac{Q_0}{\rho_0 C_p} = 2\pi R H F, \quad (2.2)$$

where  $\rho_0$  is the reference density ( $\text{kg m}^{-3}$ ),  $C_p$  the heat capacity ( $\text{J kg}^{-1} \text{K}^{-1}$ ),  $R$  the radius

Table 2.1: Input parameters for the conceptual model. Values match the numerical reference simulation described in section 2.2.1 (except for the frontal eddy coefficients  $c_{fe}$  and  $c_{fw}$ )

Physical description	Symbol	Reference value	Units
atmospheric temperature	$T_A$	4	°C
inflow temperature	$T_{in}$	9	°C
depth of currents	$H$	650	m
width of currents	$L$	50e3	m
basin radius	$R$	450e3	m
thermal expansion coefficient	$\alpha$	0.2	kg m <sup>-3</sup> K <sup>-1</sup>
gravitational acceleration	$g$	9.81	m s <sup>-2</sup>
reference density	$\rho_0$	1028	kg m <sup>-3</sup>
Coriolis parameter	$f_0$	1.2e-4	s <sup>-1</sup>
eddy coefficient east	$c_e$	0.06	-
eddy coefficient west	$c_w$	0.004	-
eddy coefficient front to the east	$c_{fe}$	0.06	-
eddy coefficient front to the west	$c_{fw}$	0.004	-
restoring strength	$\Gamma$	16	W m <sup>-2</sup> K <sup>-1</sup>
heat capacity	$C_p$	3994	J kg <sup>-1</sup> K <sup>-1</sup>

of the interior basin (m) and,  $H$  the depth of the slope current (m, reference values for all parameters used in this chapter are provided in table 2.1). For simplicity, the domain of the marginal sea is assumed to be circular.

The lateral eddy heat flux,  $F$ , in equation 2.2 is parameterized. It is assumed to depend on the baroclinic velocity of the slope current ( $V_s$ ) and the temperature gradient between the boundary ( $T_s$ ) and the interior ( $T_0$ ), following *Blumsack and Gierasch* (1972) and *Spall* (2004, 2011):

$$F = \overline{u'T'} = c\overline{V_s}(T_s - T_0), \quad (2.3)$$

where  $c$  is the non-dimensional eddy coefficient. The overline refers to the along-flow mean properties of the slope current. The value of the coefficient  $c$  depends on the ratio of the isopycnal slope of the slope current and the topographic slope (*Blumsack and Gierasch*, 1972; *Spall*, 2004). Based on the numerical model topography and the boundary current stratification,  $c = 0.004$  is used for the western basin, where the topographic slope is constant. The choice of  $c$  in the eastern basin is not straightforward, as the lower growth rate predicted by the modified Eady theory cannot explain the observed enhanced eddy activity near the steep topographic slope (see discussion in e.g. *Trodahl and Isachsen*, 2018). Here, we follow the study of *Bracco et al.* (2008) who suggested that a very steep topographic slope can be seen as a vertical wall. Therefore, we assume that the mean flow in the eastern basin feels a flat bottom, which implies an eddy coefficient  $c = 0.06$  (*Spall*, 2004).

Similar to the numerical simulations, the total surface heat loss  $Q_0$  (W) is given by:

$$Q_0 = A_0\Gamma(T_0 - T_A). \quad (2.4)$$

Table 2.2: Non-dimensional parameters

Physical description	Symbol	Equation
atmospheric forcing efficiency	$\mu$	$\frac{\Gamma f_0}{\alpha g C_p (T_{in} - T_A)}$
eddy efficiency	$\epsilon$	$\frac{cR}{L}$
aspect-ratio	$\delta$	$\frac{H^2}{R^2}$

Here,  $A_0$  is the area of the interior exposed to the atmosphere ( $\text{m}^2$ ).

Next, a heat balance for the slope current is defined. It is assumed that the downstream change in heat transport is governed by the surface heat loss to the atmosphere across the slope current ( $Q_s$ ) and the lateral eddy heat flux to the interior:

$$\Psi_s(T_{in} - T_{out}) = \frac{Q_s}{\rho_0 C_p} + 2\pi RHF = \frac{Q_s}{\rho_0 C_p} + \frac{Q_0}{\rho_0 C_p} \quad (2.5)$$

$Q_s$  is defined analogous to equation 2.4, using  $T_s$  and  $A_s = 2\pi RL$ , with  $L$  the width of the slope current (m). The slope current is assumed to be in geostrophic balance, so  $\Psi_s$  ( $\text{m}^3 \text{s}^{-1}$ ) is given by:

$$\Psi_s = \frac{\alpha g H^2}{2\rho_0 f_0} (T_s - T_0) = \overline{V}_s HL. \quad (2.6)$$

Here,  $\alpha$  is the thermal expansion coefficient ( $\text{kg m}^{-3} \text{K}^{-1}$ ),  $f_0$  the Coriolis parameter ( $\text{s}^{-1}$ ) and  $g$  the gravitational acceleration ( $\text{m s}^{-2}$ ). The derivation of the *Ibasin*-framework is based solely on the description of baroclinic currents as we consider wind forcing only implicitly (by homogenizing watermasses and maintaining a level of no motion). The possible impact of the winds on the buoyancy budgets derived in this chapter will be discussed in section 2.5.

To allow the derivation of an analytical solution for both the temperature of the interior and the temperature of the outflowing watermass ( $T_0$  and  $T_{out}$ ), *Spall* (2011) assumes that the temperature of the slope current ( $T_s$ ) is constant and equal to the inflow temperature ( $T_{in}$ ). Solutions for  $T_0$  and  $T_{out}$  can then be found by combining equations 2.2-2.6:

$$T_{in} - T_0 = \frac{\mu}{2\delta\epsilon} \left[ \left(1 + \frac{4\delta\epsilon}{\mu}\right)^{\frac{1}{2}} - 1 \right] (T_{in} - T_A) \quad (2.7a)$$

$$T_{in} - T_{out} = \frac{2\pi\mu}{\delta} \left[ \frac{T_{in} - T_A}{T_{in} - T_0} \left(1 + \frac{2L}{R}\right) - 1 \right] (T_{in} - T_A) \quad (2.7b)$$

Three non-dimensional parameters have been introduced in equation 2.7 (see table 2.2). The parameter  $\mu$  (hereinafter the atmospheric forcing efficiency) and the parameter

$\epsilon$  (hereinafter the eddy efficiency) are both a measure of how effectively heat is extracted from the system, either based on the strength of the air-sea exchange coefficient  $\Gamma$  or on the eddy coefficient  $c$ . Their ratio indicates the dominance of the atmospheric influence relative to the lateral eddy advection on the resulting interior and outflow temperature. These parameters are used to investigate what controls the mean hydrography and volume transport in the marginal sea. In this study, the choice is made to describe the basin geometry solely by the radius  $R$  (instead of by the surface area and perimeter as used in *Spall, 2011*). Therefore, equation 2.7 and the non-dimensional parameters are slightly different. Moreover, an additional 'aspect-ratio' parameter  $\delta$  is introduced.

The solutions provided by equation 2.7 are however identical to those provided by the equations derived in *Spall (2011)* (his equations 8 and 17) and the response of the dynamics of this marginal sea to changes in the atmospheric forcing or eddy fluxes (by changing  $\mu$  or  $\epsilon$ ) are discussed in detail by *Spall (2011)*. One of the key implications of the *1basin*-framework is that the sensitivity of the marginal sea to atmospheric forcing depends on the relative strength of the eddy fluxes compared to the surface fluxes. For example, the Lofoten Basin (hereinafter the eastern basin) is characterized by a large eddy heat flux from the boundary to the interior due to the increased instability of the slope current near the Lofoten Islands. This basin, as discussed by *Spall (2011)*, is typically in an eddy-dominated regime ( $\mu/\epsilon \ll 1$ ), meaning that the basin is characterized by very efficient lateral heat transport to compensate for the surface heat loss. In contrast, in the Greenland Basin (hereinafter the western basin) the lateral heat transport from the boundary to the interior is less strong ( $c$  is small).

As a consequence, the interior basin temperature ( $T_0$ ) is more sensitive to changes in atmospheric forcing in the western basin (blue line in Figure 2.4) than in the eastern basin (red line in Figure 2.4). The following section will extend the *1basin*-framework to a two-basin marginal sea that combines the eddy-dominated eastern basin and the atmosphere-dominated western basin.

## 2.3. CONCEPTUAL MODEL FOR A TWO-BASIN MARGINAL SEA

A stepwise approach is taken to extend the *1basin*-framework (equation 2.7) to a *2basin*-framework. As a first step, the eastern and western basin are treated as two separate basins (schematic Figure 2.3b), where the outflow of the eastern basin is connected to the inflow of the western basin. Results of this approach are discussed in section 2.3.1. Section 2.3.2 further extends the framework by adding a front current and by allowing a gradual cooling of the slope and front current in the downstream direction (schematic Figure 2.3c).

### 2.3.1. A TWO-BASIN APPROACH WITHOUT A FRONTAL CURRENT

As a first step towards a conceptual model for a two-basin marginal sea, the set of solutions given by the *1basin*-framework is applied twice; once for a basin applying a large eddy coefficient (the eastern basin) and once for a basin applying a small eddy coefficient (the western basin). The temperature of the outflow from the eastern basin is then simply used as the inflow temperature for the western basin (representing the recirculating Atlantic Water). This set-up, the *2basin\_simple*-framework, is schematized in Figure

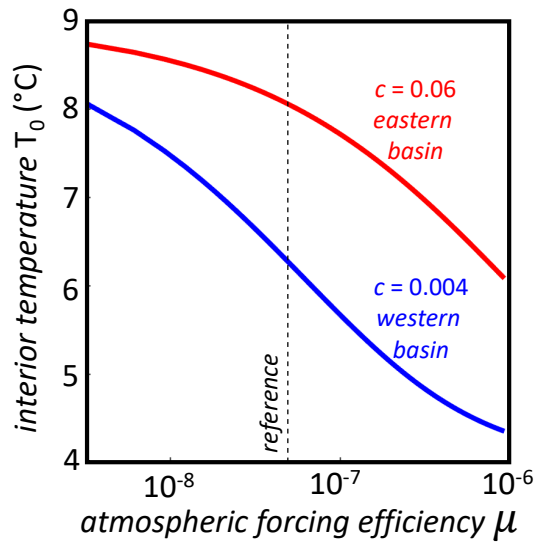


Figure 2.4: The interior basin temperature  $T_0$  as a function of the non-dimensional parameter  $\mu$  for a basin with a large eddy coefficient ( $c = 0.06$ , red line) and for a basin with a small eddy coefficient ( $c = 0.004$ , blue line) using the *1basin*-framework. Input parameters used for the calculation are given in table 2.1. The vertical dashed line indicates the value of the non-dimensional parameter  $\mu$  that corresponds to the reference model simulation. Values of  $c$  used for the eastern basin and for the western basin are estimated based on the steepness of the slope in these basins in the numerical simulations.

2.3b. Following this approach, the solutions for the interior temperature in the east ( $T_e$ ) and west ( $T_w$ ) and for the flow from the east into the west ( $T_{in}^*$ ) and out of the western basin ( $T_{out}$ ) are given by equation 2.8:

For the eastern basin:

$$T_{in} - T_e = \frac{\mu}{2\delta\epsilon_e} \left[ \left( 1 + \frac{4\delta\epsilon_e}{\mu} \right)^{\frac{1}{2}} - 1 \right] (T_{in} - T_A) \quad (2.8a)$$

$$T_{in} - T_{in}^* = \frac{\pi\mu}{\delta} \left[ \frac{T_{in} - T_A}{T_{in} - T_e} \left( 1 + \frac{2L}{R} \right) - 1 \right] (T_{in} - T_A) \quad (2.8b)$$

and for the western basin:

$$T_{in}^* - T_w = \frac{\mu}{2\delta\epsilon_w} \left[ \left( 1 + \frac{T_{in}^* - T_A}{T_{in} - T_A} \frac{4\delta\epsilon_w}{\mu} \right)^{\frac{1}{2}} - 1 \right] (T_{in} - T_A) \quad (2.8c)$$

$$T_{in}^* - T_{out} = \frac{\pi\mu}{\delta} \left[ \frac{T_{in}^* - T_A}{T_{in}^* - T_w} \left( 1 + \frac{2L}{R} \right) - 1 \right] (T_{in} - T_A) \quad (2.8d)$$

Note that  $T_{in}$  is now the temperature of the slope current in the east (equal to  $T_s$ ). Instead of  $T_{out}$  as used in equation 2.7,  $T_{in}^*$  is the temperature of the outflow from the eastern basin (equation 2.8b) and at the same time the temperature of the boundary current in the west (Figure 2.3b). Therefore, in equations 2.8c-d,  $T_{in}$  from equation 2.7 is replaced by  $T_{in}^*$ . As the  $\mu$ -parameter also depends on  $T_{in}$  (table 2.2), an additional term  $(T_{in}^* - T_A)/(T_{in} - T_A)$  appears in equation 2.8c.

The subscript of the  $\epsilon$ -parameter in equation 2.8 indicates whether the eddy coefficient of the eastern or the western basin is used ( $c_e$  or  $c_w$ ). Using the *2basin\_simple*-framework, most combinations of  $c_e$  and  $c_w$  result in an eastern basin that is warmer than the western basin (brown shading in Figure 2.5a). This is because the slope current in the east is always warmer than the slope current in the west ( $T_{in} > T_{in}^*$ ). Therefore, even for equal eddy coefficients (Figure 2.5c), the lateral heat flux from the boundary to the interior is larger in the eastern basin.

Increasing  $c_e$  leads to an increase in the temperature difference between east and west. This is not only because the interior basin temperature in the east,  $T_e$ , increases, but also because the interior basin temperature in the west,  $T_w$ , decreases. The temperature change in the eastern basin is as expected, as the lateral eddy heat flux from the boundary current into the eastern basin increases. Since the eastern slope current has lost more heat to the interior, the slope current of the western basin will be colder and therefore the lateral heat exchange with the western basin interior reduces. So, the eddy efficiency in the eastern basin not only affects the eastern basin interior temperature, but also the interior temperature of the downstream basin. This conclusion does not hold for changes in  $c_w$ , as in the *2basin\_simple*-framework  $c_w$  can only impact the western basin interior and the temperature of the outflow.

The sensitivity of the outflow temperature to the eddy coefficients is as expected; for large  $c$ , the boundary current loses more heat, and the temperature of the outflow reduces (upper right corner Figure 2.5b). The *2basin\_simple*-framework estimates a

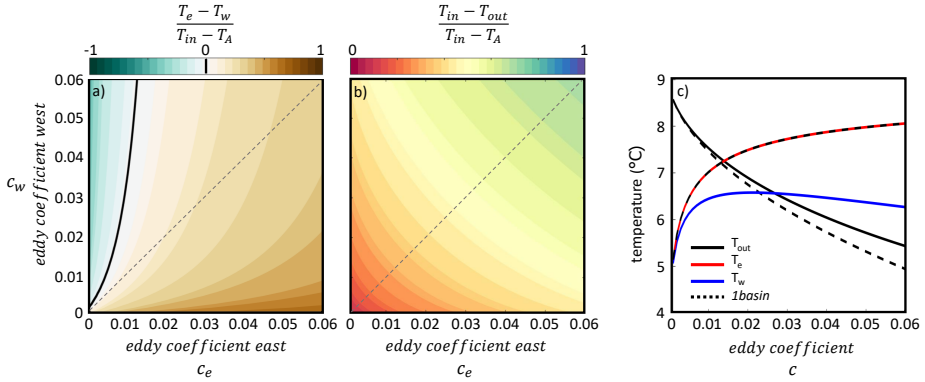


Figure 2.5: Non-dimensional temperature difference between (a) the eastern and western basin and (b) the outflow and inflow as a function of the eddy coefficient in the east ( $c_e$ ) and in the west ( $c_w$ ) for the *2basin\_simple*-framework. In (b) red shading indicates a warm outflow and blue shading indicates a cold outflow. (c) The temperature of the eastern basin interior (red line), the western basin interior (blue line) and the outflow (black line) as a function of the eddy coefficient ( $c = c_w = c_e$ ) for the *2basin\_simple*-framework. The dashed lines show the solutions from the *1basin*-framework.

warmer outflowing watermass than the *1basin*-framework (compare solid and dashed black lines Figure 2.5c). The reason is that due to the lack of a second basin in the *1basin*-framework, the slope current retains a constant temperature everywhere (similar to  $T_{in} = T_{in}^*$ ). Therefore, more heat is lost to the interior in the *1basin*-framework, which results in a colder outflow compared to the *2basin\_simple*-framework.

### 2.3.2. A TWO-BASIN APPROACH WITH A FRONTAL CURRENT

The *2basin\_simple*-framework, using two separate basins representing the Lofoten Basin and the Greenland Basin, already indicates that the dynamics in the upstream basin influence the dynamics in the downstream basin. However, there are two important features that are missing in this simple approach. First, in the Nordic Seas there are two pathways for northward heat transport: the slope current along the continental margin and the front current along the mid-ocean ridge. Therefore, not only the slope current, but also the front current can exchange heat with the interior via lateral eddy heat fluxes. Furthermore, the conceptual models described so far assume that the slope current retains a constant temperature. As seen in Figure 2.2a, this is not an appropriate assumption; much of the heat is already lost before the slope current enters the western side of the basin. This section will implement these components by introducing a front current and a gradual cooling of both the slope current and the front current. This way, the *2basin\_full*-framework is derived that provides valuable insight in the dynamics of a two-basin marginal sea like the Nordic Seas. A schematic of this system is shown in Figure 2.3c.

Using similar heat balances as described in section 2.2.2, a set of 6 equations is derived that can be solved for the interior temperature of the eastern and western basin ( $T_e$  and  $T_w$ ), the temperature of the front current ( $T_f$ ), the temperature of the boundary current in the east ( $T_{se}$ ), the temperature of the boundary current in the west ( $T_{sw}$ ) and

the temperature of the outflowing watermass ( $T_{out}$ , see Figure 2.3c for locations). The set of equations only has solutions for  $T_e > T_w$ , which is the case in the Nordic Seas.

In the interior of the basins, the heat lost to the atmosphere is now balanced by the heat gained by lateral heat fluxes not only from the boundary current, but also from the frontal current (analogous to equation 2.2):

$$\frac{Q_e}{\rho_0 C_p} = \pi RHF_{se} + 2RHF_{fe} \quad (2.9a)$$

$$\frac{Q_w}{\rho_0 C_p} = \pi RHF_{sw} + 2RHF_{fw} \quad (2.9b)$$

The subscripts either refer to the slope current along the eastern boundary ( $se$ ), the slope current along the western boundary ( $sw$ ) or the front current ( $f$ ). Two new free parameters, the frontal eddy coefficients, are introduced as the front current can exchange heat in two directions; to the east (subscript  $fe$ ) and to the west (subscript  $fw$ ). As we are interested in the strength of the heat flux from the front current, rather than in the underlying dynamics of the instability of a front along a mid-ocean ridge, we choose the frontal eddy coefficients ( $c_{fe}$  and  $c_{fw}$ ) such to find closest agreement with the interior basin temperatures given by the numerical simulations (see table 2.1). Sensitivity of the results to changes in the frontal eddy coefficients is discussed at the end of this section.

In addition to equation 2.9 for the interior basin temperatures, three equations for the heat balance are derived for the eastern slope current, the western slope current and the frontal current respectively (analogous to equation 2.5):

$$\Psi_{se}(T_{in} - T_{se}) = \frac{Q_{se}}{\rho C_p} + \pi RHF_{se} \quad (2.10a)$$

$$\Psi_{sw}(T_{sw} - T_{out}) = \frac{Q_{sw}}{\rho C_p} + \pi RHF_{sw} \quad (2.10b)$$

$$\Psi_f(T_{in} - T_f) = \frac{Q_f}{\rho C_p} + 2RHF_{se} + 2RHF_{fw} \quad (2.10c)$$

To close the set of equations, conservation of mass and heat is applied in the northernmost point, where the slope current and frontal current merge:

$$\Psi_{in} = \Psi_{out} = \Psi_{sw} = \Psi_{se} + \Psi_f \quad (2.11a)$$

$$\Psi_{se} T_{se} + \Psi_f T_f = \Psi_{sw} T_{sw} \quad (2.11b)$$

For the *2basin\_full*-framework we assume that the slope current and the front current have equal width  $L$  (see discussion section 2.5) and we again assume that both currents are in thermal wind balance with zero velocity at a given depth  $H$ :

$$\Psi_{se} = \frac{\alpha g H^2}{2\rho_0 f_0} (T_{in} - T_e) \quad (2.12a)$$

$$\Psi_f = \frac{\alpha g H^2}{2\rho_0 f_0} ((\overline{T}_f - T_w) - (\overline{T}_f - T_e)) = \frac{\alpha g H^2}{2\rho_0 f_0} (T_e - T_w) \quad (2.12b)$$

Combining equations 2.9-2.12, substituting equations for the heat flux to the atmosphere, the eddy parameterization (equations 2.4 and 2.3 respectively) and the non-dimensional parameters (table 2.2), six equations are derived for the interior temperature in the eastern and western basin ( $T_e$  and  $T_w$ ), the final temperature of the currents ( $T_{se}$ ,  $T_f$  and  $T_{out}$ ) and the starting temperature of the western boundary current ( $T_{sw}$ ). The resulting set of equations for the *2basin\_full* are given by equation 2.13. In these equations, the overline refers to the along-flow mean temperature of the flow.

equation for  $T_e$ :

$$T_e - T_A = \frac{\epsilon_e \delta}{\mu(T_{in} - T_A)} (T_{in} - T_e)(\overline{T_{se}} - T_e) + \frac{2\epsilon_{fe} \delta}{\pi\mu(T_{in} - T_A)} (\overline{T_f} - T_e)^2 \quad (2.13a)$$

equation for  $T_w$ :

$$T_w - T_A = \frac{\epsilon_w \delta}{\mu(T_{in} - T_A)} (T_{in} - T_w)(\overline{T_{sw}} - T_w) + \frac{2\epsilon_{fw} \delta}{\pi\mu(T_{in} - T_A)} (\overline{T_f} - T_w)^2 \quad (2.13b)$$

equation for  $T_{se}$ :

$$T_{in} - T_{se} = \frac{\pi\mu}{\delta} \frac{(T_{in} - T_A)(\overline{T_{se}} - T_A)}{(T_{in} - T_e)} \frac{2L}{R} + \pi\epsilon_e (\overline{T_{se}} - T_e) \quad (2.13c)$$

equation for  $T_{out}$ :

$$T_{sw} - T_{out} = \frac{\pi\mu}{\delta} \frac{(T_{in} - T_A)(\overline{T_{sw}} - T_A)}{(T_{in} - T_w)} \frac{2L}{R} + \pi\epsilon_w (\overline{T_{sw}} - T_w) \quad (2.13d)$$

equation for  $T_f$ :

$$T_{in} - T_f = \frac{2\mu}{\delta} \frac{(T_{in} - T_A)(\overline{T_f} - T_A)}{(T_e - T_w)} \frac{2L}{R} + 2\epsilon_{fe} \frac{(\overline{T_f} - T_e)^2}{T_e - T_w} + 2\epsilon_{fw} \frac{(\overline{T_f} - T_w)^2}{T_e - T_w} \quad (2.13e)$$

equation for  $T_{sw}$ :

$$(T_{in} - T_e)(T_{se} - T_{sw}) = (T_e - T_w)(T_{sw} - T_f) \quad (2.13f)$$

The first two equations provide estimates for the eastern and western interior basin temperature. Just as for the *1basin-* and *2basin\_simple*-frameworks, the interior basin temperature depends on the ratio  $\mu/\epsilon$ . However, the resulting temperature does not only depend on the relative importance of the atmosphere and the lateral eddy heat flux from the boundary current (first term on the right hand side of equations 2.13a-b) but also on the ratio of the atmospheric forcing efficiency and the eddy heat flux from the front

current (second term on the right hand side of equations 2.13a-b). Equations 2.13c-e provide estimates for the slope currents and front current, where the first term on the right hand side indicates the temperature change due to heat loss to the atmosphere and the second (and third, equation 2.13e) represent the temperature change due to the lateral eddy heat flux.

Some insight into the *2basin\_full*-framework is obtained by investigating the limits of  $\mu/\epsilon$ , but keeping in mind that there are now four different eddy efficiency parameters;  $\epsilon_e$ ,  $\epsilon_w$ ,  $\epsilon_{fe}$  and  $\epsilon_{fw}$ . We consider the case where the eddy coefficients from the front are very small, and the eddy coefficients from the eastern and western boundary current are equal. In case the atmospheric forcing is relatively strong ( $\mu/\epsilon \gg 1$ ), both  $T_e$  and  $T_w$  approach the temperature of the atmosphere (equations 2.13a-b). As a result, the temperature difference between east and west becomes very small, which means that the front current transport is weak (equation 2.12b). Following equation 2.13f (the conservation of heat in the northernmost point) the end temperature of the slope current in the east,  $T_{se}$  will approach the starting temperature of the slope current in the west,  $T_{sw}$ . Therefore, under these circumstances the *2basin\_full*-framework reduces to the *1basin*-framework, but now including a linear change of the boundary current temperature.

The sensitivity changes when the system is in a weaker atmospheric forcing regime ( $\mu/\epsilon \ll 1$ ). Still considering the case where  $c_e = c_w$  (and  $c_{fe} = c_{fw} = 0$ ), the interior basin temperature now mainly depends on the difference in temperature between the slope current and the interior in these basins (equations 2.13a-b). As the boundary current in the east is warmer than in the west, just as for the *2basin\_simple*-framework, the lateral heat flux from the eastern boundary into the eastern interior basin will be larger than in the west, even for equal eddy coefficients. However, comparison of the results from the *2basin\_full*-framework and the *2basin\_simple*-framework (Figure 2.6) shows a large disagreement between the estimated temperatures, even if  $c_{fe} = c_{fw} = 0$  (compare solid and dashed lines). Particularly the estimated western basin interior temperature and the temperature of the outflow are lower ( $\Delta T > 1^\circ\text{C}$ ) in the *2basin\_simple*-framework compared to the *2basin\_full*-framework (gray and blue lines in Figure 2.6). There are two reasons for this difference.

First, in the *2basin\_full*-framework, the boundary currents and the front current change their temperature linearly in the downstream direction, whereas in the *2basin\_simple*-framework these are equal to their upstream values and hence warmer. Therefore, the heat lost to the atmosphere via surface fluxes and the heat lost to the interior via the lateral eddy heat fluxes are much larger in the *2basin\_simple*-framework than in the *2basin\_full*-framework, leading to lower estimates for the temperature of the outflow. Second, in the *2basin\_full*-framework the temperature at the upstream end of the boundary current in the west ( $T_{sw}$ ) does not only depend on the downstream temperature of the boundary current in the east ( $T_{se}$ ), but also on the downstream temperature of the front current ( $T_f$ ). Especially for small frontal eddy coefficients this leads to a larger  $T_{sw}$ , as the front current heat loss is minimal. Additionally, when the frontal eddy coefficients are non-zero, the lateral eddy heat flux to the interior of the western basin comes not only from the boundary current in the west (like in the *basin\_simple*-framework), but also from the front current. This leads to an even larger discrepancy between the estimated western basin interior temperatures (blue lines Figure 2.6).

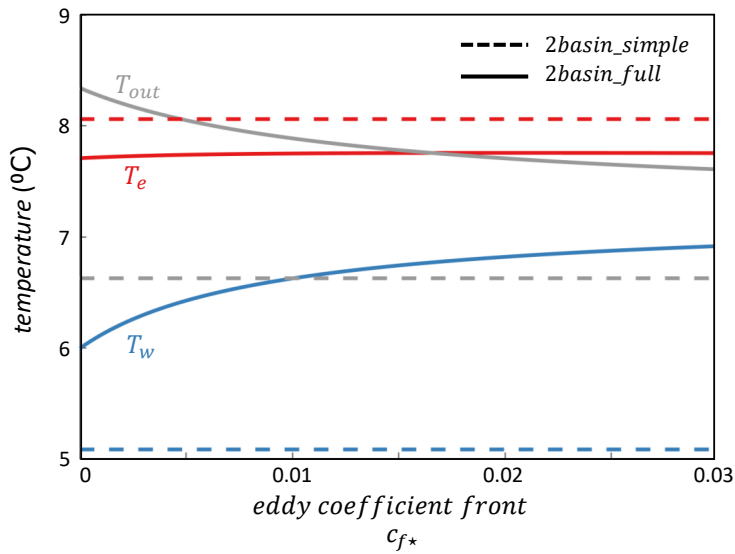


Figure 2.6: Temperature of the eastern interior ( $T_e$ ), the western interior ( $T_w$ ) and the outflowing water-mass ( $T_{out}$ ) as a function of the frontal eddy coefficient for the *2basin\_full*-framework (solid lines) and the *2basin\_simple*-framework (dashed lines). The  $c_{fe}$  and  $c_{fw}$  parameter are equal and represented by  $c_{f*}$  for this calculation.

Table 2.3: Key parameters of the numerical model sensitivity analysis

Run	$\Gamma$ ( $\text{W m}^{-2}\text{C}^{-1}$ )	$\mu$ ( $\times 10^{-8}$ )	symbol
1	4	1.2	square
2	8	2.5	square
<b>3</b>	<b>16</b>	<b>4.9</b>	star
4	32	9.8	square
5	64	19.6	square
6	128	39.2	square
7	256	78.4	square

In the *2basin\_full*-framework, the western basin interior (blue line) is more sensitive to changes in  $c_f$  than the eastern basin interior (red line), as the temperature difference between the front current and the western basin interior is always larger than the temperature gradient between the front and the eastern basin interior. However, overall the temperatures of the interior basins and the outflow seem relatively insensitive to changes in  $c_f$  (especially for  $c_f > 0.01$ ).

Results from the *2basin\_full*-framework show that the implementation of a gradual downstream cooling of the slope current and front current is at least as important for the estimated temperatures as the implementation of the frontal dynamics. The next section will show that, as a result of these implementations, the *2basin\_full*-framework is able to capture the dynamics of the numerical two-basin simulations better than the *2basin\_simple*-framework.

## 2.4. SENSITIVITY TO ATMOSPHERIC BUOYANCY FORCING

As discussed in section 2.2.2, the Lofoten Basin is less sensitive to changes in atmospheric forcing than the Greenland Basin due to the different eddy fluxes from the boundary current. In the *2basin\_full*-framework these two basins are connected via the slope current and via the front current. Therefore, the response of the whole system to changes in atmospheric forcing is expected to be not only non-uniform, but also non-linear.

To test this hypothesis, the solutions from the *1basin*-framework, the *2basin\_simple*-framework and the *2basin\_full*-framework are compared to the numerical simulations described in section 2.2.1 for different values of the non-dimensional parameter  $\mu$  (the measure of the atmospheric forcing efficiency). In the numerical simulations, the parameter  $\mu$  is varied by changing the restoring strength,  $\Gamma$  (see table 2.3 run 1-7). We choose to change  $\Gamma$  and not  $T_A$ , as changes in  $T_A$  only affect the range of possible solutions ( $T_A < T < T_{in}$ ), whereas changes in  $\Gamma$  provide insight into what controls the dynamics in the marginal sea. Sensitivity studies to a change in  $T_A$  have been performed, but did not lead to different insights than discussed in this section (see appendix 2.A).

The numerical simulations, the *2basin\_full*- and the *2basin\_simple*-frameworks all show, in contrast with the *1basin*-framework, that the temperature change of the two-basin marginal sea is non-uniform when a uniform change in atmospheric forcing is

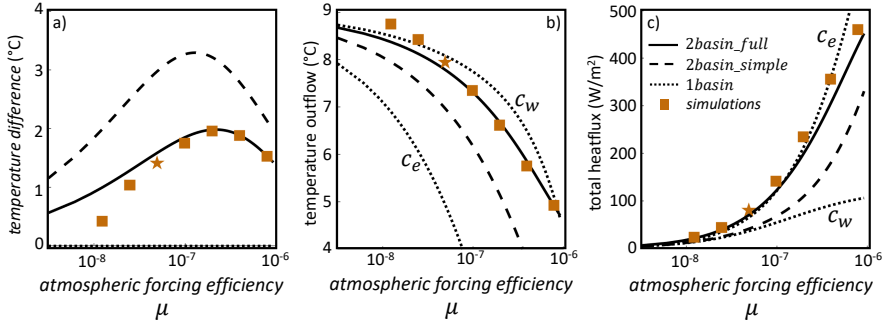


Figure 2.7: (a) Mean temperature difference between the eastern and western basins, (b) the temperature of the outflowing watermass and (c) the total heat loss to the atmosphere as a function of the non-dimensional parameter  $\mu$ . The temperatures and heat flux shown are diagnosed from the *2basin\_full*-framework (solid lines), from the *2basin\_simple*-framework (dashed lines), and from the numerical simulations (orange markers). Solutions from the *1basin*-framework using either the value of  $c_e$  or  $c_w$  are shown as well (dotted lines). The star indicates the reference simulation. Note that the horizontal axis is logarithmic.

applied (expressed by the non-dimensional parameter  $\mu$ , Figure 2.7a). The temperature difference between the eastern and western basin interior displays a maximum for  $\mu \sim 2 \times 10^{-7}$  for both the *2basin\_full*-framework (solid line in Figure 2.7a) and the simulations (squares in Figure 2.7a). Small values of  $\mu$  imply a minimal atmospheric cooling (Figure 2.7c), so both the eastern and western basins remain warm and the temperature gradient is therefore small (Figure 2.7a). For large values of  $\mu$ , both basins will cool toward the prescribed atmospheric temperature  $T_A$ . Therefore, for strong atmospheric forcing, the temperature gradient between east and west will be small as well. A more realistic case lies between these two limits (like the reference simulation, which is denoted by a star symbol in Figure 2.7a), where the temperature decrease in the western basin is larger than in the eastern basin (Figure 2.4), due to the combined effect of a colder boundary current in the west and a weaker eddy flux from the boundary to the western basin interior.

Qualitatively, the dependence of the estimated temperatures on the change in atmospheric forcing is quite similar for the *2basin\_full*-framework and the *2basin\_simple*-framework (Figure 2.7a-c). However, the *2basin\_full*-framework shows much better agreement with the numerical simulations. Again, the *2basin\_simple*-framework underestimates the temperature of the western basin (explaining the much larger temperature difference found in Figure 2.7a), the temperature of the outflow and the total heat loss to the atmosphere (dashed lines in Figure 2.7b and 2.7c). As discussed in section 2.3.2, this is because the equations describing the *2basin\_simple*-framework neither incorporate the eddy heat flux from the front current into the western basin interior, nor the downstream cooling of the boundary currents. The *1basin*-framework can only provide solutions for a basin with a constant eddy coefficient and no single choice for  $c_e$  or  $c_w$  can approach the results from the numerical simulations; where the estimated temperature of the outflow using  $c_w$  is rather well captured, using the same eddy coefficient, the sensitivity of the total heat loss to changes in atmospheric forcing is strongly underesti-

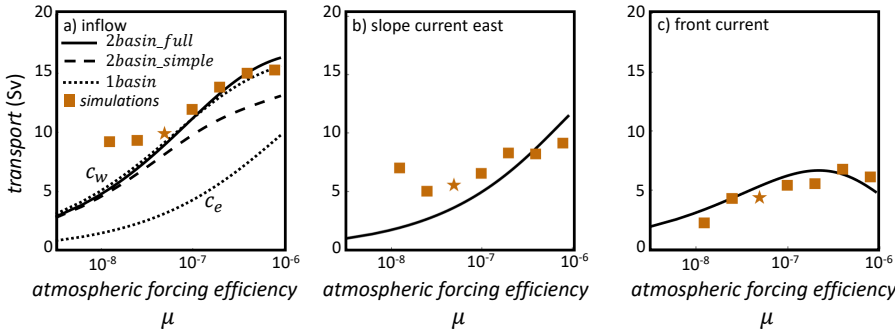


Figure 2.8: As in Figure 2.7, but now for the estimated volume transport (in Sv) of (a) the inflow ( $\Psi_{in}$ ), (b) the eastern slope current ( $\Psi_{se}$ ) and (c) the front current ( $\Psi_f$ ).

mated (dotted lines Figure 2.7b-c).

The non-linear response of the temperature gradient between the eastern and western basins to changes in atmospheric forcing seen in Figure 2.7a has implications for the dynamics in the two-basin marginal sea. In the  $2basin\_full$ -framework, the heat balance derived for each current implies that the total heat transported into the marginal sea is equal to the total amount of heat lost to the atmosphere (equation 2.10). Since  $T_{in}$  is kept constant, the inflow ( $\Psi_{in}$ ) increases when the atmospheric forcing is stronger (solid line in Figure 2.8a). The results from the numerical simulations corroborate this relation between the heat loss and the inflow (squares in Figure 2.8a).

In the  $2basin\_full$ -framework the inflow separates in the front current and the slope current along the eastern boundary (see equation 2.11). Furthermore, the strength of the front current is set by the temperature difference between the eastern and western basin (see equation 2.12). Therefore, the volume transports along the front current ( $\Psi_f$ ) and along the slope current in the east ( $\Psi_{se}$ ) are co-dependent, both on the total heat loss to the atmosphere and on the temperature gradient between the eastern and western basins (solid lines in Figure 2.8b and 2.8c). This provides a dynamical explanation for the observed anticorrelation between the Atlantic Water transport along the front current and the slope current (see also appendix 2.A).

The magnitude of the volume transport for the slope current and the front current diagnosed from the numerical simulations and its response to changes in atmospheric forcing are captured well by the  $2basin\_full$ -framework (compare squares and solid lines in Figure 2.8b and 2.8c). This indicates that the dynamics in the numerical simulations match the assumptions made in the conceptual model. However, for small values of  $\mu$  the numerical simulations predict larger volume transports of the slope current (Figure 2.8b). One possible explanation for this discrepancy is the artificial restoring region in the numerical simulations, where not only temperature, but also the velocity is prescribed. Therefore, the numerical simulations might overestimate the volume transport into the marginal sea for relatively weak atmospheric forcing. This prescribed veloc-

ity also impacts the temperatures of the interior basins and the outflow, which are all slightly warmer than the *2basin\_full*-framework predicts for weak atmospheric forcing (Figures 2.7a-b). However, the only forcing mechanism in the conceptual model is the pull of warm water into the Nordic Seas from heat loss to the atmosphere as assumed in e.g. *Spall* (2011). So, the conceptual model could also underestimate the transport of the inflow, as for example the role of wind forcing is neglected (see e.g. *Orvik and Skagseth*, 2005; *Sandø and Furevik*, 2008). The overestimation of the volume transport in the numerical simulations could then be interpreted as a minimal inflow transport from a wind-driven circulation.

So far, we have shown that a two-basin approach leads to a non-linear response of the marginal sea to changes in atmospheric forcing. The temperature gradient between the eastern and western basins (and as such the strength of the front current) can either increase or decrease for the same change in  $\mu$  depending on whether the atmospheric forcing is strong or weak (Figure 2.7a and Figure 2.8c). To be able to predict which response can be expected, some insight in the dependence of  $\mu_{max}$  ( $\mu$  for which the maximum temperature gradient is found) on the eddy coefficients is required.

The *2basin\_full*-framework predicts a similar sensitivity of the temperature difference to the eddy coefficients as discussed in section 2.2.2 (Figure 2.5) for the *2basin\_simple*-framework; increasing the eddy coefficient in the east (west) leads to a larger (smaller) temperature difference between the two basins. Figure 2.9, however, also shows that the maximum of the temperature difference is found for larger values of  $\mu$  (stronger atmospheric forcing) when the eddy coefficients increase. Due to the complexity of equation 2.13, it is not possible to find an analytical solution for  $\mu_{max}$  and  $\Delta T_{max}$  that describes the dependence of the maximum of the temperature gradient between the eastern and western interior basins on the eddy coefficients  $c_e$  and  $c_w$ . However, investigation of the maxima shows that for a linear increase in either  $c_e$  or  $c_w$  an exponential increase in  $\mu_{max}$  is needed to reach a maximum in the temperature gradient (not shown).

In summary, these results show that the *2basin\_full*-framework captures the dynamics of the idealized model simulations by providing good estimates for both the temperature of the different watermasses in the marginal sea and for the transport estimates of the inflow, the front current and the slope current along the eastern boundary. Furthermore, analysis of the sensitivity of the marginal sea dynamics to changes in atmospheric forcing has shown that the two-basin approach leads to a non-linear response of the temperature gradient between the eastern and western interior basins. As a consequence, changes in transport along the front current depend not only on the eddy efficiency near the eastern and western boundaries, but also on the strength of the atmospheric forcing.

## 2.5. DISCUSSION AND CONCLUSIONS

In this study, we have proposed a dynamical system of a two-basin marginal sea subject to buoyancy loss that better addresses the complexity of the Nordic Seas compared to previous one-basin studies described by e.g. *Iovino et al.* (2008) and *Spall* (2011). The conceptual model (the *2basin\_full*-framework) shows good agreement with idealized numerical simulations for a wide range in atmospheric forcing, implying that the physics

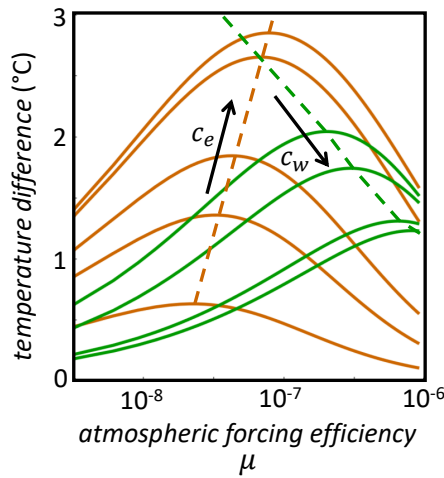


Figure 2.9: Temperature difference between the eastern and western basins as a function of the non-dimensional parameter  $\mu$  (atmospheric forcing efficiency) for different values of the eddy efficiency parameters  $c_e$  (orange curves) and  $c_w$  (green curves). The dashed lines trace the maximum of the temperature difference curve, where the arrow indicates an increase in  $c_e$  (keeping  $c_w$  constant, orange dashed line) and an increase in  $c_w$  (keeping  $c_e$  constant, dashed green line). Note that the horizontal axis is logarithmic.

of the conceptual model is relevant for a marginal sea like the Nordic Seas (Figures 2.7 and 2.8). To capture the hydrographic and dynamical differences of the Lofoten and the Greenland Basins, a two-basin geometry is essential. Additionally, we have shown that a simple extension of the one-basin conceptual framework described in *Spall* (2011) (the *2basin\_simple*-framework, section 2.3.1) is not sufficient to capture the interactions between the two basins. Instead, to ensure a good comparison with the numerical two-basin marginal sea simulations, the inclusion of a front current and a downstream cooling of both the slope current and the front current is required (section 2.3.2 and Figures 2.7 and 2.8). Doing so, the *2basin\_full*-framework has elucidated the importance of the mid-ocean ridge for separating two dynamically different regions and the essential role of the front current in governing the heat and volume budget of the Nordic Seas.

The *2basin\_full*-framework provides estimates for the interior basin temperature of the Lofoten and Greenland Basins, the temperature of the outflow and the transport of the inflow, slope current and front current. The dynamics of the marginal sea are mainly controlled by the eddy fluxes from the slope current and front current and the strength of the atmospheric forcing, similar to *Spall* (2011). The extension from the *1basin*-framework to the *2basin\_simple*-framework has shown that the sensitivity of the downstream (western) basin to changes in atmospheric forcing depends on the properties of the upstream (eastern) basin (Figure 2.5). Due to the addition of the front current in the *2basin\_full*-framework, the upstream (eastern) basin is also sensitive to the properties of the downstream (western) basin, as the frontal strength and therefore the lateral eddy heat flux from the front depends on the temperature of both basins (Figure 2.9).

The Lofoten Basin shows a weaker sensitivity to changes in the atmosphere than the Greenland Basin due to the enhanced eddy activity in the east (Figure 2.4). As the Lofoten Basin and the Greenland Basin are connected via the slope current and front current, both the numerical two-basin simulations and the *2basin\_full*-framework show a non-uniform and non-linear response to changes in atmospheric forcing. As a result, the temperature gradient between east and west can either increase or decrease when the atmospheric forcing weakens, depending on the strength of the atmospheric forcing before the weakening starts (Figure 2.7a), and on the eddy coefficients of the eastern and western basins (Figure 2.9). In case of the present day Nordic Seas, based on the reference simulation (indicated by the star in Figures 2.7a and 2.8c) and the conceptual model, one would expect a decrease in the density gradient across the mid-ocean ridge and a weakening of the baroclinic component of the outer branch of the NwAC when the atmospheric forcing weakens.

The front current strength is of similar magnitude compared to the slope current in both the conceptual model and the numerical simulations. This is in agreement with recent observations of the front current from glider measurements (*Bosse and Fer, 2019*). However, it is important to note that the characteristics of the slope and front current in the conceptual model are idealized in order to keep the number of free parameters at a minimum.

First of all, the derivation of the theoretical framework is based on only baroclinic currents. Observations have indicated that both the slope current and the front current have a substantial barotropic component (e.g. *Orvik et al., 2001; Bosse and Fer, 2019*) and this could influence the derived heat budget in various ways. If the barotropic component would be included, the currents will likely be faster. As a result, the residence time in the mean flow is shorter and the subsequent temperature change due to direct heat loss to the atmosphere will be less. Furthermore, the barotropic component might induce other types of flow instabilities. It is however difficult to include a parameterization for those heat flux mechanisms in the conceptual model. Therefore, the sensitivity of the two-basin marginal sea to changes in the surface buoyancy forcing presented in this study should be interpreted as an upper limit, due to the omission of the barotropic component.

Second, in the *2basin\_full*-framework, the depth and width of the slope current and front current are chosen to be equal. The transect shown in Figure 2.2c indicates that the front current is much deeper than the slope current in this simulation. Regarding observations, a level of no motion is often not found, due to the strong barotropic character of the currents (e.g. *Orvik et al., 2001; Bosse and Fer, 2019*). However, based on previous idealized model studies (e.g. *Iovino et al., 2008*) it is likely that the depth of the baroclinic component is related to the depth of the topographic sill (the Greenland-Scotland Ridge), which corroborates our choice for a constant depth. The width of the slope current and the width of the front current are likely to vary in reality. Although we chose to constrain the depth, width and baroclinic character of the slope and front currents in the conceptual model, the estimated temperatures compare well to the numerical simulations (Figure 2.7), where these characteristics are clearly not set nor constant.

The conceptual model discussed in this chapter represents a highly idealized representation of the Nordic Seas, as the main aim of this study was to investigate the sen-

sitivity of a two-basin marginal sea in comparison to the more common one-basin description. However, there are several components that could benefit from further investigation in order to better understand and predict the sensitivity of the Nordic Seas to changes in atmospheric forcing. First, in the *2basin\_full*-framework the only exchange between the eastern and western basins is via the slope current. *Spall* (2010) has shown that there is also a possible heat exchange between the interior of the Lofoten and Greenland basins as a result of the frontal current instability that impacts the stratification of the Lofoten Basin (see also appendix 2.A). Better understanding of what controls this exchange is needed to appropriately integrate this mechanism in our conceptual framework.

Furthermore, our conceptual model focuses on the role of temperature regarding atmospheric forcing and ocean dynamics. Salinity variations (or fresh water fluxes) can play an important role for e.g. the strength of the density gradient between the Lofoten and Greenland Basins, the dense water formation in the interior (e.g. *Rosby et al.*, 2009b; *Brakstad et al.*, 2019), the atmospheric buoyancy forcing and slope current dynamics due to river run-off (*Lambert et al.*, 2018). *Spall* (2012) has investigated the role of precipitation in a one-basin marginal sea and shows that abrupt transitions are possible due to a shut down of convection. Furthermore, in both the theoretical framework and the idealized model simulations a linear equation of state is used with a constant thermal expansion coefficient, which is not necessarily appropriate for the Nordic Seas where temperature differences are large (e.g. *Mork and Skagseth*, 2005). Also the wind-driven dynamics of the real system are likely to play an important role for the variability of the processes discussed in this chapter. All these processes might be important, but the main focus of this chapter was to design a conceptual model to outline the importance of the two-basin character of the Nordic Seas. Extending the two-basin conceptual framework to include some of these processes could enhance its predictive value.

In summary, this study has shown that a one-basin approach is not suitable to investigate the response of a marginal sea like the Nordic Seas to changes in atmospheric buoyancy forcing. Instead, the results from the two-basin conceptual framework indicate that the dynamics of the eastern basin are linked to the dynamics in the western basin and that the response of the two basins combined is non-linear. Therefore, for full understanding of observed changes in either the Lofoten or the Greenland Basin, both basins need to be considered. Furthermore, the conceptual model developed in our study shows that the presence of the ridge and the front current amplify the sensitivity of the Nordic Seas to changes in atmospheric buoyancy forcing (Figure 2.6), both by increasing the net heat loss to the atmosphere (Figure 2.7c) and by controlling the transport through the Nordic Seas (Figure 2.8). Further studies and observations of the front current dynamics are therefore important to better understand its role for the formation and export of dense water masses from the Nordic Seas.

---

---

# Appendix

---

---

**2**

## 2.A. SENSITIVITY TO NON-UNIFORM ATMOSPHERIC FORCING

In chapter 2 both the conceptual model and the idealized model simulations revealed the response of a two-basin marginal sea to uniform changes in the atmospheric buoyancy forcing. In this appendix, a short discussion is added on the response of the two-basin marginal sea to a non-uniform change in the atmospheric forcing by changing the atmospheric temperature over the western basin only. Our main goal is to investigate whether the conclusions drawn in chapter 2 regarding the changes in hydrography and circulation still hold.

### METHOD

The same model configuration is used as described in section 2.2.1. However, instead of changing the restoring strength  $\Gamma$  as done in section 2.4, a non-uniform atmospheric buoyancy forcing is applied by keeping the prescribed atmospheric temperature,  $T_A$ , constant over the eastern basin ( $T_A = 4^\circ$ ) and by changing  $T_A$  over the western basin (to respectively  $3^\circ\text{C}$ , *west3*,  $3.5^\circ\text{C}$ , *west3.5*,  $4.5^\circ\text{C}$ , *west4.5*, and  $5^\circ\text{C}$ , *west5*). These simulations result in an asymmetric surface heat flux, where the west-east temperature gradient increases when the western basin receives a stronger cooling (and vice versa). The simulations are run to equilibrium and means over the final 5 years are used to analyze the temperature and velocity fields.

### RESULTS

The non-uniform changes in the surface forcing affect the interior basin temperature as expected: the sea surface temperature (SST) in the western basin decreases when the atmospheric temperature decreases (stronger restoring) and vice versa (dashed temperature profiles in Figure 2.10). The restoring across the eastern basin was not altered between the simulations and as a result, the mean SST across the eastern basin does not change (see solid temperature profiles in Figure 2.10). However, the stratification in the eastern basin and the spatial pattern of the temperature at the sea surface in the east do appear to be sensitive to the changes in the surface forcing across the western basin.

The stratification in the eastern basin is stronger in the cold scenarios (see steeper thermocline in Figure 2.10). In the idealized model simulations of *Spall* (2010), a similar response was seen when changing the slope of the mid-ocean ridge (instead of changing the atmospheric forcing as done here). The slope has a stabilizing effect on the front current which reduces the baroclinic instability. As a result, *Spall* (2010) showed that the eddy mass transport across the ridge weakened and the strength of the thermocline in the east decreased. Furthermore, *Spall* (2010) discussed that the depth of the thermocline is set by the depth of the sill in the south and of the mid-ocean ridge. This is in line with the results of our simulations; the depth of the thermocline is constant and does not depend on the strength of the atmospheric cooling. So the increase in the eastern basin stratification in the colder scenarios is most likely a result of the increased density gradient between the two basins and therefore the stronger exchange across the mid-ocean ridge that transports a colder watermass from the west to the east below the thermocline.

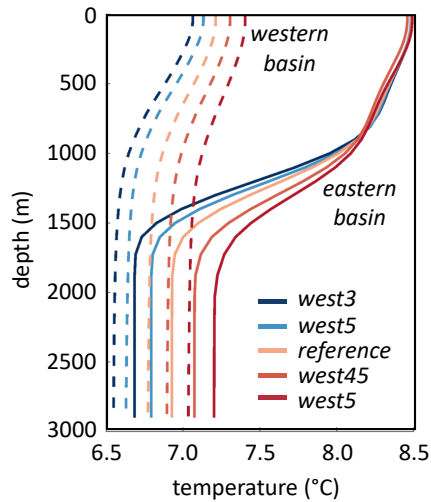


Figure 2.10: Mean temperature profile in the eastern basin (solid lines) and the western basin (dashed lines) for each simulation. The mean is calculated from 700-1200 km in the meridional direction and from 100-400km (600-900km) in the zonal direction for the western (eastern) basin.

At the surface of the eastern basin, the SST response to changes in atmospheric forcing shows a dipole pattern (Figure 2.11). For colder scenarios than the reference simulation, the northern part of the eastern basin cools, whereas the southern part of the eastern basin warms (shading in Figure 2.11a-b). In the warmer scenarios, the opposite is seen (Figure 2.11c-d).

This SST anomaly in the eastern basin can be explained by the changes in the surface eddy kinetic energy (EKE), as shown in Figure 2.11 by red (increased EKE) and blue (decreased EKE) contours. The region along the mid-ocean ridge shows an increase in EKE for the colder scenarios and a decrease in EKE for the warmer scenarios (red and blue contours at  $x = 500$  km in Figure 2.11a-d). In contrast, near the steep slope of the eastern basin (near  $y = 1100$  km), the surface EKE decreases in the colder scenarios and increases in the warmer scenarios. Since the eddies transport heat from the warm boundary current to the interior of the eastern basin, it is not surprising that the SST response shows such a strong correlation with the increased/decreased EKE pattern.

The changes in the EKE pattern are related to the strength of the slope current and the front current. Recall that the inflowing water east of the island separates to follow different branches in the eastern basin. The bar-diagram in Figure 2.12a shows how the transport carried by the inflow is separated in transport along the front (filled bars), transport along the slope (hatched bars) and transport along a weak branch that continues across the ridge to the west (dotted bars). Where in the coldest scenario (*west3*) most of the inflowing waters take the path along the mid-ocean ridge (67%), in the warmest scenario

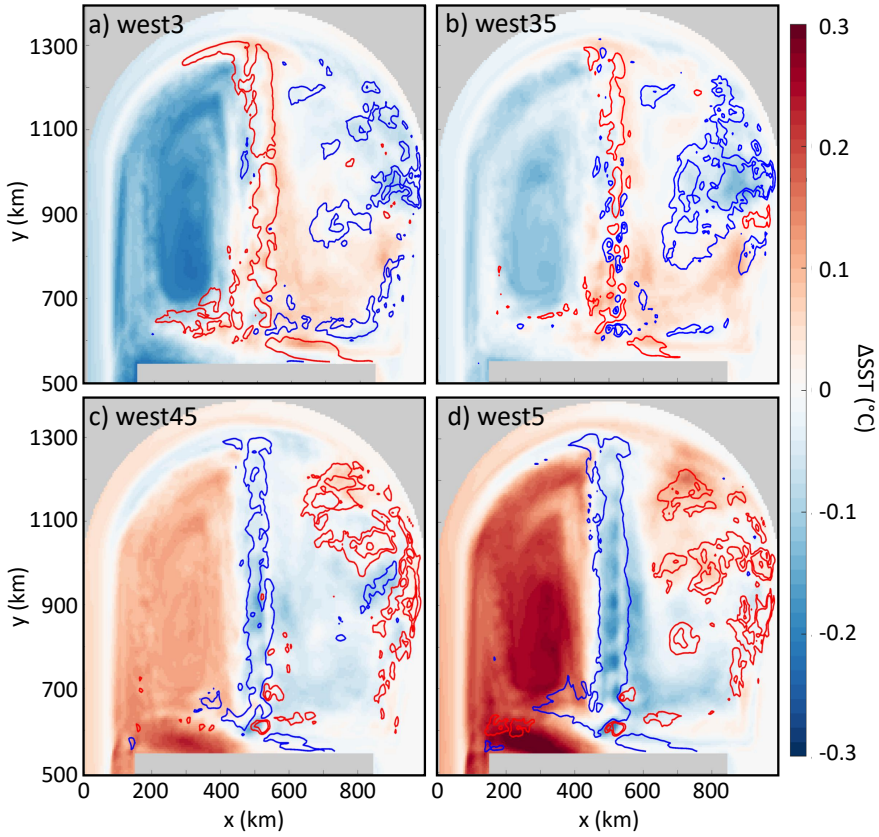


Figure 2.11: Anomaly of SST (shading) and surface EKE contours with respect to the reference simulation for the (a) *west3* simulation, (b) *west35* simulation, (c) *west45* simulation and (d) *west5* simulation. Contours show the  $20 \text{ cm}^2 \text{ s}^{-2}$  and  $50 \text{ cm}^2 \text{ s}^{-2}$  surface EKE anomaly for increased (in red) and decreased (in blue) EKE compared to the reference simulation.

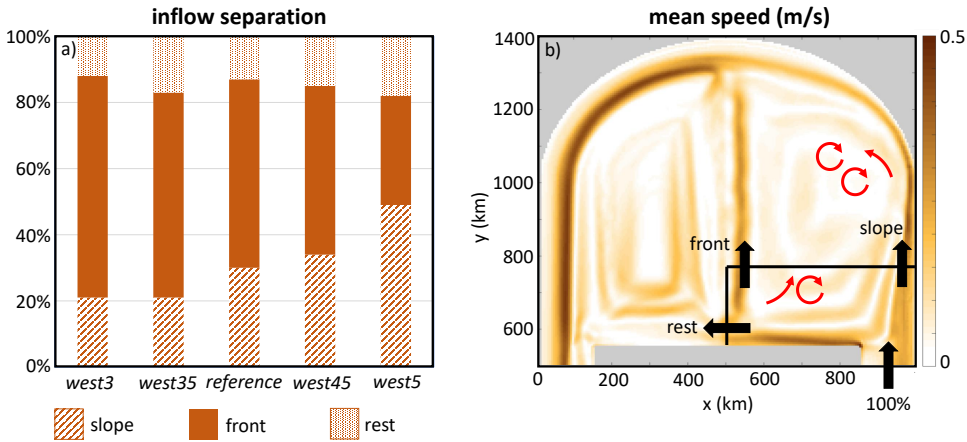


Figure 2.12: (a) Separation of the inflow transport east of the island into the slope current (hatched bars), the front current (filled bars) and the flow along the island to the west ('rest', dotted bars) for all five scenarios. Note that this separation is indicated in % and not by absolute volume transport as done in Figure 2.8. (b) Surface speed of the reference simulation (shading) and the location of the slope current, the front current and the westward flow along the island. The red arrows schematize the direction of the lateral eddy heat fluxes.

(*west5*) this transport reduces to only 33% of the total inflow and most transport takes place along the eastern boundary (49%).

Just as discussed in section 2.4, the stronger front current along the mid-ocean ridge is a result of the increased temperature gradient between the eastern and western basins. As the slope and front currents are dynamically linked, the slope current has to adjust to changes in the front current, and as a result its strength reduces (increases) for the colder (warmer) scenario. The strength of the flow impacts the baroclinic instability due to the increase in vertical shear. This explains the changes seen in the surface EKE field (Figure 2.11). The spatial dipole pattern in the eastern basin SST is caused by the fact that the lateral eddy fluxes from the front current and the slope current are strongest at different latitudes (see schematic Figure 2.12b).

In addition to the changes in the front and slope current strengths, the changes in stratification can explain the changes seen in the instability of the eastern boundary current as well. As described in section 2.2.2, the baroclinic instability depends on the ratio of the isopycnal slope and the bottom slope. When the stratification increases, the isopycnal slope weakens and the growth rate and scale of the most unstable waves decrease. The opposite is true for a decrease in the stratification as seen in the warm scenarios.

## CONCLUSIONS

The sensitivity study performed in this appendix corroborates the results presented in chapter 2. The analysis shows that the hydrography and the dynamics in the eastern basin are altered by the remote change in surface forcing across the western basin. The two sub-basins are connected via the mid-ocean ridge, and the strength and dynamics

of the front current play an important role for the response in the east. This highlights, just as concluded in chapter 2, that the eastern, upstream basin is sensitive to changes in the western, downstream basin; as the temperature gradient between the eastern and western basin increases in the colder scenarios, the path along the front current is preferred and the lateral eddy fluxes from the slope current into the eastern basin interior weaken. However, at the same time the lateral eddy heat flux from the front into the eastern basin increases and therefore the mean sea surface temperature in the eastern basin does not change.

The results presented in this appendix further show that the western basin remains colder than the eastern basin, even when the atmosphere across the western basin is warmer than over the eastern basin. This again highlights the differences in dynamics between the Lofoten Basin and the Greenland Basin as the lateral eddy heat flux in the western basin is weak.

# 3

## PATHWAYS AND WATERMASS TRANSFORMATION ALONG AND ACROSS THE MOHN-KNIPOVICH RIDGE IN THE NORDIC SEAS

*Atlantic Water takes various pathways through the Nordic Seas and its transformation to denser waters forms a crucial connection to the lower limb of the Atlantic Meridional Overturning Circulation. Circulation maps often schematize two distinct pathways of Atlantic Water; one following the Norwegian Atlantic Slope Current along the continental slope of Norway and one following the Norwegian Atlantic Front Current along the Mohn and Knipovich Ridges. In this chapter, the connectivity between the northward flow along these ridges is investigated. Analyzing trajectories of surface drifters and ARGO floats, we find that only 8% of the floats that travel near the mid-ocean ridges take the frontal pathway to the north. Indeed, by tracing numerical particles in a realistic numerical simulation, we estimate that 1/3rd of the watermass traveling along the Mohn Ridge follows the 2500 m isobath eastward and joins the slope current, instead of flowing north along the Knipovich Ridge. Furthermore, north of 74° N, multiple exchanges between the slope current and the front current are observed. Therefore, the slope current and front current are less isolated than often schematized. Additionally, the observational data set reveals substantial cross-ridge exchange; 44% of the floats approaching the mid-ocean ridges cross the ridge. Results from numerical simulations indicate that the cross-ridge exchange leads to a stronger cooling and freshening of the Atlantic Water along the front. Deployments of floats near the mid-ocean ridges are needed to investigate the pathway of Atlantic Water and its exchange across the ridge in more detail.*

---

Results presented in this chapter have been published as: S.L. Ypma, Georgiou, S., Dugstad, J.S., Pietrzak, J.D. and Katsman, C.A., Pathways and water mass transformation along and across the Mohn-Knipovich Ridge in the Nordic Seas, *Journal of Geophysical Research: Oceans*, DOI:10.1029/2020JC016075

### 3.1. INTRODUCTION

The Nordic Seas are characterized by a warm and saline Atlantic watermass in the east and a fresh and cold Arctic watermass in the west. Due to the anomalously warm and salty eastern basin, more than 60% of the total heat loss in the northern North Atlantic Ocean occurs in the Nordic Seas (*Chafik and Rossby, 2019*). As such, the transformed watermasses leaving the Nordic Seas play a major role for the strength of the Meridional Overturning Circulation (MOC, e.g. *Chafik and Rossby, 2019; Lozier et al., 2019*). The upper limb of the MOC carries the warm Atlantic Water (AW) into the Nordic Seas via different branches (Figure 3.1a, *Orvik and Niiler, 2002*). The AW transforms to denser watermasses along its path northward (e.g. *Bosse et al., 2018*), from where it flows toward the Arctic Ocean or returns south within the East Greenland Current (EGC). This gradual transformation of AW is seen as the main contributor to the variability of the dense water leaving the Nordic Seas via the overflows (i.e. *Mauritzen, 1996; Eldevik et al., 2009*).

However, the AW in the eastern basin of the Nordic Seas cannot be seen as one homogeneous layer that is modified in a uniform way; upon entering the Nordic Seas the AW follows various branches that affect different parts of the Nordic Seas (*Hansen and Østerhus, 2000*). AW circulation in the Nordic Seas is typically schematized by a two-branch structure (e.g. Figure 1a in *Dugstad et al., 2019b*). One branch, the Norwegian Atlantic Slope Current (NwASC, hereinafter the slope current), follows the Norwegian continental slope as a topographically controlled barotropic current. The second branch, the Norwegian Atlantic Front Current (NwAFC, hereinafter the front current), is a baroclinic jet associated with the Arctic Front (AF, *Orvik and Niiler, 2002*). The AF is characterized by a strong thermocline and halocline that separate the Arctic Water in the west from the Atlantic Water in the east (Figure 3.1b, *Bosse and Fer, 2019*). This density front is aligned with the mid-ocean topographic ridges in the Nordic Seas; the Mohn Ridge and the Knipovich Ridge (see Figure 3.1a). Along the Knipovich Ridge, the front current is often referred to as the western branch of the West Spitsbergen Current (*Walczowski, 2013*).

Hydrographic measurements at various sections across the AF reveal strong horizontal gradients in temperature and salinity along the topographic slope, and show a clear northward flow along the ridges (i.e. *van Aken et al., 1995; Rossby et al., 2009b; Walczowski, 2013*). Recent estimates from glider transects by *Bosse and Fer (2019)* indicate that the AW transport along the front current is at least as strong as the transport along the slope current ( $\sim 3.2$  Sv). It is therefore surprising that barely any surface drifters (*Poulain et al., 1996; Orvik and Niiler, 2002*) or RAFOS floats (*Rossby et al., 2009a*) follow this frontal pathway depicted in Figure 3.1a. The conclusion drawn by *Orvik and Niiler (2002)*, that the NwAC maintains a two branch structure throughout the Nordic Seas, was based on a composite of many partial pathways of surface drifters. Therefore, it can be questioned whether these pathways also apply to water parcels that come from south of  $65^\circ\text{N}$  and travel all the way to the Arctic. The fact that very few surface drifters follow the Mohn-Knipovich Ridge may be attributed to the non-uniform deployment and relatively high mortality of surface drifters in the Nordic Seas (*Koszalka et al., 2011, 2013a*). But still, it is as of yet unclear whether the northward flow along the Mohn Ridge is connected to the downstream northward flow along the Knipovich Ridge in a Lagrangian sense.

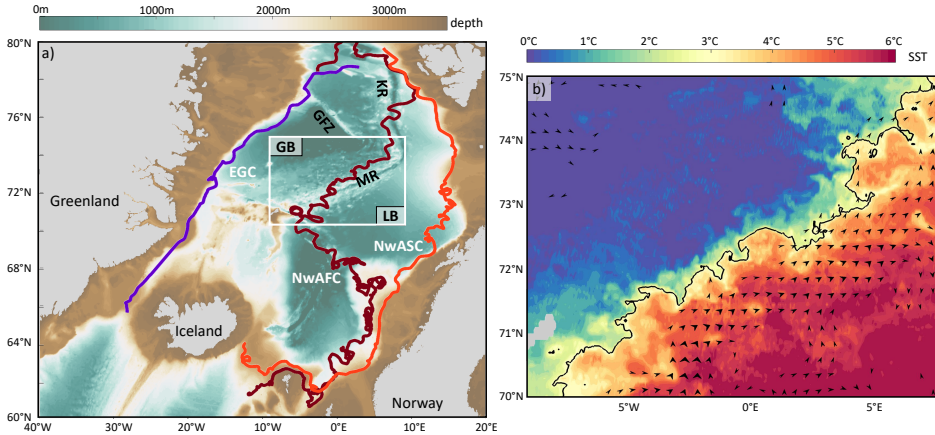


Figure 3.1: (a) Bathymetry of the Nordic Seas and pathways of three example surface drifters that follow the Norwegian Atlantic Slope Current (NwASC, orange path), the Norwegian Atlantic Front Current (NwAFC, dark red path) and the East Greenland Current (EGC, blue path) respectively. The bathymetric features pertinent for this study are marked: the Mohn Ridge (MR), the Knipovich Ridge (KR) and the Greenland Fracture Zone (GFZ). Bathymetry is from ETOPO1 (*Smith and Sandwell, 1997*). (b) Sea surface temperature (SST) from AVHRR sensor at the location of the white box indicated in the left panel; image on April 29, 2017, showing the Arctic Front ( $3^{\circ}\text{C}$  contour is highlighted). The black arrows show the mean geostrophic velocity from AVISO satellite altimetry for the year 2017 for velocities stronger than  $0.04\text{ m s}^{-1}$ .

Apart from AW modification in the along-front direction, across-front fluxes resulting from baroclinic instability of the front can impact watermass transformation processes. Evidence for such cross-frontal exchange is described by *Budéus and Ronski (2009)*, who observed patches of Atlantic Water in the Greenland Basin originating from the AF. In addition, analysis of satellite measurements and estimates from surface drifter data show enhanced eddy kinetic energy (EKE) along the Mohn Ridge (*Koszalka et al., 2011; Trodahl and Isachsen, 2018*). Analyses of hydrographic in situ measurements yield an eddy heat flux of  $8\text{--}17.7 \times 10^{12}\text{ W}$  across the AF (*van Aken et al., 1995; Walczowski, 2013*, respectively). That is,  $\sim 30\%$  of the total heat loss of the eastern basins in the Nordic Seas is due to eddy heat exchange with the colder and fresher western basins (*Segtnan et al., 2011*). The warm anticyclonic eddies shed by the front from east to west can be important for the deep convection processes in the Greenland Basin as they provide a salt flux that enhances convection (*Brakstad et al., 2019*). In turn, the eddy-induced exchanges across the ridge cool and freshen the AW (*Saloranta and Svendsen, 2001*), which affects the overturning in the Nordic Seas and the properties of the watermasses entering the Arctic.

However, no significant cross-ridge exchange is captured by trajectories of surface drifters (*Poulain et al., 1996*), subsurface RAFOS floats (*Rossby et al., 2009a*) or ARGO floats (*Latarius and Quadfasel, 2016*). In fact, *Rossby et al. (2009b)* suggest that cross-ridge exchange is unlikely, as the AF density gradient is strong and tightly locked to the sloping topography. Furthermore, analyses of a SF6 tracer, injected in the Greenland basin in 1996, do not show significant mixing between the Greenland Basin and the Lo-

foten Basin (*Olsson et al.*, 2005; *Messias et al.*, 2008). It is therefore unclear how important the cross-front transport is for watermass transformations in the Nordic Seas.

Successive analyses of the growing Lagrangian observational data set have shown to continuously improve understanding of the Nordic Seas surface- and mid-depth circulation and variability (*Poulain et al.*, 1996; *Orvik and Niiler*, 2002; *Rosby et al.*, 2009a; *Voet et al.*, 2010; *Koszalka et al.*, 2011; *Dugstad et al.*, 2019b). Therefore, in this chapter we revisit the surface drifter and ARGO float trajectories with a special focus on trajectories along and across the Mohn and Knipovich Ridges. In order to investigate the connection between the flow along the Mohn and Knipovich Ridges and possible pathways across the ridges, results from the observed trajectories are compared to trajectories from a realistic, high resolution numerical calculation (section 3.3). Furthermore, the importance of baroclinic cross-ridge exchange for watermass transformation along AW pathways is investigated in an idealized numerical configuration of the Lofoten and Greenland Basins as well (section 3.4). A discussion and conclusions are provided in section 3.5.

## 3.2. METHODS

When investigating pathways and connectivity between different ocean branches, a Lagrangian approach is most suitable (*Van Sebille et al.*, 2018; *Bower et al.*, 2019). Therefore, we use all trajectories available from surface drifters and ARGO floats that at some moment during their lifetime passed through the Nordic Seas. Details on this data set and the selection procedure to analyze the flow along and across the Mohn and Knipovich Ridges are provided in section 3.2.1. The observed trajectories are limited not only in quantity, but also in their capability to trace watermasses. As ARGO floats and surface drifters float at a fixed depth, they are unable to represent any vertical displacement of watermasses, which is likely to occur in the Nordic Seas. Therefore, we performed additional Lagrangian studies to evaluate pathways and watermass transformation of AW along the mid-ocean ridges using both a high resolution, realistic ocean model (section 3.2.2) and an idealized numerical simulation (section 3.2.3).

### 3.2.1. TRAJECTORIES FROM OBSERVATIONS

The surface drifter data set is obtained from the Global Drifter Program (GDP) database<sup>1</sup>. The surface drifters consist of a buoy at the surface and a sub-surface drogue and their trajectories represent the circulation at 15 m depth. Trajectories of surface drifters that have lost their drogue are not taken into account. A quality-control and interpolation of each drifter position to 6 hour intervals were performed by the AOML/NOAA Drifter Data Assembly Center (*Lumpkin and Pazos*, 2007).

In contrast to surface drifters, ARGO floats typically drift at 1000 m depth. Every 10 days, they descend to 2000 m depth and subsequently ascend to the surface profiling the water column. At the surface, they transmit their data and position to a satellite and return to their parking depth. Tracing the profiling location of ARGO floats visualizes the circulation at mid-depth (*Voet et al.*, 2010). The ARGO float data is obtained from the

<sup>1</sup><https://www.aoml.noaa.gov/phod/gdp/> updated through June 30 2019 when downloaded on December 3, 2019

International Argo Program (downloaded on Nov 18, 2019 from <https://coriolis.eu.org>) and only quality-controlled profiles are taken into account.

At time of download (Dec 3, 2019), 564 surface drifters and 283 ARGO floats had been drifting through the Nordic Seas. To investigate the flow along and across the Mohn and Knipovich Ridges, trajectories that came in close vicinity to the mid-ocean ridges are selected. To this end, the mid-ocean ridges are schematized by a straight line and an area is defined by a  $2^\circ$  radius from the ridges (red shading in Figure 3.2a). Any float or drifter entering this area is used for analysis. This way, only 32 surface drifters and 52 ARGO floats remain, which allows for subsequent separation based on individual pathways by eye.

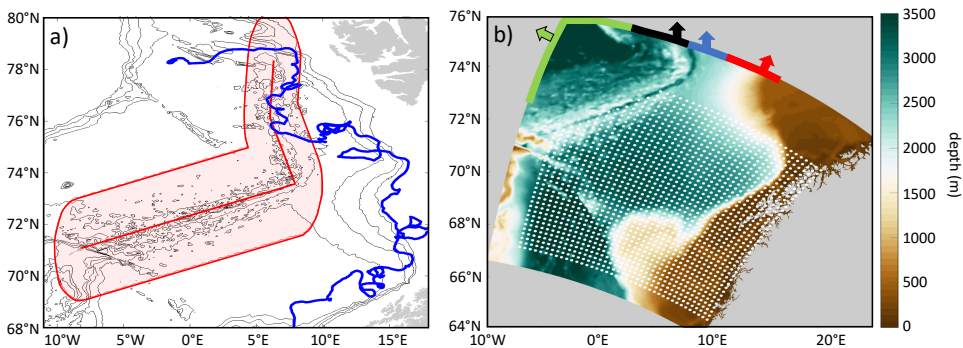


Figure 3.2: (a) Selection area (red shading) for floats traveling close to the Mohn and Knipovich Ridges. Red straight line follows the summit of the Mohn and Knipovich Ridges. The blue line shows an example path of a surface drifter following part of the Knipovich Ridge. The 1000 m, 1500 m, 2000 m and 2500 m isobaths are shown in gray. (b) Bathymetry of the realistic numerical simulation described in section 3.2.2. White dots indicate the deployment location of particles at 15 m, 200 m and 500 m depth. The thick colored lines show the transects used to separate the outflowing particles.

### 3.2.2. TRAJECTORIES FROM A REALISTIC OCEAN MODEL

As the number of surface drifters and ARGO floats in the vicinity of the mid-ocean ridges is relatively low, results from the observed trajectories are compared to trajectories from a realistic ocean model; the Regional Ocean Modeling System (ROMS) applied to the eastern Nordic Seas (Figure 3.2b). The model has 800 m horizontal resolution and 60 vertical levels, ranging from 2 - 5 m at the surface to 60 - 70 m near the bottom. Details on the model configuration can be found in *Dugstad et al. (2019a)*. Thanks to its high spatial and temporal resolution, the model resolves mesoscale and some of the submesoscale processes in the Nordic Seas and captures the variability and dynamics of the area well (*Trodahl and Isachsen, 2018; Dugstad et al., 2019a*).

We use the Lagrangian data set obtained by *Dugstad et al. (2019a)*, who created this data set to investigate variability of the inflow to the Lofoten Basin. They used the 6 hourly output of the 3D velocity fields from the realistic model, spanning years 1996 to 1999, to advect numerical particles. These particles were deployed in a rectangular grid of 40 x 40 drifters (white dots Figure 3.2b) every week for three years at three different

depth levels (15 m, 200 m and 500 m). This spatially uniform deployment allows for a better representation of the flow, in contrast to the observed drifters and floats that are deployed along specific sections and in locations which can lead to limited and biased statistics (Davis, 1991). The particles were advected for 1 year using the OpenDrift tool (Dagestad *et al.*, 2018) with a 4th order Runge Kutta time stepping scheme. No explicit horizontal or vertical diffusion was added. Dugstad *et al.* (2019a) showed that turbulent transport processes are well captured by this data set.

Here, the data set is analyzed to study the pathways of AW along the mid-ocean ridge to the north. As we are only interested in the AW watermass, deployments northwest of the Mohn Ridge are not taken into account. Moreover, we only analyze those particle trajectories that leave the model domain toward the north or northwest. This way 143557 trajectories are selected. As the velocity in deeper layers is lower than at the surface and the advection time is only 1 year, this selection procedure favors particles deployed at shallow depths: 45% of the particles used for analysis are deployed at 15 m depth, 37% at 200 m depth and 18% at 500 m depth. The analyzed trajectories are therefore mostly representative of pathways of the upper part of the AW layer in the Lofoten Basin. The trajectories are further separated based on the location at which the particles leave the domain (thick colored lines along the northern and northwestern edge of the domain in Figure 3.2b). As will be elucidated in section 3.3 and Figure 3.5, the various transects defined in Figure 3.2b represent different regions of locally high concentrations of particles, indicative of mean circulation branches.

### 3.2.3. TRAJECTORIES FROM AN IDEALIZED NUMERICAL CONFIGURATION

As the realistic ocean model simulates only part of the eastern Nordic Seas, an idealized configuration of the Massachusetts Institute of Technology (MIT) general circulation model is used (Marshall *et al.*, 1997) to shed light on the connection between the eastern (Lofoten) and western (Greenland) basin. Furthermore, the importance of the frontal instability for AW watermass transformation is investigated using this model. Although idealized, the model captures the dynamics of the Nordic Seas pertinent for this study (see chapter 2). The model has a 5 km horizontal resolution and 33 vertical levels ranging from 20 m thickness at the surface to 200 m thickness near the bottom. The warm eastern basin is separated from a colder western basin by a mid-ocean ridge at 1200 m depth (Figure 3.3). Details on the model configuration can be found in Spall (2011) and in chapter 2; the hydrographic and dynamic properties of the circulation were described in detail in section 2.2.1.

The model domain consists of two parts that are separated by an island. The area north of the island represents the Lofoten and Greenland Basins. There, the ocean surface temperature is restored to an atmospheric temperature of 4°C with a timescale of 2 months to resemble a realistic surface heat flux (section 2.2.1). South of the island, restoring of temperature induces a buoyant cyclonic boundary current, representative of the AW inflow. This inflow separates into a slope current and a front current, mimicking the NwASC and NwAFC respectively (arrowheads in Figure 3.3a). As described in e.g. Spall (2010), the steepening of the continental slope near the Lofoten Islands is essential to create the observed enhanced eddy activity that induces the advection of AW throughout the eastern basins of the Nordic Seas. The idealized model captures the mag-

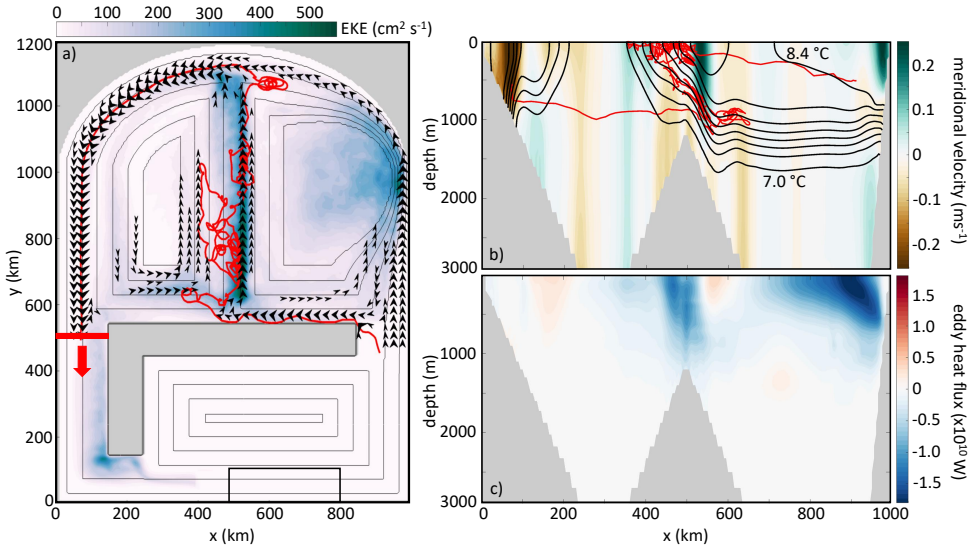


Figure 3.3: (a) 5-year mean surface eddy kinetic energy (shading) and surface velocity  $> 0.05 \text{ m s}^{-1}$  north of the sill (black arrowheads) in the idealized numerical simulation. Gray contours are the model bathymetry (contour interval is 500 m). The black box south of the sill indicates the region where the model temperature and velocity are restored. (b) Cross section at  $y = 750 \text{ km}$  of the 5-year mean meridional velocity (shading) and mean temperature (black contours, contour interval is  $0.2^\circ \text{C}$ ). The red lines in panels (a) and (b) show the trajectory of an example particle, released at  $y = 500 \text{ km}$  (red thick line) and traced backward in time. (c) Zonal eddy heat flux as a function of depth, integrated over the full meridional extent of the domain north of the sill.

nitude of EKE near the steep slope (shading in Figure 3.2a). Enhanced eddy variability is also found along the unstable front current. The total eddy heat flux across the thermal front in the idealized model is  $10 \times 10^{12} \text{ W}$  (Figure 3.2c), which is of similar magnitude as estimated from observations by *van Aken et al.* (1995) and *Walczowski* (2013). A discussion on the heat flux across the mid-ocean ridge in this idealized model is provided in appendix 3.A.

To investigate the watermass transformation of the Atlantic Water in this model, numerical particles are released at the outflow at  $y = 500 \text{ km}$  (red thick line in Figure 3.3a) and traced backward in time using the Connectivity Modeling System (CMS, *Paris et al.*, 2013). The particles are advected using a timestep of 1 hour within the daily averaged three-dimensional velocity fields of the MITgcm simulations. The new position of each particle is calculated using a 4th order Runge Kutta stepping scheme in time and a tricubic interpolation in space. Convection is represented by an increased vertical diffusion, and therefore, the model does not resolve explicitly vertical velocities associated with convection. To account for this process, the vertical movement of the numerical particles in the mixed layer is parameterized as described by *van Sebille et al.* (2013): every time the particle is diagnosed to be within the mixed layer, it is randomly moved within the layer with a maximum vertical velocity of  $0.1 \text{ m s}^{-1}$ .

Particles are released daily for 30 days with a particle resolution of 5 km in the zonal direction and 10m vertically. The resulting 35766 particles are advected for 4 years. Only particles that reach the gap between the island and the coast in the east within 4 years of backtracking (78% of originally seeded particles) are analyzed in this study. Once south of this gap, the particle has left the region of interest and the remainder of the pathway is not taken into account. An example trajectory is shown in Figures 3.3a-b. To test whether the results are sensitive to the time of the particle release, several simulations have been performed where the particle release date and frequency has been varied. These showed that the conclusions drawn in this chapter are consistent, regardless of the release date.

### 3.3. ALONG- AND ACROSS-FRONTAL PATHWAYS

In this section, the connection between the front current along the Mohn Ridge and the front current along the Knipovich Ridge is investigated using both the trajectories from surface drifters and ARGO floats (as described in section 3.2.1) and the trajectories from the realistic numerical simulation (as described in section 3.2.2). Furthermore, pathways that reveal cross-ridge exchange between the Lofoten Basin and the Greenland Basin are discussed.

The normalized particle density shown in Figure 3.4a highlights that the pathways taken by the surface drifters (i.e. that at some point entered the red shaded area in Figure 3.2a) lie close to the mid-ocean ridges. High particle density is found along the Mohn Ridge and the Knipovich Ridge. However, out of the 32 surface drifters that travel near the mid-ocean ridges, only 5 follow the path northward along both the Mohn Ridge and the Knipovich Ridge. All other trajectories display a path that alternates between the slope current and the front current as indicated by the gray arrows in Figure 3.4a. Most surface drifters that float along the Mohn Ridge (15 floats) are steered eastward by the 2500 m isobath at 72°N and continue their journey as part of the slope current. Most surface drifters that float along the Knipovich Ridge (12 floats) originate from the slope current. North of 74°N many drifter pathways display exchange between the western and eastern branch of the West Spitsbergen Current. Numerous surface drifter paths display loops, indicative of eddies.

This exchange between the slope current and the front current north of 72°N is also displayed by the trajectories of the ARGO floats (Figure 3.4b). In total, 17 floats flow along the Knipovich Ridge of which 15 originate from the slope current. The mean flow at 1000 m depth along the Mohn Ridge is southward (Voet *et al.*, 2010). So, most of the floats that follow the Mohn Ridge travel south (36 floats), and leave the Lofoten Basin along the Jan Mayen Ridge (25 floats). It is therefore not surprising that only 2 ARGO floats show a connection between the northward flow along the Mohn Ridge and the Knipovich Ridge.

As the number of surface drifters and ARGO floats that approach the mid-ocean ridges is limited, trajectories in the realistic model configuration (section 3.2.2) are used to investigate the connection between the slope and front currents in more detail. The locations where the numerical particles leave the model domain toward the north(west) show four distinct branches: one along the continental slope (67% of the total number of particles, Figure 3.5a), one along the eastern flank of the Knipovich Ridge (14% of the total number of particles, Figure 3.5b), one along the western flank of the Knipovich Ridge (17% of the total number of particles, Figure 3.5c) and one along the southern flank of

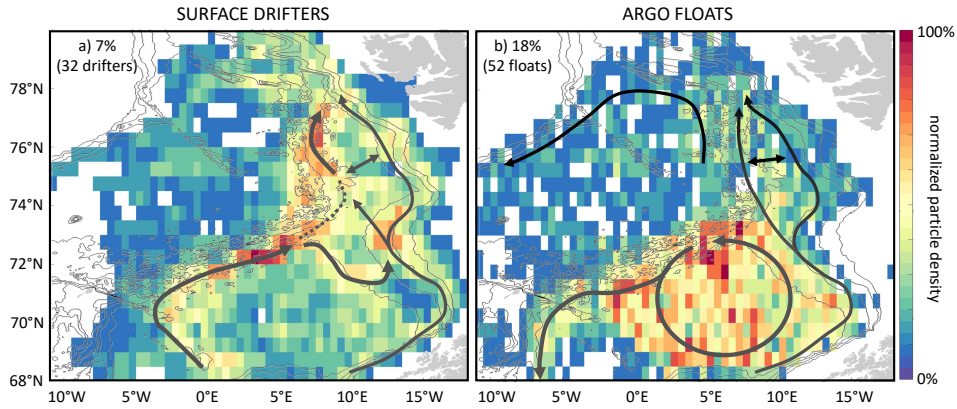


Figure 3.4: Normalized particle density map of all (a) surface drifters and (b) ARGO floats that flow along part of the Mohn and Knipovich Ridges (selection process described in section 3.2). Each float location is regridded on a  $0.5 \times 0.5^\circ$  lon x lat grid. Dark gray lines schematize the main pathways that the selected floats are prone to follow based on manual inspection of individual trajectories. The 1000 m, 1500 m, 2000 m and 2500 m isobaths are shown in gray. The percentage given in each panel indicates how many surface drifters or ARGO floats correspond to the subset shown in each panel with respect to their total number found in the Nordic Seas.

the Greenland Fracture Zone (GFZ, 2% of the total number of particles, Figure 3.5d).

The normalized particle density distribution in Figure 3.5 highlights which pathways the numerical particles take, depending on where they leave the domain. Just as observed in the trajectories of the surface drifters, some of the trajectories along the Mohn Ridge follow the 2500 m isobath at  $72^\circ\text{N}$  toward the east to join the slope current (see example trajectory in Figure 3.5a). Vice versa, some of the trajectories that follow the slope current flow along the same isobath toward the northwest to join the flow along the eastern flank of the Knipovich Ridge (see example trajectory in Figure 3.5b). Therefore, the trajectories in the realistic numerical simulation, in line with the observed trajectories (Figure 3.4), suggest substantial exchange between the front current and the slope current, before these branches continue north of  $72^\circ\text{N}$ .

In order to quantify how the flow along the Mohn Ridge and along the continental slope south of  $72^\circ\text{N}$  is redistributed over the various outflow branches to the north, different boxes are defined (see dashed white lines Figures 3.5a-c). When the particle originates from box I before leaving the model domain, it is defined as a slope current particle. If a particle originates from box II, it is defined as a front current particle. As a consequence, particles that never enter one of the boxes are not taken into account in the analysis, as their trajectories are not long enough to determine whether they originated from the slope current or from the front current. Recall that the particles categorized in Figure 3.5c leave the model domain along the western flank of the Knipovich Ridge and, when not changing the size of box II, would all be incorrectly defined as front current particles. Therefore, a slightly smaller box is used here.

Using this method, we estimate that  $\sim 92\%$  of the particles that flow within the slope current also leave the domain within the slope current, and  $\sim 8\%$  joins the front cur-

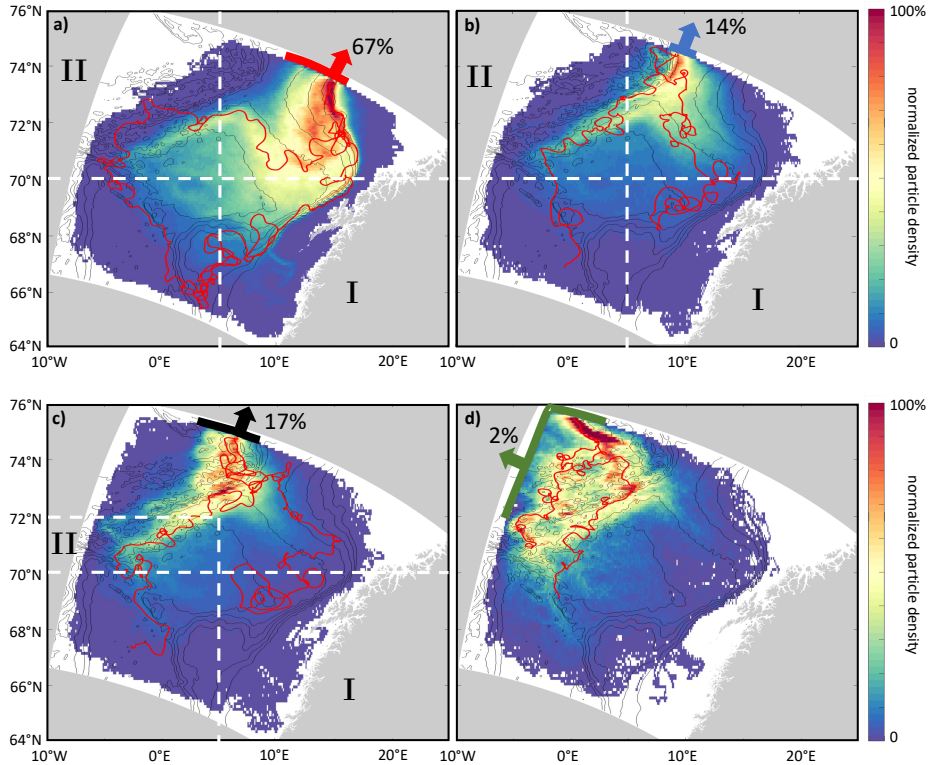


Figure 3.5: Normalized particle density map of particles deployed at all three depth levels (15 m, 200 m and 500 m) and leaving the model domain (a) along the continental slope, (b) along the eastern flank of the Knipovich Ridge, (c) along the western flank of the Knipovich Ridge and (d) along the Greenland Fracture Zone. Each particle position is regridded on a  $0.1^\circ \times 0.1^\circ$  lon x lat grid. Example trajectories of each pathway are indicated by the red lines. Black contours show isobaths with 500 m contour intervals; dashed white lines show the boxes used to investigate whether particles followed the inner or outer branch of the NwAC as described in section 3.3. Results shown are diagnosed from the realistic numerical simulation (section 3.2.2).

rent along the Knipovich Ridge. From the flow along the Mohn Ridge, ~35% joins the slope current, ~27% flows along the eastern flank of the Knipovich Ridge and ~38% flows along the western flank of the Knipovich Ridge. Care should be taken when interpreting these numbers; the available particles trajectories do not capture the entire Atlantic Water layer in the eastern basin, as their original deployment is only at 3 depth levels (section 3.2.2). Also, particles represent different volume transports. The percentages calculated are based on the total number of particles following each branch, not on the total transport carried. Last, the percentages presented depend on the definition of the boxes used for separation. Therefore, the results should be interpreted as an indication, not an exact quantification, of the significant exchange between the slope current and the front current that takes place near 72°N. The results clearly reveal that the flow along the Mohn Ridge does not form a one-to-one connection with the flow along the Knipovich Ridge.

An interesting aspect of the pathway highlighted by the particle density distribution in Figure 3.5c is that it shifts from the eastern flank of the Mohn Ridge to the western flank of the Knipovich Ridge. Furthermore, ~2% of the total outflow in the realistic numerical simulation consists of particles that cross the mid-ocean ridge from the Lofoten Basin into the Greenland Basin (Figure 3.5d). The individual trajectories show strong variability along and northwest of the Mohn Ridge (yellow area Figure 3.5d), but further north they merge into a clear pathway along the Greenland Fracture Zone. As they originate from the AW layer in the east, they could represent AW watermasses that detach from the front current due to frontal instabilities and travel into the Greenland Basin as observed by *Budéus and Ronski (2009)*.

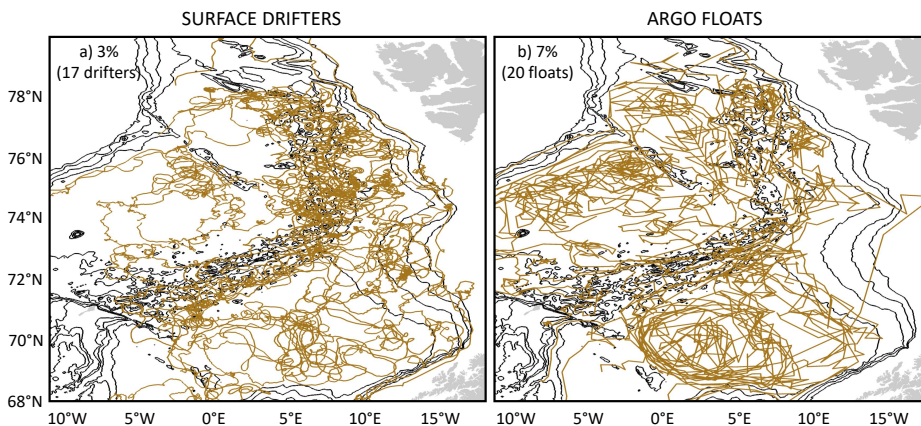


Figure 3.6: Pathways of (a) drifters and (b) ARGO floats that cross the Mohn and Knipovich Ridges. The 1000 m, 1500 m, 2000 m and 2500 m isobaths are shown in black. The percentage given in each panel indicates how many drifters or floats correspond to the subset shown with respect to the total number of surface drifters and ARGO floats found in the Nordic Seas (section 3.2.1).

The observed trajectories of surface drifters reveal the instability of the front current as well (Figure 3.6a). Especially along the Knipovich Ridge, multiple surface drifters cross the summit of the ridge and show meandering or circular (eddy) trajectories near

the ridge. The trajectories of the 17 surface drifters shown in Figure 3.6a all indicate significant cross-ridge exchange between the Lofoten and the Greenland Basins.

Furthermore, 20 ARGO floats are found to cross the mid-ocean ridge from the Greenland Basin into the Lofoten Basin (or vice versa, Figure 3.6b). However, the cross-ridge exchange at the ARGO float depth is not necessarily related to the frontal instability. A zoom-in of four ARGO float trajectories near the ridge is shown in Figure 3.7. Three of these floats start in the cyclonic gyre of the Greenland Basin (Figure 3.7a-c). When they approach a gap in the ridge, they cross, travel southward and start to follow a cyclonic circulation along the outer rim of the Lofoten Basin. The example trajectory in Figure 3.7d shows similar behavior, except that the float continues its path northward along the Knipovich Ridge. The exchange between west and east through gaps in the topographic ridges has been hypothesized by e.g. *Spall* (2010), and is confirmed by these trajectories. Although *Olsson et al.* (2005) and *Messias et al.* (2008) showed that a fast pathway to exit the Greenland Basin exists via the Jan Mayen Current, the ARGO floats that originate from the Greenland Basin do not seem to have a preferred location where they cross the mid-ocean ridge, except for the local topography. Not surprising, they seem to be steered much stronger by topography than the surface drifters that showed cross-ridge exchange. Possibly, enhanced mean flow within canyons as discussed by *Ruan and Callies* (2019) can lead to the behavior seen by the ARGO floats.

In conclusion, results from surface drifter trajectories (Figure 3.4a), ARGO float trajectories (Figure 3.4b) and trajectories in a realistic numerical configuration (Figure 3.5) all indicate that the connection between the flow along the Mohn Ridge and the flow along the Knipovich Ridge is not as strong as suggested by surface circulation schematics currently in use (e.g. *Dugstad et al.*, 2019b; *Shao et al.*, 2019; *Broomé et al.*, 2019). Furthermore, several surface drifters and ARGO floats cross the mid-ocean ridge from one basin into the other. Therefore, in addition to the large eddy variability in the Lofoten Basin (*Bosse et al.*, 2018), the enhanced exchange between the slope current and the front current north of 72°N and the excursions of watermasses across the mid-ocean ridge lengthen the residence time of the AW watermass within the eastern basin of the Nordic Seas. This potentially has implications for the watermass transformation of the AW in the eastern basin, which is discussed in the following section.

### 3.4. IMPORTANCE OF FRONTAL INSTABILITY FOR WATERMASS TRANSFORMATION

Next, we investigate the dependence of AW watermass transformation on possible pathways in more detail. The realistic numerical configuration is limited by its domain, and the low number of ARGO floats and surface drifters available near the front current is not sufficient to perform any statistical analysis on watermass transformation. Furthermore, since the surface drifters and ARGO floats drift at a specified pressure level, they are not suited to trace a particular watermass that might move in the vertical. Therefore, the fate of the AW watermass is traced in the idealized model configuration of the Lofoten and Greenland Basin introduced in section 3.2.3. Different pathways are distinguished and the transformation along each pathway and the transit time of the AW watermass from in- to outflow are analyzed.

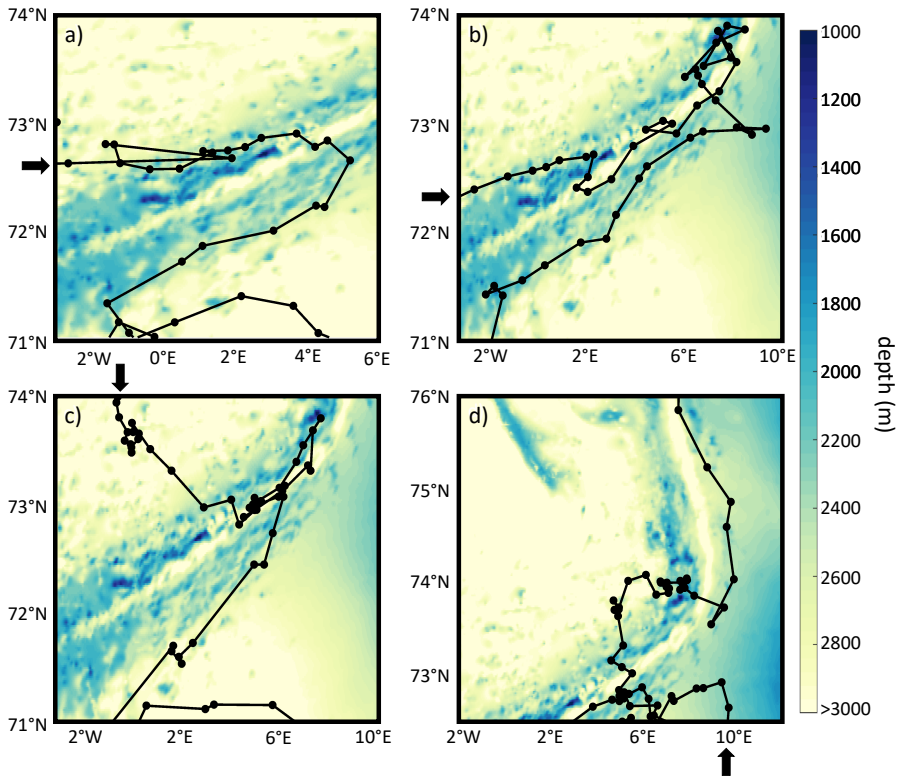


Figure 3.7: ARGO float trajectories that cross (a-c) the Mohn Ridge and (d) the Knipovich Ridge (black lines). The arrows indicate the travel direction of the floats and shading shows the bathymetry.

To separate particles that follow only the slope current from the particles that follow only the front current and to separate pathways that display exchanges with the interior of the eastern basin or the western basin, three boxes are defined (see white dashed lines in Figure 3.8a-d). The *only\_bc*-particles enter only box A. They mainly follow the slope current and represent the core of the NwASC. Most stay within this boundary current, but some show exchange with the interior of the eastern basin (see light blue shading in box A in Figure 3.8a). The *only\_front*-particles enter only box B. Their path reveals the meandering structure of the front current (Figure 3.8b) and represents the core of the NwAFC. They reach the front by turning directly toward the west upon entering the basin and leave the front toward the western basin by following a deeper isobath than the *only\_bc*-particles. The *front\_east*-particles enter both box A and box B (but not box C). They travel along part of the front and/or slope current, but also show clear excursions into the interior of the eastern basin while being steered by eddies. Exchange between the front current and the slope current occurs regularly (see example trajectory in Fig-

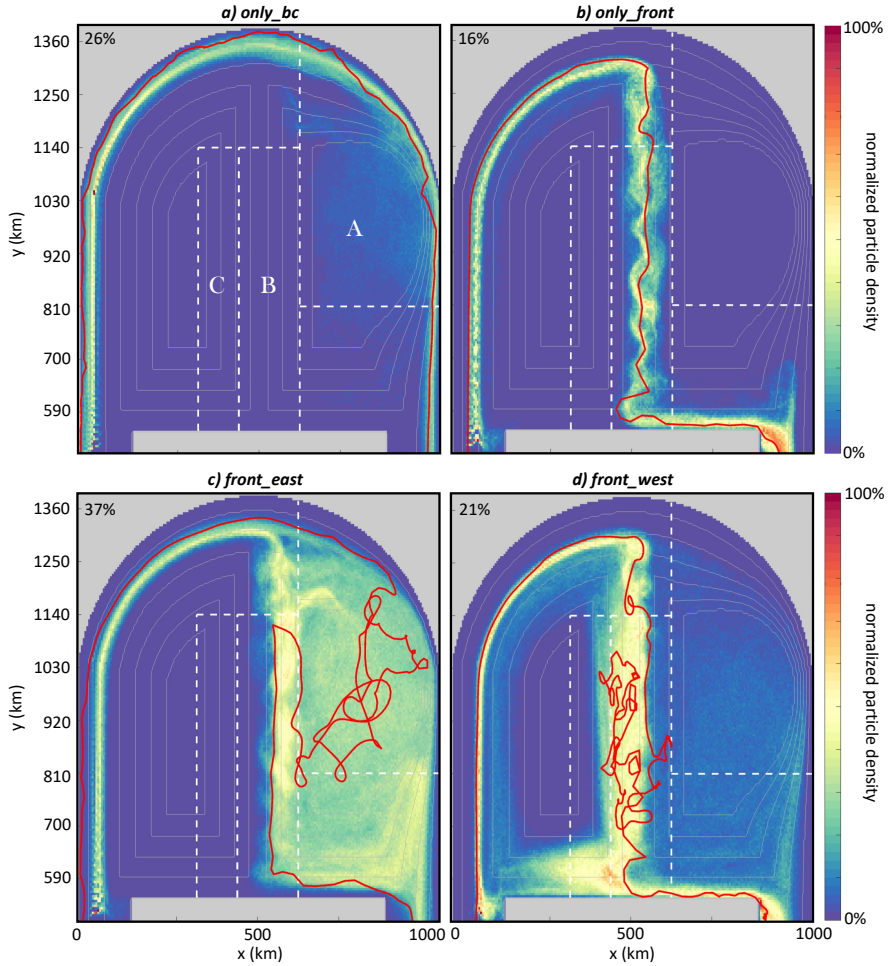


Figure 3.8: Normalized particle density map of the (a) *only\_bc*-pathway, (b) *only\_front*-pathway, (c) *front\_east*-pathway and the (d) *front\_west*-pathway. Each particle position is regridded on a 11x11 km x-y grid. Example trajectories of each pathway are indicated by the red lines. Gray lines show isobaths; dashed white lines indicate the areas used to separate the particle pathways as described in section 3.4. Results shown are diagnosed from the idealized numerical simulation (section 3.2.3).

ure 3.8c). The *front\_west*-particles form the last category that enter at least box C and thus cross the mid-ocean ridge toward the western basin. These particles capture the instability of the front current and some of those particles spend part of their journey in the closed cyclonic circulation of the western basin (see also appendix 3.A for a more detailed discussion on the *front\_west*-pathway).

As set by the configuration of the idealized numerical simulation, watermass transformation north of the island can only occur by direct cooling to the atmosphere or by resolved or numerical mixing with neighboring watermasses. To assess the watermass transformation in the basin, the temperature of the watermass the particles represent at the inflow (crossing  $y = 500$  km east of the island to the south for the first time, Figure 3.3a) is compared to the temperature at the outflow (crossing  $y = 500$  km west of the island, the particle release location) for each pathway. It appears that on average, the AW watermass is cooled by  $\sim 1.3^\circ\text{C}$ . However, the temperature change of the AW watermass depends on its pathway through the basin (Figure 3.9a).

The AW pathways appear to some extent already set by the temperature distribution at the inflow. The warmest part of the inflow is most likely to follow the *only\_bc*-pathway (solid green line in Figure 3.9a), whereas the coldest part of the inflow is most likely to take the frontal pathway (orange and purple solid lines). This is in line with observed characteristics of the NwASC and the NwAFC, where the frontal branch is colder and fresher than the slope current (e.g. Hansen and Østerhus, 2000). In addition, at the inflow the *front\_east*-particles also represent a slightly colder watermass than the *only\_bc*-particles. As the *front\_east*-particles are colder, their trajectory (when temporarily following the slope current) is slightly offshore of the trajectories of the *only\_bc*-particles. They are therefore more sensitive to the instability of the slope current, which explains their excursions through the interior of the eastern basin (Georgiou et al., 2020).

The distribution of the particles' temperature at the outflow shows two distinct peaks at  $\sim 8.2^\circ\text{C}$  and  $\sim 7.9^\circ\text{C}$  (dashed lines Figure 3.9a). The colder signal at the outflow is related to the pathways that interact with the western basin interior (the *front\_west*-particles, purple line in Figure 3.9a), whereas the warmer outflow waters correspond to the pathways that stay in the front and/or slope current or travel through the interior of the eastern basin (orange, green and gray lines). As different pathways reveal a different temperature signal at the outflow, the watermass transformation of the AW watermass depends on the pathway the water takes through the basin. In particular, the temperature distribution of the *only\_front*-particles and *front\_west*-particles is similar at the inflow (solid orange and purple lines in Figure 3.9a), while a strong temperature difference arises at the outflow. This indicates that the excursion into the western basin is essential to yield a stronger transformation.

Although very idealized, the pathways along the front current (the *only\_front*-particles) and across the mid-ocean ridge (the *front\_west*-particles) show resemblance to the pathways along the eastern and western flank of the Knipovich Ridge found in the realistic numerical simulation (Figure 3.5b-c). Also in the realistic simulations, the temperature and salinity distribution of the particles that end up along the Knipovich Ridge is similar at their start, while at their end there is a clear difference (Figure 3.10): particles that cross the Mohn Ridge toward the west are colder and fresher when they leave the model domain than particles that flow along the eastern side of the Knipovich Ridge.

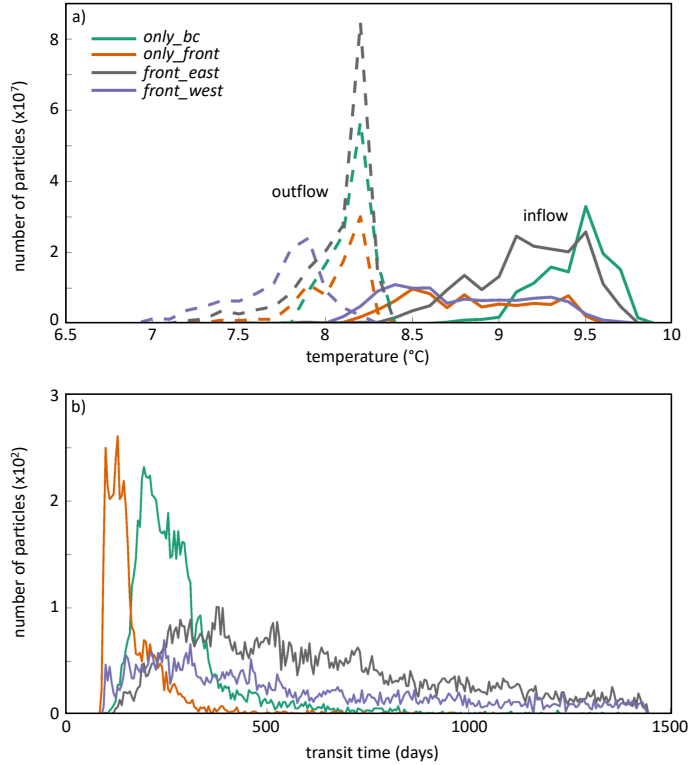


Figure 3.9: (a) Temperature distribution of each pathway at the inflow (solid lines) and outflow (dashed lines). The temperature binsize is 0.1°C. (b) Distribution of the transit time from inflow to outflow for each particle, separated per pathway. A binsize of 5 days is used. Results shown are diagnosed from the idealized numerical simulation (section 3.2.3).

The difference in watermass transformation along each pathway is also reflected by the transit time from inflow to outflow in the idealized numerical simulation (Figure 3.9b). Not surprising, the instability of the slope current increases the residence time of the AW watermass within the domain (compare green line to gray line in Figure 3.9b). The long residence time in the Lofoten Basin due to the large eddy variability is crucial for the strong heat loss across the basin (e.g. *Bosse et al.*, 2018). However, the instability of the front current also increases the residence time due to the exchange with the western (Greenland) basin (compare orange line to purple line in Figure 3.9b).

Interestingly, the frontal pathway is faster than the pathway following the slope current (green and orange line in Figure 3.9b). This can be explained by the lower velocity of the slope current downstream of the region of enhanced eddy shedding in our idealized numerical simulation (see arrowheads Figure 3.3a). Due to the idealized nature of the model simulations, it is not possible to draw any further conclusions regarding

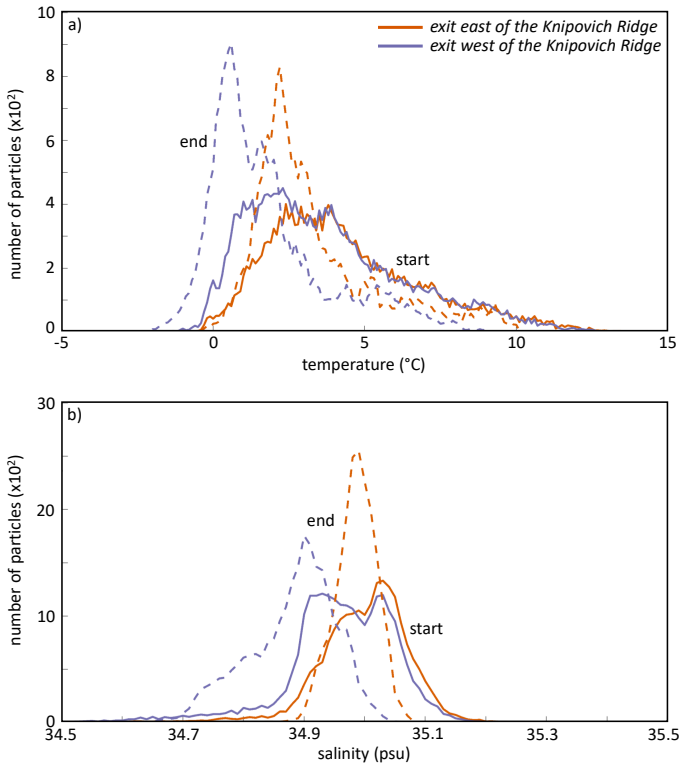


Figure 3.10: (a) Temperature and (b) salinity distribution of particles that leave the domain along the eastern flank (orange line) and along the western flank (purple line) of the Knipovich Ridge at deployment (solid lines) and when leaving the domain (dashed lines). A binsize of 0.1°C and 0.01 psu for temperature respectively salinity are used. Results shown are diagnosed from the realistic numerical simulation (section 3.2.2).

the relative transit times of the two NwAC branches. Based on the realistic travel distance, the frontal pathway is longer. However, recent estimates of the front current near the Mohn Ridge indicate that the front current is at least as strong as the slope current (*Bosse and Fer, 2019*). Regardless of the relative transit times, the larger heat loss of the slope current than the front current in our idealized simulation emphasizes that not only the atmospheric forcing, but also the transit time and pathways play an important role for the AW watermass transformation.

### 3.5. CONCLUSIONS AND DISCUSSION

In this chapter, we have investigated whether the flow along the Mohn Ridge and the flow along the Knipovich Ridge are connected in a Lagrangian sense. As the number of surface drifters and ARGO floats near the mid-ocean ridges is limited, we have additionally

analyzed trajectories of numerical particles in a realistic and an idealized numerical simulation. These simulations allowed us not only to investigate the connection between the front current and the slope current of the Norwegian Atlantic Current (NwAFC and NwASC respectively), but also to trace watermass transformation along different pathways.

Based on this study, it is clear that care should be taken when using velocity and travel direction from surface drifters to derive circulation maps. These maps, as for example derived by *Orvik and Niiler (2002)*, show the Eulerian mean velocity field, but cannot provide any information on the connection between different branches in a Lagrangian sense. Based on the observed trajectories, we found only a weak connection between the northward flow along the Mohn Ridge and along the Knipovich Ridge, unlike how the NwAFC is normally schematized (i.e. *Dugstad et al., 2019b; Shao et al., 2019; Broomé et al., 2019*). Only 5 of the 32 surface drifters showed the traditional pathway north along both ridges. Instead, most drifters displayed exchange with the slope current (Figure 3.4a).

Trajectories in the realistic numerical simulations indicated a stronger connection between the flow along the Mohn Ridge and the Knipovich Ridge than the observed trajectories. However, the model results showed a clear branching of the flow along the Mohn Ridge into different paths to the north (Figure 3.5). Therefore, in the realistic numerical simulation, the front current along the Mohn Ridge did not form a one-to-one connection with the front current along the Knipovich Ridge either, corroborating the conclusions drawn from the observed trajectories.

Multiple exchanges between the front current and the slope current were seen in both the observed trajectories as in the trajectories of the realistic and the idealized numerical simulation (Figures 3.2a, 3.5 and 3.8c). Many surface drifters and ARGO floats traveled along the 2500 m isobath near 72°N toward the east (west) to join the slope (front) current on their path northward. This path was present in the realistic numerical simulation as well. Further north, multiple floats crossed from the eastern branch of the West Spitsbergen Current to the western branch of the West Spitsbergen Current (or vice versa). The front current and slope current are therefore not isolated, but clearly connected in a Lagrangian sense. *Rosby et al. (2009a)* observed a similar connection between the front current and the slope current just north of the Iceland-Scotland Ridge using RAFOS floats. Our results suggest that also north of 72°N significant exchange between the two branches occurs.

In the Nordic Seas, mean circulation patterns are known to be strongly dominated by topography (e.g. *Nøst and Isachsen, 2003; Voet et al., 2010*). *Voet et al. (2010)* observed the tight flow alignment with topography using so-called topotrophy derived from ARGO float trajectories, which is a measure for flow alignment with isobaths. However, the region north of the Lofoten Basin is characterized by low values of topotrophy (his Figure 9), indicating that the ARGO float trajectories cross isobaths there. This is in agreement with our findings, where in addition to the ARGO floats also surface drifters showed similar behavior in this area. Such a crossover region could indicate that in this area the strength of eddies and meanders is of similar magnitude as along-flow mean velocities (*Bower, 1991; Rosby et al., 2009a*).

The numerous exchanges between the front current and the slope current lengthen

the residence time of AW within the eastern basins of the Nordic Seas, which may enhance the total heat loss over the basin. Furthermore, the link between these two branches weakens the direct propagation of AW anomalies from the Greenland-Scotland Ridge to Fram Strait. It is therefore important to not only increase our knowledge on processes within the Lofoten Basin, but also on the region north of 74°N and in particular on the local front current dynamics.

Analyses of trajectories in both the realistic and the idealized numerical configurations showed that AW watermass transformation in the Nordic Seas depends on the path that the AW takes. Additionally, the watermass transformation itself could to some extent determine which path the AW will follow downstream. Our results suggest that coldest and freshest watermasses are formed along the front current, due to the frontal current instability and exchange with the western basin. Although not investigated in this study, it could be that some of the observed pathways have a seasonal dependency. On longer timescales, it is known that the strength of the front current depends on the phase of the North Atlantic Oscillation (NAO), where the front is weaker during the negative phase of the NAO (*Raj et al.*, 2019). Also under future scenarios the front is expected to weaken, due to a reduction in the density gradient between the Lofoten Basin and the Greenland Basin (chapter 2). If, as a result, the exchange between the east and west reduces, the AW heat loss in the eastern basins could decrease and convection in the Greenland Basin could weaken due to a smaller supply of salty waters from the east.

Although not observed previously (*Poulain et al.*, 1996; *Rosby et al.*, 2009a; *Latarjius and Quadfasel*, 2016), we found 37 ARGO floats and surface drifters that crossed the mid-ocean ridges. This might seem like a small number, but compared to the total number of observed trajectories that reached the mid-ocean ridges (84 floats), the observed cross-ridge exchange may be substantial. As in-situ measurements suggest strong northward flow along the mid-ocean ridge (*Bosse and Fer*, 2019), it is surprising that out of the 564 surface drifters and 283 ARGO floats in the Nordic Seas, so few are found close to the Mohn and Knipovich Ridges. We would therefore encourage deployment of drifters within the strong northward flow along the mid-ocean ridge, to gain further insight in the pathways and residence time of AW in the eastern Nordic Seas.

# Appendix

## 3.A. HEAT EXCHANGE ACROSS THE MID-OCEAN RIDGE

Chapter 3 discussed the various pathways along the front and the watermass transformation along each path, with the main aim to investigate the connectivity of the front current along the Mohn and Knipovich Ridges. The observations and the numerical simulations indicated that the instability of the front current plays an important role for the watermass transformation of Atlantic Water via exchange across the mid-ocean ridges. Also in appendix 2.A the importance of this watermass exchange across the ridge was pointed out, as it impacts the stratification in the eastern basin. Therefore, this appendix provides further insight on the heat exchange across the mid-ocean ridge by connecting a Lagrangian and an Eulerian framework using the idealized model simulations (section 3.2.3).

### METHOD

For the analysis, the reference simulation described in section 2.2.1 and section 3.2.3 is used. To investigate the watermass exchange across the mid-ocean ridge in the Eulerian framework, the transport across the ridge is quantified as a function of temperature using the LAYERS package (Abernathey *et al.*, 2013) of the MITgcm. The temperature layers range from 6°C (the lowest temperature in the simulation) to 10°C (the highest temperature in the restoring region) with a layer increment of 0.2°C. At each model time step, the zonal and meridional velocities ( $u_T$  and  $v_T$ ), the layer thickness ( $h_T$ ) and the product of these ( $u_T h_T$ ) are diagnosed for each temperature layer. Then, the net zonal transport  $\Psi_{net}$  across a meridional transect as a function of temperature is given by

$$\overline{\Psi_{net}}(x, T) = \overline{u_T h_T} dy, \quad (3.1)$$

where  $dy$  is 5 km and the overbar indicates a time mean of 5 years. The net transport can be separated into a mean and an eddy component using:

$$\overline{\Psi_{mean}}(x, T) = \overline{\overline{u_T} \overline{h_T}} dy \quad (3.2)$$

and

$$\overline{\Psi_{eddy}}(x, T) = \overline{u'_T h'_T} dy = \overline{\Psi_{net}} - \overline{\Psi_{mean}}. \quad (3.3)$$

The connection between the different watermasses that cross the mid-ocean ridge as a result of lateral eddy fluxes are further investigated using a Lagrangian framework. Particles are released at the location of the mid-ocean ridge ( $x = 500$  km) where the mean flow across the ridge is minimal ( $y = 645$ - $1285$  km, thus excluding the zonal boundary currents) and are advected forward in time. The particles are released daily for 30 days with a particle resolution of 5 km in the meridional direction and 10m vertically. The resulting 460530 particles are advected for 4 years. Only particles that leave the marginal sea by crossing the sill towards the south are used for analysis ( $\sim 65\%$  of the originally seeded particles).

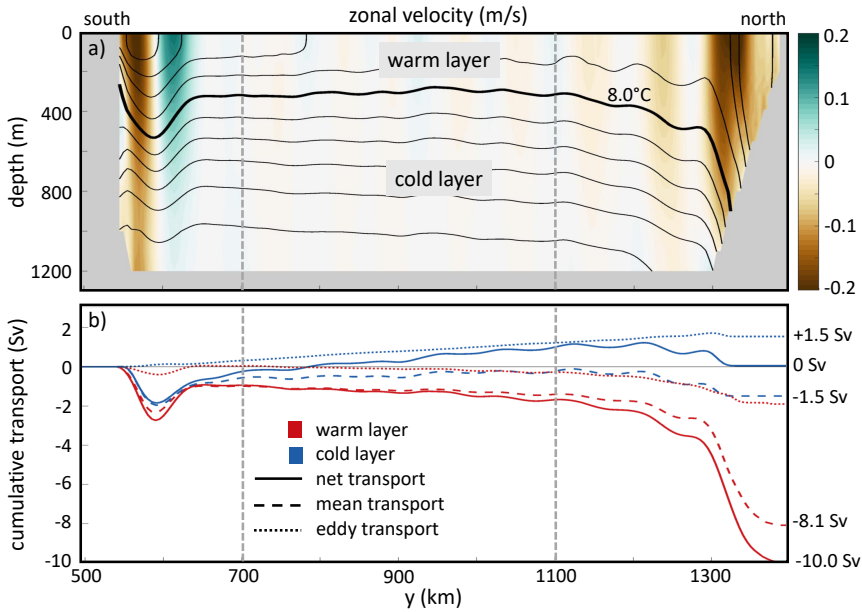


Figure 3.11: (a) 5-year mean zonal velocity at the mid-ocean ridge ( $x = 500$  km) as a function of depth. Solid contours show the mean isotherms with contour interval  $0.2^\circ\text{C}$ . The black dashed lines separate the boundaries of the mid-ocean ridge from the interior part. (b) Cumulative net (solid), mean (dashed) and eddy (dotted) transport with respect to the south for the warm layer ( $T > 8^\circ\text{C}$ , in red) and the cold layer ( $T < 8^\circ\text{C}$ , in blue). A positive slope of the curve indicates transport to the east, a negative slope indicates transport to the west. The total transport across the ridge is provided at the right side of the panel for each component.

## RESULTS

The mean volume transport across the mid-ocean ridge is confined to the northern boundary of the idealized model domain (Figure 3.11a), where the slope current flows into the western basin (Figure 3.3a). At the southern boundary of the ridge (just north of the island), a strong westward mean current (brown shading in Figure 3.11a) is partly compensated by an eastward current slightly farther north (green shading in Figure 3.11a at  $y = 550\text{--}560\text{ km}$ ). These currents are part of the front current, that slightly overshoots the ridge, before traveling north along the eastern slope of the mid-ocean ridge (see arrows in Figure 3.3a). Between the strong mean flow in the north and the south (dotted lines in Figure 3.11) the mean transport across the ridge is close to zero.

Based on Figure 3.9a (compare the *front\_west*-pathway and the *front\_west*-pathway), a temperature threshold of  $8^\circ\text{C}$  is used to separate cold from warm watermasses crossing the mid-ocean ridges. At the southern boundary (south of  $y = 650$  km), there is a net transport of  $\sim 0.75$  Sv of both watermasses to the west (solid lines in Figure 3.11b), primarily transported by the mean flow (dashed lines in Figure 3.11b). Across the section where the mean flow is negligible (between the vertical dashed lines of Figure 3.11), the net transport across the ridge is clearly eddy driven (compare the dotted and solid lines in Figure 3.11b): the warm watermass is transported to the west and the cold watermass

is transported to the east. At the northern boundary, both watermasses are transported to the west by the mean flow and the eddy transport in this region is negligible.

A significant fraction of the heat flux across the mid-ocean ridge is driven by eddies. *Isachsen and Nøst* (2012) already showed that such a cross-frontal flux needs to exist in order to close the buoyancy budget of the Nordic Seas. They suggested the existence of an eddy-induced overturning across the ridge, where the warm and salty water from the east is transported across the front and transformed to dense water by air-sea heat fluxes in the west. This dense water then subducts below the front and is transported back east across the ridge below the thermocline. They hypothesized that in order to close this loop, the dense waters need to be transformed to lighter waters in the eastern basin. Such a diapycnal upwelling in the eastern basin would imply a non-zero net transport of the cold watermass across the ridge, which is not seen in our numerical simulation (solid blue line Figure 3.11b). Instead, this cold (dense) watermass leaves the eastern basin within the mean flow near the boundaries of the basin (dashed blue line). As the numerical simulation is idealized, it might not capture processes that potentially drive diapycnal upwelling. However, a mean flow at depth is difficult to observe and therefore, dense water transport by the mean flow might not be captured using available observations for the buoyancy budget presented by *Isachsen and Nøst* (2012).

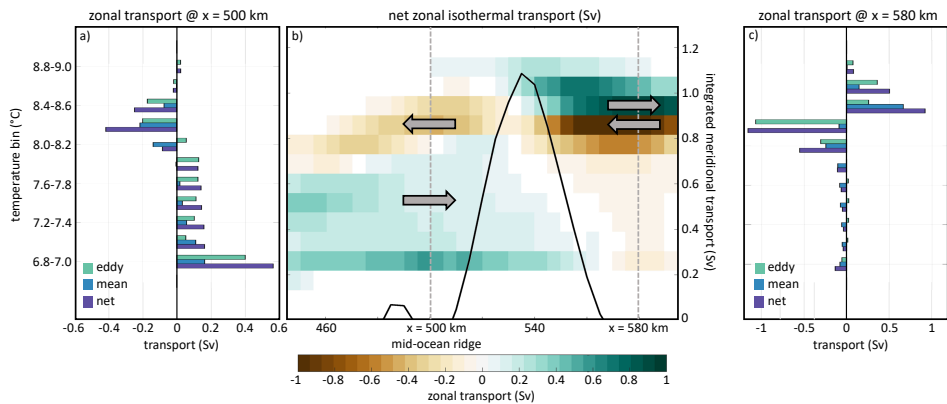


Figure 3.12: (a) Zonal transport between  $y = 700$ -1100 km across  $x = 500$  km as a function of temperature. (b) Zonal transport near the mid-ocean ridge as a function of temperature; green colors indicate eastward flow, brown colors indicate westward flow. The black curve (y-axis on the right hand side) gives the integrated meridional transport to highlight the position of the front current at this transect. Note that the mid-ocean ridge is located to the west of this black curve, at  $x = 500$  km. (c) Zonal transport between  $y=700$ -1100 km across  $x = 580$  km as a function of temperature. The net zonal transport (purple) in (a) and (c) is decomposed in a mean (blue) and eddy (green) component. Note that most of the isotherms outcrop in westward direction and are very steep near the region of the mid-ocean ridge (see Figure 3.3b). Therefore, the temperature layers west of the front current in panel a and b are located higher in the water column than the same temperature layers east of the front current in panel b and c.

The importance of eddies for the heat transport across the mid-ocean ridge is nicely visualized in Figure 3.12 as well, which shows that two regimes can be distinguished. West of the front current (black curve), water with a temperature of  $8.8$ - $8.4$ °C is advected into the western basin (brown shading). A cold watermass ( $<8$ °C) returns towards the

front current. East of the front current, water with a temperature  $>8.4^{\circ}\text{C}$  is transported into the eastern basin, and a watermass with intermediate temperatures ( $8-8.4^{\circ}\text{C}$ ) returns. These patterns are typical for a baroclinic unstable front where eddies tend to flatten isopycnals (e.g. *Olbers et al., 2012*). In contrast to a baroclinically unstable slope current, heat can be transported laterally in both directions along the front as the flow is not bounded by a continental slope.

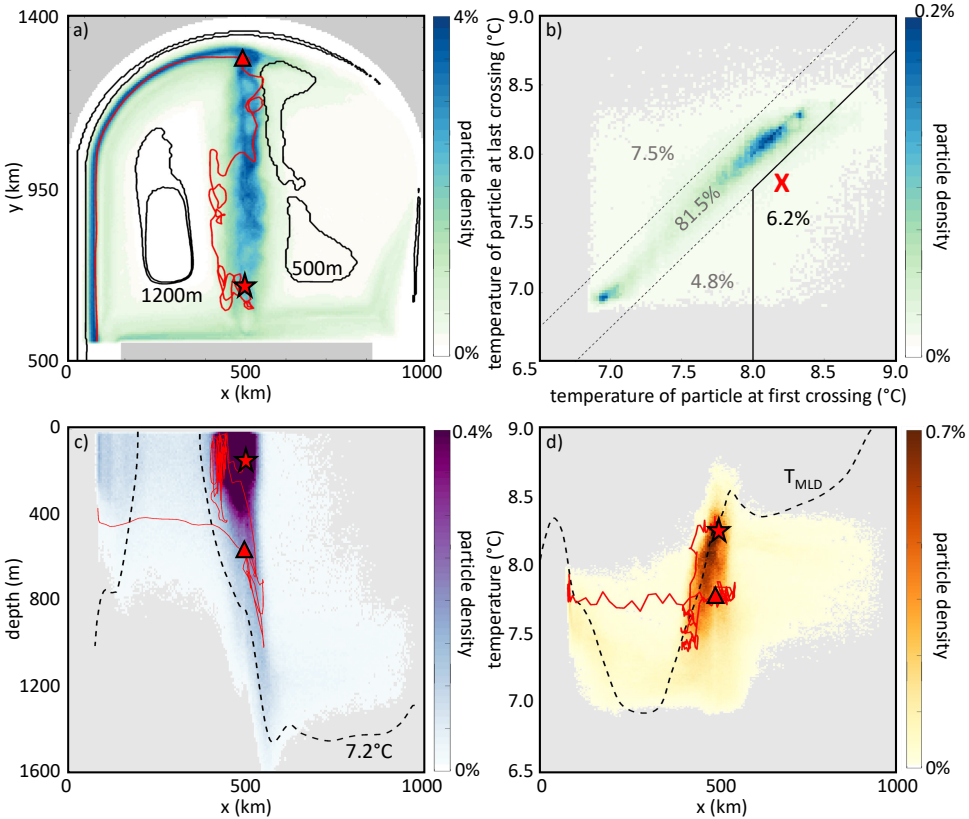


Figure 3.13: (a) Density of the particle position of particles released at  $x = 500$  km and  $y = 645-1285$  km. In red an example trajectory is shown. The 500 m and 1200 m 5-year mean mixed layer depth contour is shown in black. (b) Density distribution of the particle temperature at the start (star in (a), horizontal axis) compared to the particle temperature when it crosses the mid-ocean ridge for the last time (triangle in (a), vertical axis). The red cross indicates the temperature change along the example pathway shown in (a). The solid black lines indicate the selected particles that start in the warm layer ( $> 8^{\circ}\text{C}$ ) and experience a net cooling  $> 0.25^{\circ}\text{C}$ . (c-d) The density of the particle's (c) depth and (d) temperature as a function of their zonal excursions for the selected particles in panel (b). The depth and temperature along the example pathway are shown in red. The dashed black line in (c) indicates the depth of the mean  $7.2^{\circ}\text{C}$  isotherm and; (d) it denotes the temperature of the mean mixed layer depth.

When the net zonal transport is separated in a mean and an eddy component using equations 3.2 and 3.3, it indeed appears that this zonal transport is primarily driven by eddies, especially for the transport towards the front (green bars in Figures 3.12a and 3.12c).

Although the front current is unstable and as such enables a heat flux from the front region toward the east and the west, the front itself, not the mid-ocean ridge, seems to limit the exchange between the eastern and western basins; the net transport of the cold watermass (green shading west of the front in Figure 3.12b) crosses the mid-ocean ridge (at  $x = 500$  km), but does not seem to cross the front into the eastern basin. As volume is conserved, this watermass has to change direction to flow along the front instead of across. To illustrate the circulation and variability along the front in all dimensions, virtual particles are released at the mid-ocean ridge as described in the method section of this appendix. As the eddy transport across the ridge is only  $\sim 1.5$  Sv (Figure 3.11b), most particles released over the full depth of the mid-ocean ridge flow along the meandering front current to the north, where they follow the western boundary current out of the basin ( $>80\%$ , Figure 3.13a). This pathway is similar to the *front\_only*-pathway presented in section 3.4.

A subset of this particle data set is analyzed in more detail to visualize the connection between the warm watermass transport toward the west and the cold watermass toward the east (respectively brown and green shading west of the front in Figure 3.12b). This subset consists of particles that represent a warm watermass ( $> 8^\circ\text{C}$ ) that cools by more than  $0.25^\circ\text{C}$  before leaving the mid-ocean ridge. This selection is visualized in Figure 3.13b) and represent trajectories similar to the *front\_west*-pathway discussed in section 3.4.

First, a single example particle pathway is analyzed (see red trajectory in Figure 3.13a). The red cross in Figure 3.13b shows its temperature change along the trajectory (from the star to the triangle in Figure 3.13a), which changes from the warm layer watermass to the cold layer watermass. After its release, this particle travels to the west in an eddy-ing motion. There, strong vertical movement of the particle is seen (Figure 3.13c). This indicates that the particle is located in the mixed layer. The temperature of the particle drops (red line in Figure 3.13d) until it reaches the temperature of the mixed layer (dotted line). Once below the mixed layer, the particle moves along isotherms and slight displacements in an east- or westward direction are accompanied by a large displacement in depth in order to follow the steeply sloping isotherms (see Figure 3.13c and isotherms in Figure 3.3b). After it leaves the mid-ocean ridge via the western boundary current (triangle in Figure 3.13), both the temperature and depth of the particle remain constant.

All other particles of the subset show similar behavior (see shading in Figures 3.13c-d). Although the particles enter the mixed layer at different locations along the mid-ocean ridge, the largest (and fastest) changes in temperature are seen just west of the mid-ocean ridge while the particles are in the mixed layer. This becomes clear when comparing the temperature of the particles with the mean temperature of the mixed layer (dotted line in Figure 3.13d). The largest fraction of particles is found exactly where the mixed layer temperature decreases rapidly in the westward direction, indicating that the change in temperature is due to atmospheric cooling. Further, in Figure 3.13c a band of increased particle density is seen at the mid-ocean ridge ( $x = 500$  km) in a slightly

tilted direction until a depth of 1600m. This indicates that the particles undergo large variations in depth below the mixed layer when they are steered slightly to the east or the west.

## CONCLUSIONS

The combination of the results from the Eulerian analysis of the heat transport across the ridge and the Lagrangian approach sheds light on the overturning across the mid-ocean ridge. In the horizontal, there is a westward eddy-driven transport of warm water and an eastward eddy-driven transport of cold water across the ridge (Figure 3.11b). In the west, these two watermasses are connected via convection that takes place adjacent to the mid-ocean ridge (Figure 3.13c). Once transformed, the now cold watermass follows isopycnals across the ridge (Figure 3.13d). There, the cold watermass is transported by the mean northward flow along the ridge and subsequently by the boundary current out of the marginal sea. This overturning loop is closed by the transformation of the cold watermass back to the warm watermass. According to our numerical simulations, this takes place outside the Nordic Seas (represented in our model by the restoring region south of the island), not inside the Nordic Seas by diapycnal upwelling as proposed by *Isachsen and Nøst* (2012).

The transformation of watermasses along the front current seems very similar to the watermass transformation along the slope current as discussed by *Brüggemann and Katsman* (2019). They studied the gradual density changes of a slope current by separating the diapycnal transformation, which results from direct cooling by the atmosphere, from the isopycnal transformation; entrainment of dense interior waters along isopycnals into the slope current, induced by eddies. Based on the results of chapter 3 and the analysis presented in this appendix, the watermass transformation taking place along the front current is found to be a result of multiple processes that will likely respond differently to changes in the environment as they involve different timescales. It is therefore important to understand and measure the watermass transformation of Atlantic Water in the Nordic Seas from a full three-dimensional point of view.



# 4

## PATHWAYS AND WATERMASS TRANSFORMATION OF ATLANTIC WATER ENTERING THE NORDIC SEAS THROUGH DENMARK STRAIT

*The pathways and watermass transformation of the North Icelandic Irminger Current (NIIC) in the Nordic Seas are investigated by tracing the NIIC watermass in two ocean circulation models: the Modular Ocean Model (MOM) and the Parallel Ocean Program (POP). The two simulations use identical atmospheric forcing and have a horizontal resolution of  $0.1^\circ$ . However, the models differ strongly in their representation of the sea-ice cover in the Nordic Seas and, possibly as a consequence, display a different hydrography. Results from observational studies point towards a fast overturning loop north of Iceland that connects the NIIC watermass to the Denmark Strait Overflow Water (DSOW). However, our Lagrangian analysis shows that only 0.2 Sv of the entering NIIC water exits as DSOW in the two models. In POP, the main transformation to dense water takes place along a short path north of Iceland. In MOM however, the contributing part of the NIIC to DSOW takes a long path through the Nordic Seas and reaches Denmark Strait as part of the East Greenland Current (EGC). A small contribution of the NIIC watermass to the Iceland Scotland Overflow Water (ISOW) is found in both MOM and POP (7.8%, respectively 2.1% of the NIIC watermass). Analysis of the depth distribution and the thermohaline changes of the particles indicates that the watermass transformation that takes place north of Iceland is crucial for diversifying the pathways of the NIIC water.*

---

Results presented in this chapter have been published as: S.L. Ypma, Brüggemann, N., Georgiou, S., Spence, P., Dijkstra, H., Pietrzak, J.D. and Katsman, C.A., Pathways and watermass transformation of Atlantic Water entering the Nordic Seas through Denmark Strait in two high resolution models, Deep Sea Research part I: Oceanographic Research Papers, doi:10.1016/j.dsr.2019.02.002

## 4.1. INTRODUCTION

The transformation of Atlantic Water (AW) north of the Greenland-Scotland Ridge is one of the key mechanisms for controlling the strength of the Atlantic Meridional Overturning Circulation (AMOC) via the overflows through Denmark Strait and across the Iceland-Scotland Ridge. The warm AW flows poleward into the Nordic Seas and beyond through three main gateways (see schematic in Figure 4.1) (e.g. *Hansen and Østerhus*, 2000). Two of these, through which the majority of the AW flows north, are located east of Iceland. West of Iceland, AW is transported by the North Icelandic Irminger Current (NIIC). This third branch flows north along the western Icelandic slope and has been monitored since 1985 (e.g. *Jónsson and Valdimarsson*, 2005), though the fate of the NIIC has only recently been studied in more detail. Water mass transformation of the AW in the NIIC is thought to be linked to the densest part of the Denmark Strait Overflow Water (DSOW) (*Våge et al.*, 2011). However, as of yet it is unclear which path the NIIC takes after entering the Nordic Seas and where watermass transformation from the NIIC to DSOW takes place. The aim of this study is to investigate the paths and watermass transformation of the NIIC in detail in two ocean models using a Lagrangian approach.

Previous studies suggest three possible pathways for the NIIC. The first path was described by *Swift and Aagaard* (1981) as well as *Jónsson* (1992), who observed Atlantic Water at the north Icelandic continental shelf, without any propagation into the central Iceland Sea. They found that east of Iceland the water leaves the shelf and propagates in the direction of the Norwegian Sea. *Stefánnson* (1962) showed that part of the NIIC watermass mixes with surface water from the Iceland Sea, forming a watermass that connects to the Iceland Scotland Overflow Water (ISOW).

ISOW, which has a similar magnitude as DSOW, is formed by a mixture of watermasses that, combined, are generally labelled as Modified East Icelandic Water (MEIW). The main constituents of the MEIW are the North Icelandic Winter Water, the East Icelandic Water, the Norwegian Sea Deep Water and the Norwegian North Atlantic Water, where the latter is partly formed by transformation of the NIIC watermass (e.g. *Hansen and Østerhus*, 2000). The main outlet of these watermasses is through the Faroe-Shetland Channel.

Using surface drifters, *Valdimarsson and Malmberg* (1999) observed a second possible path for the NIIC, where most of their drifters seemed to be topographically steered northward by the Kolbeinsey Ridge (see Figure 4.1) and returned south through Denmark Strait in the East Greenland Current (EGC).

More recently, analyses from multiple hydrographic transects along the coast of Iceland suggested a third possible pathway. They point to a close relationship between the NIIC and the North Icelandic Jet (NIJ) (e.g. *Våge et al.*, 2011, 2013, 2015). The NIJ transports the densest component of the Overflow Water through Denmark Strait (*Våge et al.*, 2011). The other two currents advecting dense water from the north through the strait are the shelf break current and the separated branch of the EGC (*Harden et al.*, 2016). The observations show several indications of a connection between the NIIC and the NIJ. First, both currents can be traced along the continental slope of Iceland until their signal disappears at the northeast corner of the island (*Våge et al.*, 2011). Along the Icelandic shelf, the currents seem to be dynamically linked by sharing a pronounced density front (*Pickart et al.*, 2017). Second, the volume transport of both currents is very simi-

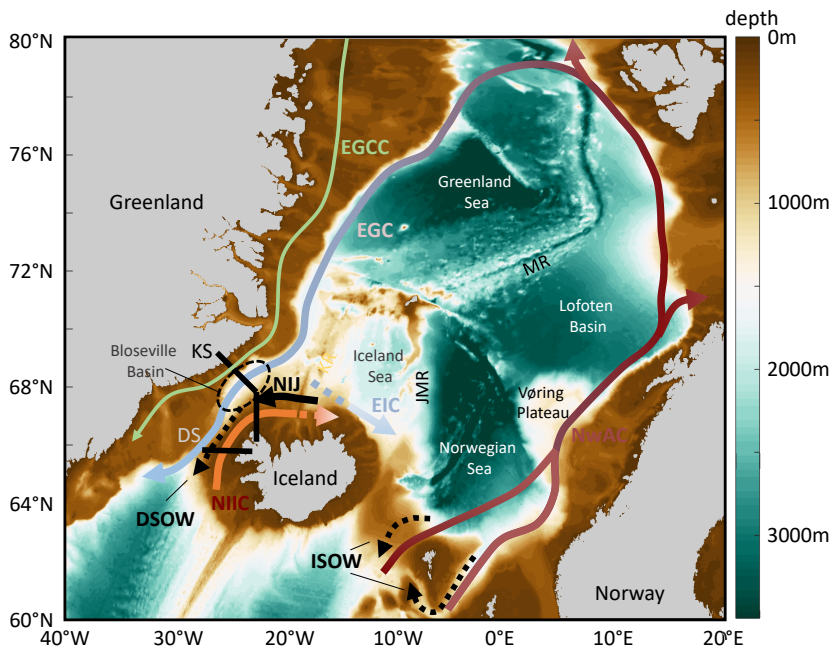


Figure 4.1: Schematic of the circulation in the Nordic Seas and bathymetry. Shown in red are the warm and salty inflowing currents: the North Icelandic Irminger Current (NIIC) and the Norwegian Atlantic Current (NwAC). The East Greenland Current (EGC) and the East Icelandic Current (EIC) are shown in blue and the East Greenland Coastal Current (EGCC) in green. Dense currents are shown in black: the North Iceland Jet (NIJ), the Denmark Strait Overflow Waters (DSOW, dashed line) and the Iceland Scotland Overflow Waters (ISOW, dashed lines). The bathymetric features pertinent for this study are marked: the Kolbeinsey Ridge (KR), the Jan Mayen Ridge (JMR) and the Mohn Ridge (MR). The release location of the particles at 66°N in Denmark Strait (DS) and the Kögur Section (KS) are shown in black. Note that the bathymetry is from ETOPO2v2, and not the model bathymetry.

lar. It is estimated to be 1 Sv and 0.88 Sv for the NIJ and NIIC, respectively (*Jónsson and Valdimarsson, 2012; Harden et al., 2016*).

*Våge et al. (2011)* showed, by using an idealized model set-up, that the mechanism that links the NIIC and the NIJ is similar to the one described by e.g. *Spall (2004)* and *Straneo (2006b)*. These studies suggest that buoyant water from the NIIC is transported to the interior of the Iceland Sea by eddies due to baroclinic instability of the NIIC. In these idealized models, the heat flux from the boundary current to the interior balances the atmospheric cooling over the interior that induces convection. The dense watermass returns to the Icelandic slope where it sinks and forms the NIJ.

So far, follow-up studies have not been able to corroborate the connection between the NIIC and the interior of the Iceland Sea. Using measurements from eight shipboard surveys, *Pickart et al. (2017)* find a strong, in phase correlation in salinity between the NIJ and NIIC. In case the two currents are linked, this would imply the existence of a very fast overturning. To accommodate this short time-scale, they hypothesize that the overturning can not take place in the central Iceland gyre, but instead takes place northwest of the gyre where deep mixed layers are observed. In their discussion it remains unclear how the water of the NIIC reaches this area. Additionally, *de Jong et al. (2018)* do not find a connection between the interior Iceland Sea and the NIJ either. In their study, based on the analysis of deployed RAFOS floats, they highlight the importance of the East Icelandic Current (EIC, Figure 4.1) that potentially blocks the exchange between the Iceland Sea gyre and the Icelandic slope region. This branch might not be captured by the idealized model of *Våge et al. (2011)*. Tracking the NIJ watermass back in time in a high resolution ocean model (Viking20) leads to a similar insight: no exchange with the interior of the Iceland Sea is seen and most of the NIJ originates from the shelfbreak EGC (*Behrens et al., 2017*). It is therefore still unclear what role the NIIC plays for the formation of Denmark Strait Overflow Waters.

Lagrangian studies as *Behrens et al. (2017)* can be very useful as particle tracking in global ocean models has the advantage that a large number of particles can be used in comparison to observations, providing better statistics of variable pathways. However, different ocean models lead to different conclusions. For example, backtracking the overflow waters in the  $1/20^\circ$  horizontal resolution Viking20 ocean model, *Behrens et al. (2017)* find that the bulk part of the Denmark Strait Overflow Water in the model (60%) has an Arctic origin. In contrast, in the  $1/10^\circ$  ocean model used by *Köhl (2010)* the largest part of the DSOW originates from watermass transformation taking place within the Nordic Seas. *Köhl (2010)* argues that the pathways vary spatially depending on the magnitude of the wind stress. Thus, he concluded that the differences in ocean models regarding forcing and set-up may lead to significantly different results.

In addition to the variables mentioned by *Köhl (2010)*, the horizontal resolution, discretization in the vertical, topography, mixing parameterizations and boundary conditions like applied atmospheric forcing and sea-ice conditions impact the mixed layer dynamics and therefore the circulation in the models (*Willebrand et al., 2001; Langehaug et al., 2012; Courtois et al., 2017*). A correct representation of the convection regions is crucial for the transformation processes of watermasses. However, ocean models still show large differences in mixed layer depth, both in low- and high resolution ocean models (e.g. *Tréguier et al., 2005; Danabasoglu et al., 2014*).

The aim of this study is to investigate to what extent the inflowing Atlantic Water through Denmark Strait contributes to the Overflow Water and whether its transformation is related to the location of convection regions within the Nordic Seas as proposed by *Våge et al.* (2011). A Lagrangian perspective is chosen, where the NIIC watermass entering the Nordic Seas through Denmark Strait is tracked in two ocean models that differ substantially in their representation of deep convection: the Modular Ocean Model (MOM) and the Parallel Ocean Program (POP). The models have the same horizontal grid with a resolution of  $0.1^\circ$  degree and identical atmospheric forcing. However, their sea-ice representation and consequently the hydrography in the Nordic Seas is different. This chapter presents the pathways of the NIIC water in these two models, a quantification of the contribution of the NIIC to the overflows and a discussion on where and how the NIIC watermass is transformed.

The chapter is structured as follows. Section 4.2 describes the model simulations analysed and the particle tracking method. In section 4.3 the performance of both models in the Nordic Seas is compared to observations. This is followed by the main results of this study, where the pathways of the NIIC watermass are described in detail in section 4.4 and the watermass transformation along the pathways is discussed in section 4.5. A discussion and the conclusions are provided in section 4.6.

## 4.2. METHODS

In this study, a Lagrangian analysis is conducted to trace the NIIC watermass. Numerical particles are advected offline using the velocity fields of the model output. The particles' location, depth, temperature and salinity are saved and used to determine the pathways and watermass transformation of the NIIC water. This method is applied to two ocean models that differ substantially in their representation of deep convection and sea ice in order to investigate the sensitivity of the results to the location of deep mixed layers and heat fluxes.

### 4.2.1. GLOBAL OCEAN MODEL CONFIGURATIONS

The particles are advected in the Modular Ocean Model global ocean-sea ice model (MOM) and the Parallel Ocean Program ocean-only model (POP). The ocean model configurations are described in detail by *Spence et al.* (2017) (MOM) and *Weijer et al.* (2012) (POP) and form the ocean component of frequently-used climate models (MOM in GFDL-CM2.6 and POP in CESM1.0). The models have the same horizontal resolution of  $0.1^\circ$  and use a tripolar B-grid. This yields  $\sim 4.5$  km resolution at  $65^\circ\text{N}$ . *Nurser and Bacon* (2014) estimated the first Rossby Radius of deformation to be  $\sim 7$  km in the Norwegian Sea and  $\sim 3$  km in the Iceland and Greenland Sea. Therefore, these ocean models are only partly eddy resolving in the region of interest. In the vertical, MOM (POP) has 50 (42) layers with a resolution of 5m at the surface up to 200m (250m) in the deeper layers.

Both models are forced by prescribed atmospheric conditions using the Coordinated Ocean-ice Reference Experiments Normal Year Forcing (COREv2-NYF) reanalysis data (*Griffies et al.*, 2009; *Large and Yeager*, 2009). COREv2-NYF provides a climatological mean atmospheric state estimate at 6-hour intervals at roughly  $2^\circ$  horizontal resolution. The atmospheric state is converted to ocean surface fluxes by bulk formulae, so there

are no air-sea feedbacks. The Normal Year Forcing is derived from 43 years of the inter-annual varying atmospheric state from 1958 to 2000. Since the same seasonal forcing is applied every year, the interannual variability is small. Using normal year forcing is advantageous for this study as the results will not depend on the release year of the numerical particles. For practical reasons, only one year of velocity data representative for the mean ocean state of the models is used in this study.

The KPP parameterization is used for the parameterization of convection in both models (*Large et al.*, 1994). Further, vertical viscosities and diffusivities are set by KPP and in the horizontal, biharmonic viscosity and diffusion are used. In MOM, the surface salinity is restored on a 60-day timescale. In POP, the surface salinity is restored during the first 75 years of the spin-up period. From that moment onwards, ‘mixed boundary conditions’ are applied, derived from the monthly-averaged restoring flux of the final five years of the spin-up.

The models differ in their sea-ice configurations. MOM is coupled to the GFDL Sea Ice Simulator model, so the sea ice evolves freely. In POP, the sea-ice edge is fixed and defined by the  $-1.8^{\circ}\text{C}$  isotherm of the SST climatology from COREv2-NYF. Under the diagnosed sea ice, temperature and salinity are restored with a timescale of 30 days. The approaches regarding the sea-ice configurations in MOM and POP lead to large differences in the maximum sea-ice extent in the Nordic Seas, as shown by the black line in Figures 4.2b and 4.2c. In POP the maximum sea-ice extent is confined to the continental shelves of Greenland, whereas in MOM the sea ice covers most of the Greenland and Iceland Seas in winter months. Additionally, Figure 4.2 shows that the modeled hydrographic fields of the two models differ as well. Section 4.3 will further elaborate on these differences with respect to observations.

#### 4.2.2. TRACKING THE ATLANTIC WATER NORTH THROUGH DENMARK STRAIT

Lagrangian particles are released daily for a duration of one year in the northward flowing Atlantic Water in Denmark Strait. The particles are released at a zonal transect at  $66^{\circ}\text{N}$  between Iceland and  $28.9^{\circ}\text{W}$  (black line in Figure 4.1 in Denmark Strait) at a resolution of  $0.1^{\circ}$  longitude and 20m in the vertical. The particle is only traced when the initial meridional velocity is positive (hence flowing to the north) and when the initial temperature is higher than  $5^{\circ}\text{C}$  (hence Atlantic Water). Each particle is tagged with its corresponding volume transport that is defined as the meridional velocity multiplied by the area of the cell face in which the particle is released (*Döös*, 1995).

The particles are advected forward in time with a timestep of 1 hour within the daily averages of the 3D velocity field output of the ocean model using the Connectivity Modeling System (CMS) (*Paris et al.*, 2013). The CMS model uses a tricubic interpolation spatially, and a  $4^{\text{th}}$  order Runge Kutta stepping scheme in time. No horizontal or vertical diffusivity is added to the particles, so the particle motion is purely advective. Mixing is only taken into account as far as it is represented by resolved eddies. The CMS model does include the option to parameterize the vertical movement in mixed layers by adding a random kick in the vertical to the particle trajectories (*van Sebille et al.*, 2013). Results of including this option are compared to results without the parameterization, and no significant changes were found in the particle pathways and the watermass transformation along the paths. The change in density of the particles in the convection region defines

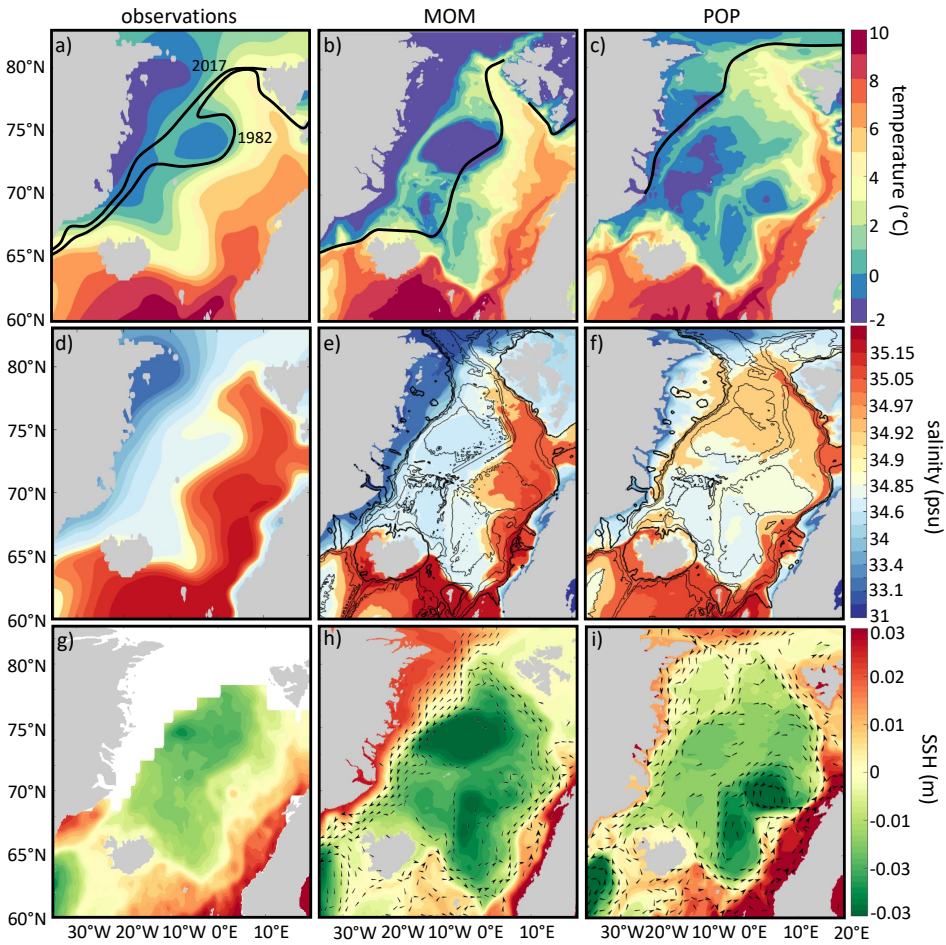


Figure 4.2: Mean temperature (top) and salinity (middle) at 50m depth and sea surface height (bottom) from (a,d,g) observations, (b,e,h) MOM and (c,f,i) POP. The observational hydrographic fields show the mean from 1995 to 2010 and are obtained from the Climatological Atlas of the Nordic Seas (*Korablev et al., 2014*). Panel (g) shows the mean absolute dynamic topography over the same period from the AVISO satellite altimetry. The black lines in (a-c) indicate the sea-ice extent over the same period from the AVISO satellite altimetry. The black lines in (a) the extent in 1982 and 2017 are shown from the Sea Ice Index (*Fetterer et al., 2017*). The contour lines in (e) and (f) show the model isobaths at 400m (thick black line), 1000m, 1500m and 3000m depth. The black arrows in (h) and (i) show the mean surface velocity field for flow stronger than 0.05 m/s.

the future path, as the particles have to follow isopycnals. It does not matter at which depth the particle is located within the mixed layer, since the T-S properties of the mixed layer are continuously homogenized by the convective adjustment used in the model simulations. Therefore, the results of the CMS model without the parameterization of the vertical movement in mixed layers have been used in this study.

In total 226407 (284412) particles are tracked in MOM (POP). The total advection time of the particles is chosen to be 6 years and is executed by looping through the available data set of one year of model output. The resulting pathways and timeseries of temperature and salinity of the particles do not show large variations from the end of December to the beginning of January, which justifies this method. After six years, the majority of the particles has left the Nordic Seas (81% in MOM and 69.8% in POP, see section 4.4 and Figure 4.6).

The resulting pathways are then visualized using a particle density plot (see section 4.4 and Figure 4.5). To this end every particle location is regridded on a  $0.1^\circ \times 0.1^\circ$  latitude-longitude grid. Each position can only be occupied by the same particle once, to avoid the obscuration of the pathways by long residence times as described by *Behrens et al.* (2017). The particle density is given by the transport carried by the particles at each location divided by the total transport. This way, the paths that the particles are most likely to take are highlighted.

### 4.3. MODEL PERFORMANCE IN THE NORDIC SEAS

Apart from the different sea-ice configuration and the SSS restoring, the set-up of the two models is very similar, as described in section 4.2.1. Still, the resulting hydrography and circulation is remarkably different. In this section, a comparison of the two models is made and the modeled fields are validated against observations to highlight possible consequences of the different model configurations. Also, the interpretation of the findings from the Lagrangian approach in sections 4.4 and 4.5 requires knowledge of the Eulerian background velocity and hydrography. The first part of this section compares the Nordic Seas hydrography and the mixed layer depth from each model to observations. The second part addresses the circulation in both models and the third part discusses the hydrography at the Kögur section (see Figure 4.1) to investigate the properties of the NIIC and the Denmark Strait Overflow Water.

#### 4.3.1. HYDROGRAPHIC PROPERTIES

The mean temperature and salinity at 50m depth of both models is compared to the observed fields of the Nordic Seas from 1995 to 2010 in Figure 4.2a-f. A depth of 50m is chosen, since at this depth the difference in temperature between the eastern and western basins is more pronounced than at the surface. Apart from some local discrepancies, both models compare well to the observed hydrography in the Nordic Seas. The hydrographic fields in MOM differ from the observations on the western side of the Nordic Seas. The Greenland Sea and Iceland Sea are colder than observed ( $\Delta T \sim 2^\circ\text{C}$ , Figure 4.2b) and the waters near the Greenland coast are too fresh ( $\Delta S \sim 0.5$  psu, Figure 4.2e). In POP, a warm and saline signal that is not present in observations, seems to propagate onto the northern Greenland shelf region at  $80^\circ\text{N}$  (Figures 4.2c and 4.2f). Furthermore,

the lateral spread of the Atlantic Water throughout the eastern basins is minimal in POP. Instead, a local minimum in temperature is seen in both the Lofoten Basin and the Norwegian Basin (Figure 4.2c). Further, the Atlantic Water returning in the EGC is warmer in MOM than in POP, indicating that the boundary current in POP loses more heat than the boundary current in MOM (see also table 4.1).

The location where deep convection takes place in both models is very different. Figure 4.3a and 4.3b show the maximum mixed layer depth (MLD) in MOM and POP. In order to use a common criterion for both models, the MLD is defined as the depth where the density difference compared to the surface is larger than  $0.125 \text{ kg/m}^3$  as described in *Danabasoglu et al.* (2014). The density is determined from the temperature and salinity fields using the UNESCO nonlinear equation of state (*Millero and Poisson*, 1981). The maximum in MLD is reached at the end of winter and beginning of spring. The models display a clear difference in both the magnitude and the location of deep convection. In MOM the convection reaches 1000m depth, and the deepest mixed layers are seen southwest of Svalbard and within the Norwegian Atlantic Current (Figure 4.3a). In contrast to MOM, POP has mixed layers with a maximum of 1500m depth along the shelf break of Greenland, into the Greenland Basin and north of the Icelandic Plateau (Figure 4.3b).

The location and depth of deep convection are strongly dependent on the atmospheric forcing, the sea ice and the stratification of the water column (e.g. *Moore et al.*, 2015; *Harden et al.*, 2015; *Våge et al.*, 2018). Comparing the location and the depth of the deep convection to the atmospheric heat flux (contours in Figure 4.3) and the sea-ice edge in March (dashed lines in Figure 4.3) confirms this. In MOM the edge of the deep convection region coincides with the  $-100 \text{ W/m}^2$  heat flux contour (Figure 4.3a). Furthermore, it is clear that the deep convection in the western basin is absent because the sea ice is preventing the cooling of the ocean surface by the atmosphere. In POP the sea-ice edge, which is located much closer to the Greenland coast (see dashed line in Figure 4.3b), also plays an important role for the location of the deep convection. The strongest heat fluxes are found along the sea-ice edge, which makes the water column more prone to deep convection.

Observational estimates of the mixed layer depth in the Nordic Seas are limited due to the lack of year-round observational data. Mixed layers with depths of 560m have been observed in the Lofoten and Norwegian Basins (*Nilsen and Falck*, 2006; *Richards and Straneo*, 2015). The deep convection in the Greenland Sea is highly variable and can extend to depths of 2000m (*Rudels et al.*, 1989; *Latarius and Quadfasel*, 2016). Combining all available observational data in the Iceland Sea, *Våge et al.* (2015) found that the deepest mixed layers in this basin ( $\sim 300\text{m}$ ) are located in the northwest, close to Greenland. These findings suggest that the deep convection in the Greenland Sea is better represented in POP and the deep convection in the Lofoten Basin is better represented in MOM. Further, POP overestimates the maximum MLD in the Iceland Sea, whereas in MOM deep convection does not occur in this region. These differences are likely a direct consequence of the difference in sea-ice behavior between the models. Recall that the sea-ice extent in POP is fixed to observed values, whereas in MOM the sea ice is dynamically active. Apparently, the sea-ice model used in MOM is overestimating the sea-ice extent in the Nordic Seas, which suppresses deep convection in the western basins.

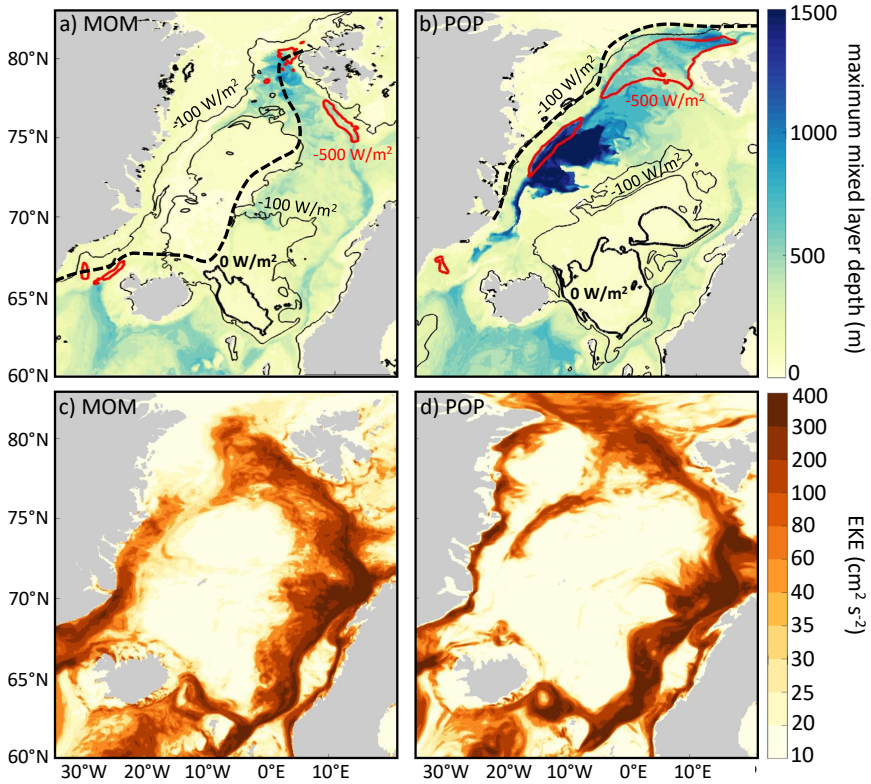


Figure 4.3: Maximum mixed layer depth (top) and eddy kinetic energy (bottom) for MOM (left) and POP (right). Solid contours in (a) and (b) show the  $-500 \text{ W/m}^2$  (in red),  $-100 \text{ W/m}^2$  and  $0 \text{ W/m}^2$  (in black) March mean heat flux. The dashed contours indicate the sea-ice extent in March.

#### 4.3.2. NORDIC SEAS CIRCULATION

The circulation pattern in the Nordic Seas is strongly controlled by topography, while the strength of the circulation is influenced by the wind forcing and hydrography (e.g. *Blindheim and Østerhus, 2005; Spall, 2010*). Figures 4.2g-i show the mean sea surface height (SSH) from observations, and in MOM and POP. The SSH in both models compares quite well to observations, except in the Lofoten Basin. Especially in POP a depression in SSH is clearly seen in the Lofoten Basin, whereas a positive SSH anomaly is commonly observed in this area associated with the Lofoten Vortex (e.g. *Soiland et al., 2016; Fer et al., 2018*). The arrows in Figures 4.2h and 4.2i show the mean surface velocity in both models. The location and direction of the currents compare well to the observed surface circulation derived from drifters by e.g. *Jakobsen et al. (2003)*. The model results differ regarding the strength of the currents. POP has a very strong cyclonic gyre in the Lofoten Basin and the Norwegian Basin, but the circulation in the Greenland and Iceland Basin

is weaker. In MOM cyclonic gyres are most pronounced in the Greenland Basin and the Norwegian Basin. As the EGC in POP is very weak (see also table 4.1), most Arctic Water is transported southwards by the East Greenland Coastal Current. In MOM this current is less pronounced.

When the circulation is compared to the structure of deep convection in the basin (Figures 4.2h-i to 4.3a-b), the regions with convective activity coincide with regions of low velocity in both models. This seems contradictory at first, since deep convection in the interior of ocean basins is thought to be positively correlated with the strength of the cyclonic boundary current that is surrounding the basin: as the interior of the ocean basin is cooled during winter, the temperature gradient between the boundary current and the interior increases and the boundary current strengthens as a result of the thermal wind balance (e.g. *Spall, 2004; Tréguier et al., 2005*). However, in our simulations a strong cooling coincides with a weak temperature gradient between the interior and the boundary current and therefore with a reduced geostrophic transport. The reduced temperature gradient is probably caused by the stronger cooling over the boundary current area compared to the interior. This heat loss seems to be so strong that the supply of warm water from the boundary current upstream is not sufficient and thereby, the boundary current temperature decreases.

The eddy kinetic energy (EKE) is shown in Figures 4.3c-d. Although the model resolution is not sufficient to fully resolve all eddy activity in the Nordic Seas, most of the variability is captured. The largest eddy variability is seen west of the Lofoten islands. Here, the EKE exceeds  $400 \text{ cm}^2\text{s}^{-2}$ , which compares relatively well to observational estimates (e.g. *Wekerle et al., 2017*). North of Iceland a small band of increased EKE from the NIIC can be seen. Both observational estimates of the eddy variability in this region and estimates from higher resolution model simulations show slightly larger values for EKE of  $\sim 100 \text{ cm}^2\text{s}^{-2}$  compared to  $\sim 60 \text{ cm}^2\text{s}^{-2}$  in MOM and POP (e.g. *Jakobsen et al., 2003; Wekerle et al., 2017*).

### 4.3.3. HYDROGRAPHIC PROPERTIES AT KÖGUR SECTION

Next, the properties of the inflowing Atlantic Water and the outflowing Overflow Water through Denmark Strait are compared between the models and mooring observations at the Kögur section (*Harden et al., 2016*). This transect is well documented from observations and the characteristics of both the inflowing NIIC and the outflowing dense waters can be distinguished along the section. Further, to enable direct comparison between the models and observations, table 4.1 shows the mean temperature, salinity and volume transport estimates of the NIIC, DSOW, NIJ and EGC.

Figure 4.4 shows the mean temperature, salinity and the cross-section velocity (positive indicates northward flow) at the Kögur section. The mean temperature along the Kögur transect in MOM captures the observed pattern well (Figure 4.4b), although the deep waters are too warm ( $\Delta T \sim 1^\circ\text{C}$ , Figure 4.4b). In POP, the stratification is much stronger than observed, with warmer water at the surface ( $\Delta T \sim +2^\circ\text{C}$ ) and colder waters below ( $\Delta T \sim -1.5^\circ\text{C}$ , Figure 4.4c). The salinity shows similar discrepancies, where the surface and deep layers are too fresh in MOM and too salty in POP by  $\sim 0.1$  psu compared to the observations (Figures 4.4e and 4.4f). Combining the findings for temperature and salinity, the in- and outflowing waters in MOM are slightly too light and the in- and out-

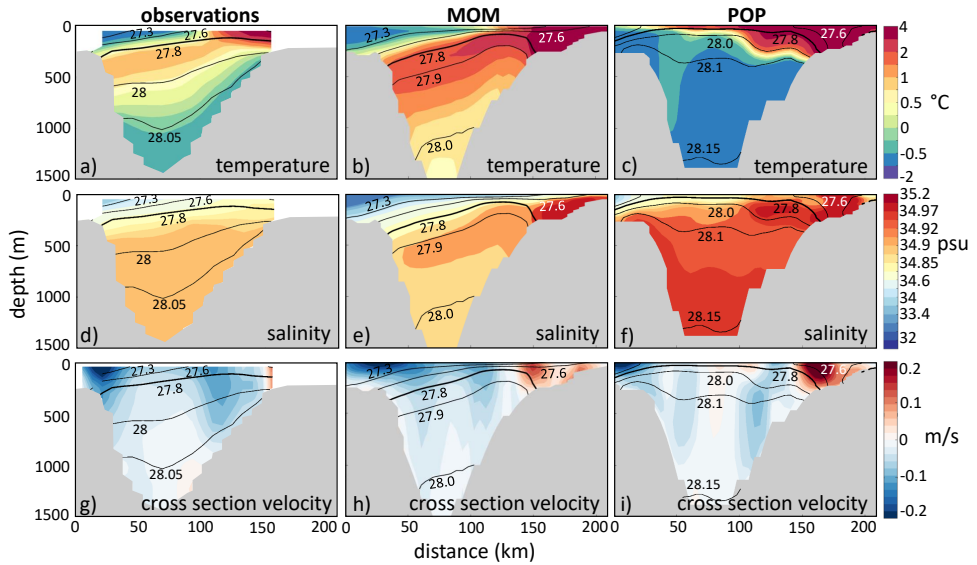


Figure 4.4: Sections of temperature (top), salinity (middle) and cross section velocity (bottom) at the Kögur section (transect given in Figure 4.1). The x-axis shows the distance along the transect, starting at the Greenland coast. Positive velocity indicates northward flow. The left column shows the mean fields from observations described by *Harden et al.* (2016). The middle and right column show the mean fields of MOM and POP respectively. Density is given by the contourlines, where the thick black line corresponds to  $\sigma = 27.8 \text{ kg/m}^3$ . Note that the colorbars for temperature and salinity are non-linear.

Table 4.1: Mean transport ( $\Psi$ ), temperature (T) and salinity (S) of the NIIC, DSOW, NIJ and EGC from observations and the model simulations. Observational values are estimated from [1] *Våge et al.* (2013), [2] *Jónsson and Valdimarsson* (2005), [3] *Pickart et al.* (2017), [4] *Jochumsen et al.* (2017), [5] *Eldevik et al.* (2009), [6] *Harden et al.* (2016) and [7] *Håvik et al.* (2017).

	observations	MOM	POP		observations	MOM	POP
NIIC				DSOW			
$\Psi$ (Sv)	1.1 <sup>[1]</sup>	1.1	1.8		3.2 <sup>[4]</sup>	2.5	3.1
T (°C)	3-6 <sup>[2]</sup>	6.2	6.6		0.1-0.5 <sup>[5]</sup>	2.5	-0.5
S (psu)	35-35.15 <sup>[3]</sup>	35	35.1		34.82-34.94 <sup>[5]</sup>	34.9	35
NIJ				EGC (76°N)			
$\Psi$ (Sv)	1±0.17 <sup>[6]</sup>	0.5	1.3		5-7 <sup>[7]</sup>	7.5	2.8
T (°C)	-0.4-0 <sup>[3]</sup>	1.4	-0.4		2-4 <sup>[7]</sup>	2.3	0.7
S (psu)	34.9-34.91 <sup>[3]</sup>	34.9	35		34.9-35.1 <sup>[7]</sup>	34.9	35

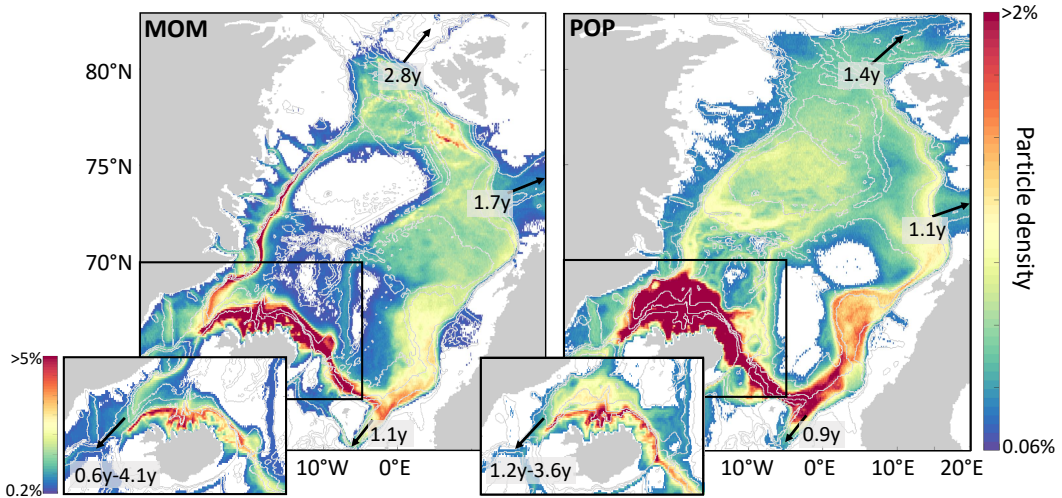


Figure 4.5: Density plot of the particle position in MOM (left panel) and POP (right panel). The inlay shows the pathways near Iceland in more detail (note the different colorscale in the bottom left). The median travel time for the particles to reach the exits of the Nordic Seas is given in years.

flowing waters in POP are too dense.

In the cross-section velocity at the Kögur section different branches can be distinguished (Figures 4.4g-i). The NIIC is present in both models and is characterized by a warm and salty water mass flowing north on the Icelandic shelf. The NIIC transport is 1.1 Sv in MOM and 1.8 Sv in POP compared to 0.88-1.1 Sv estimated from observations (*Jónsson and Valdimarsson, 2012; Våge et al., 2013*). As a result of the model bias in density, the overflow water is characterized by different isopycnals. The  $27.8 \text{ kg/m}^3$  respectively  $28.0 \text{ kg/m}^3$  isopycnals are chosen to represent the overflow water mass in MOM and POP. This results in an overflow transport into the Atlantic of 2.4 Sv in MOM and 3.1 Sv in POP, which is slightly lower than the observed estimate of 3.2 Sv from *Jochumsen et al. (2017)*. Compared to observations, the NIJ is better represented in POP than in MOM (see table 4.1).

In summary, this section discussed the differences between the models and observations. Overall, the models capture the main characteristics of the Nordic Seas well, but disagree on the location of deep mixed layers, the gyre strength in the Nordic Seas and the hydrographic characteristics of the Denmark Strait Overflow Water. The remainder of this chapter will focus on whether these differences influence the pathways of the NIIC water and the location and strength of the watermass transformation.

#### 4.4. PATHWAYS OF THE NIIC WATERMASS IN THE NORDIC SEAS

The density plot of the particles seeded in the NIIC (see section 4.2.2) reveals the pathways of the NIIC watermass in the Nordic Seas (Figure 4.5). After entering the Nordic Seas, most particles follow the 400m isobath around Iceland to the east (see inlays Fig-

ure 4.5). From there, multiple pathways can be identified following the shelfbreak and the main topographic features of the Nordic Seas; the Vøring Plateau and the Jan Mayen and Mohn Ridges (see Figure 4.1).

These particle density plots show that the paths along which the particles enter the interior of the Nordic Seas are completely different between the two models. Particles mainly occupy the Lofoten Basin in MOM, whereas in POP the particles occupy the Greenland Basin. In MOM, particles are captured by eddies near the Lofoten Islands and travel westward until they reach the Mohn Ridge. There, the majority of the particles flows to the north and eventually joins the EGC. In POP, the particles are not captured by eddies near the Lofoten islands, but are transported in the strong cyclonic gyre of the Lofoten Basin and the Norwegian Basin instead. At the western side of the Nordic Seas, particles travel throughout the Greenland Basin, without displaying one distinctive path.

The residence time of the particles within the Nordic Seas is highly variable and depends on where the particles leave the basin. The median travel time is given in Figure 4.5 for the particles that enter and leave the Nordic Seas within the time interval of 6 years (section 4.2.2). The shortest residence times of  $\sim 1$  year are found for particles taking a short path crossing the Greenland-Scotland Ridge, whereas the particles that follow the path along the rim of the Nordic Seas take  $\sim 4$  years to do so. On average, the travel time towards Fram Strait is one year shorter in POP than in MOM, which indicates that the particles flow much faster from the Lofoten Islands to Fram Strait in POP than in MOM.

In order to distinguish between the different paths, particles are selected based on which exit they take out of the Nordic Seas. This particle categorization process is illustrated in Figure 4.6a. Furthermore, a selection is made based on whether particles enter the interior of the Nordic Seas, or stay close to the boundary with respect to the coastlines of Iceland, Norway, Svalbard and Greenland. Although the categorization is sensitive to the choice of the transects shown in Figure 4.6a, inspection of the individual particle trajectories indicates that the transect locations used in this study lead to a meaningful separation.

The result of this categorization process is summarized by Figures 4.6b and 4.6c. In both models, most of the NIIC watermass leaves the Nordic Seas toward the Atlantic Ocean by crossing the Greenland-Scotland Ridge (66.7% in MOM and 42.5% in POP). A smaller fraction of the NIIC watermass flows into the Arctic via Fram Strait or the Barents Sea (14.3% in MOM and 27.3% in POP). The part of the NIIC water that takes longer than 6 years to leave the Nordic Seas (19% in MOM and 30.2% in POP) is found mostly in the interior of the basin (not shown). A much longer advection time would be needed to advect all of the originally seeded NIIC particles out of the Nordic Seas.

The particles leaving the Nordic Seas through Denmark Strait can do so following different paths as indicated in Figures 4.6b-c; via a short loop north of Iceland (the DSs, short, path), via the rim of the Nordic Seas (the DSI, long, path), via the interior of the Nordic Seas (the DSm, middle, path) and via the coastal shelf area of Greenland (the DSc, coastal, path). As the connection of the NIIC to the overflow is the main interest of this study, the remainder of this chapter is focused on the NIIC water returning to the Atlantic Ocean. Although the sea-ice cover, the mixed layers, and the transport of the NIIC show a seasonal dependence in the two model simulations, the pathways of the NIIC watermass are not sensitive to the time of release of the particles.

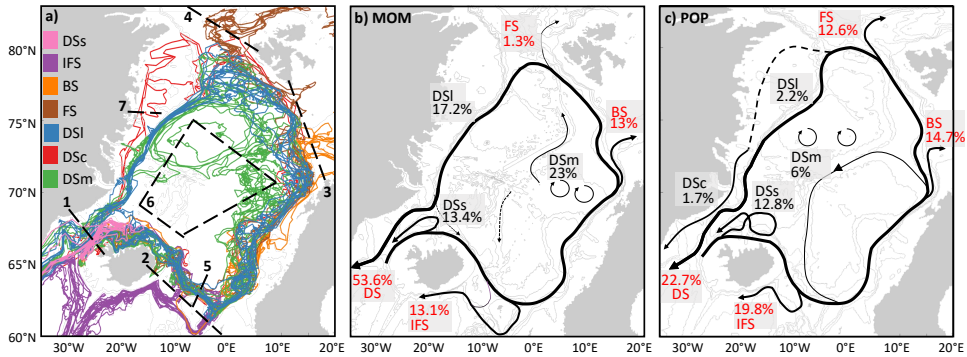


Figure 4.6: (a) Example of 63 randomly chosen particle trajectories from both MOM and POP and their categorization (color coding). DSs (Denmark Strait short, pink) are particles that leave the Nordic Seas crossing transect 1, without crossing transect 5. IFS particles (Iceland-Faroe-Shetland, purple) are particles that leave by crossing transect 2. BS (Barents Sea, orange) are particles that travel into the Barents Sea crossing transect 3. FS (Fram Strait, brown) are particles that travel into the Arctic Ocean by crossing transect 4. DSI (Denmark Strait long, blue) are particles that travel along the rim of the Nordic Seas, crossing transects 5 and 1. DSc (Denmark Strait coast, red) are particles that follow the same route as DSI, but travel on the shelf region of Greenland crossing transect 7. DSm (Denmark Strait middle, green) are particles that enter the interior of the Nordic Seas indicated by box 6 and leave the Nordic Seas through transect 1. (b-c) The black arrows indicate the paths of the NIIC water in the Nordic Seas where the percentage gives the distribution of the NIIC watermass over the different pathways. The total fraction of the NIIC watermass that leaves through each exit is given in red. 19% (30.2%) of the particles are still in the Nordic Seas after 6 years in MOM (POP).

Both models show the existence of a short loop along the inflowing NIIC back to Denmark Strait (the DSs path). At first sight, this path seems similar to the hypothesized path of *Våge et al.* (2011). However, only 13% of the volume that entered the Nordic Seas in the NIIC is taking this path in both MOM and POP, in contrast to the fast one-to-one connection between the NIIC and the NIJ proposed by *Pickart et al.* (2017). Furthermore, investigation of the particles' depth is needed in order to see whether this outward branch is actually part of the NIJ. To this end, the vertical distribution of the in- and outflowing branches of the different pathways at the Kögur section are visualised in Figures 4.7a and 4.7b. To derive this figure, the particles crossing this transect are mapped on a  $0.1^\circ \times 10\text{m}$  longitude-depth grid. Only the contour that encompasses more than 80% of the particles is shown to highlight the main position of each pathway in the watercolumn.

In both models, most of the DSs watermass originates from the upper 100m of the NIIC (solid pink contour in Figures 4.7a-b), and this path is therefore shallower than the other paths. The particles follow the shelf break of Iceland and turn northwards at Kolbeinsey Ridge. In MOM, the particles return to Denmark Strait following the 1000m isobath along the Icelandic slope. In POP, some particles circulate in the Bloesville Basin (Figure 4.1) as well. On their outward journey, there is no indication in MOM that the DSs particles are connected to the NIJ, since the returning particles are all located in the upper 100m of the water column (pink dashed line in Figure 4.7a). In POP, however, there is a clear signal of outward flowing particles between 200m and 400m depth close to the Icelandic slope (pink dashed line Figure 4.7b), showing that in this model the outward

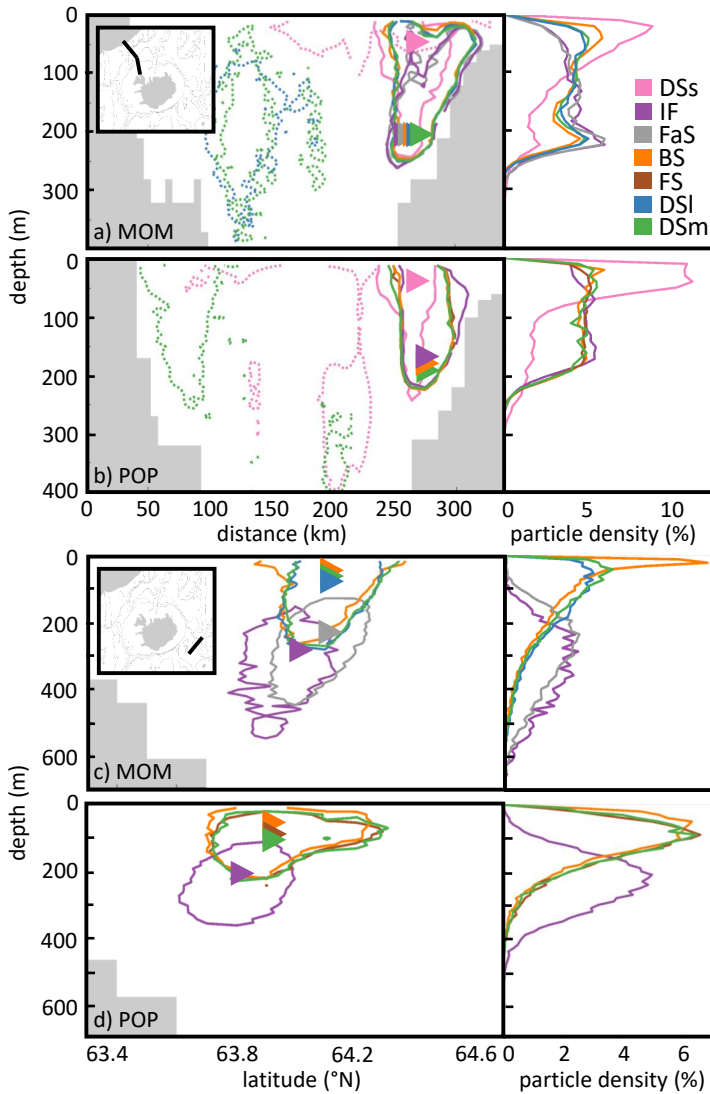


Figure 4.7: The depth distribution of each pathway at (a,b) Kögur section and (c,d) a section east of Iceland (see inlays). The left panels show the contour, colored per pathway, that encompasses >80% of the particles. The triangles give the location where the maximum particle concentration of the pathway is found at these transects. The solid contours show the distribution of the particles that flow into the Nordic Seas, the dashed lines show the distribution of the pathways on their outward journey. The right panels show the normalized depth distribution of each path integrated along the transects. The IFS particles are separated in those that leave the Nordic Seas between Iceland and the Faroe islands (IF, in purple) and those that leave the Nordic Seas between the Faroe Islands and Scotland (FaS, in gray). Only the paths that carry more than 5% of the NIIC water are shown.

branch is part of the NIJ. This indicates that the watermass transformation of the particles following the DSs path is different in both models. This will be further discussed in section 4.5.

As only 13% of the NIIC watermass takes the DSs path, the majority of the water is transported by other paths. A significant fraction of the NIIC watermass leaves the Nordic Seas between Iceland and the Shetland islands in both models (the IFS path, 13% in MOM and 20% in POP). In POP, all of the IFS particles leave the Nordic Seas between Iceland and the Faroe Islands (the IF path), whereas in MOM the majority of the IFS particles (>60%) leaves through the deeper channel between the Faroe Islands and Scotland (the FaS path). Again, the vertical distribution of the pathways is investigated by mapping the particles on a  $0.1^\circ \times 10\text{m}$  latitude-depth grid of a transect east of Iceland (Figure 4.7c and 4.7d). Clearly, the IFS particles (purple color in Figure 4.7c-d) are located deeper in the water column than the particles of the other pathways. In MOM, the particles leaving between the Faroe Islands and Scotland are located slightly farther offshore. Therefore, they follow the 1000m isobath to the Faroe-Shetland Channel. The possible connection of the IFS path to the Iceland Scotland Overflow Water (ISOW) will be discussed in section 4.5.

Investigation of the vertical distribution of the pathways at the Kögur section and the transect east of Iceland gives insight into why some particles flow south (the IFS path) and why some flow northward east of Iceland (the BS, FS, DSm, DSI and DSc paths). At the start of their trajectory, the maximum concentration of the particles that do not take the DSs path is found at 200m depth in both models (see triangles in Figures 4.7a and 4.7b). However, east of Iceland, the particles that continue their journey north are all shifted upwards in the water column, whereas most particles that flow south are found below 200m depth (compare the purple and gray contours to the other colors in Figure 4.7c and 4.7d). The upper part of the water column east of Iceland is characterized by the Atlantic Water flowing north in the NwAC. Particles that are located near the surface are therefore likely to mix with the inflowing Atlantic Water and flow north, whereas the deeper particles follow the topography to the south.

These results indicate that processes that take place between the two investigated transects are crucial for setting the ratio of the southward and northward flowing fraction of the NIIC. The instability of the NIIC in this region (see Figure 4.3c-d) could provide one possible mechanism for setting these pathways apart. The generation of eddies coincides with local up- and downward movement of isopycnals and this process could separate particles in depth (Ypma *et al.*, 2016). Another possible mechanism is that the particles are set apart in depth by local mixing within the mixed layer, which influences their density. It is beyond the scope of this study to determine the dominant processes in this region that are important for the transformation of the NIIC watermass. However, it is likely that the ratio of the southward and northward flowing fraction of the NIIC is subject to interannual variability.

The particles that flow north in the NwAC can take different routes. They either flow into the Barents Sea, flow through Fram Strait or return south along Greenland to Denmark Strait. One of the main differences between MOM and POP is that more than half of the NIIC watermass leaves through Denmark Strait in MOM, where most particles take the long way around (along the DSI and DSm paths). In POP, only 23% leaves through

Denmark Strait, which may be explained by the weak EGC in POP and the long residence time of the particles in the Greenland Basin. Using a longer advection time of the particles would possibly increase the fraction of the NIIC watermass leaving the Nordic Seas through Denmark Strait in POP.

In summary, according to the two model simulations investigated in this study the connection between the NIIC and the NIJ is either weak (in POP) or non-existent (in MOM). Furthermore, the model simulations suggest a possible connection between the NIIC and the ISOW.

#### 4.5. WATERMASS TRANSFORMATION ALONG THE PATHWAYS

## 4

In order to investigate the watermass transformation along the pathways of the NIIC water in the Nordic Seas, the temperature and salinity are traced for each particle. As an example, Figure 4.8a shows the trajectory of one of the particles that takes the DSI route in POP. Along this path, a net cooling and freshening of  $7^{\circ}\text{C}$  and 0.13 psu is seen (Figure 4.8b), leading to an increase in density of  $0.68\text{ kg/m}^3$ . The transformation predominantly takes place at times when the particle is located inside the mixed layer (shaded periods in Figures 4.8b and 4.8c). Note that the magnitude of the cooling that takes place is not necessarily related to the depth of the mixed layer, neither to the strength of the heat flux at the surface. As seen in Figure 4.8b between location 1 and 2, the particle changes its thermohaline properties to a warmer and saltier watermass, while traveling to a location with a deeper mixed layer and a stronger atmospheric cooling. Most likely, the warming and increase in salinity is a result of mixing with Atlantic Waters that enter the Nordic Seas east of Iceland. Two periods of strong cooling along the path of the particle can be distinguished. The cooling that takes place north of Iceland (upstream of number 1 in Figure 4.8a) at the start of the trajectory coincides with a reduction in salinity. This could indicate another mixing process with cold and fresh waters from the north. The second cooling event takes place when the particle is south of Svalbard (between location 6 and 7 in Figure 4.8a). During this cooling event, the salinity change is rather small and the particle is close to the sea surface, indicating that the reduction in temperature is most likely due to atmospheric cooling.

Note that not only this particle, but all particles change their density predominantly when they are located within the mixed layer. This is because diapycnal mixing below the mixed layer is small (e.g. *Ledwell et al.*, 1993). In the model simulations, diapycnal mixing originates from the vertical background diffusion and in case of steep fronts from horizontal biharmonic diffusion. In addition to diapycnal mixing, there can be isopycnal mixing (mixing of temperature and salinity without a change in density) either by the explicitly resolved eddies or by horizontal diffusion. However, the effect of isopycnal mixing on temperature and salinity is much smaller than the diapycnal and diabatic water mass transformation within the ocean mixed layers. This is evident in Figure 4.8b-c from the much smaller temperature and salinity changes when the particle is below the mixed layer.

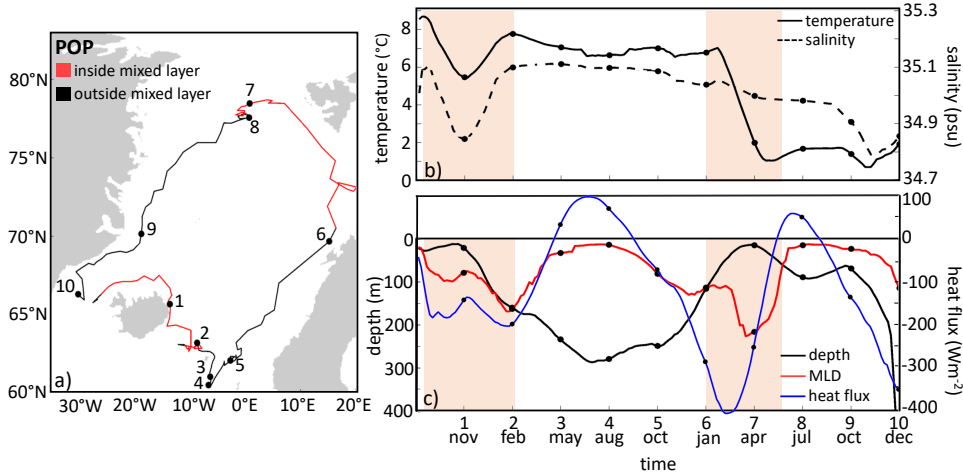


Figure 4.8: (a) Example trajectory of a DSI particle in POP that is part of the DSOW. The line is red where the particle is traveling inside the mixed layer, the line is black outside the mixed layer. (b) Temperature (solid black line, left axis) and salinity (dashed black line, right axis) along the path of the particle trajectory shown in panel a. (c) Depth of the particle (in black), the mixed layer depth along the trajectory (in red) and the heat flux at the sea surface along the trajectory (in blue, negative means cooling). The shaded orange periods in (b-c) indicate when the particle is in the mixed layer. The numbers along the time axis of panel b and c correspond to the numbers in panel a, showing the particle location at the specified time.

#### 4.5.1. CONTRIBUTION OF THE NIIC WATER TO OVERFLOW WATERS

The investigation of this single particle pathway already elucidates many aspects of density changes that can occur in the Nordic Seas. To analyze the watermass transformation of the NIIC and its contribution to the overflows, all particles need to be taken into account. The change in temperature and salinity of the particles is visualized in the T-S diagrams in Figures 4.9a and 4.9b, where T-S properties of the particles that enter the Nordic Seas (in green) are compared to the T-S properties of the particles that exit the Nordic Seas at either Denmark Strait, crossing the Iceland-Scotland Ridge, into the Barents Sea or through Fram Strait (in purple). The temperature and salinity of the particles is gridded on a  $\Delta T = 0.1^\circ\text{C}$  and  $\Delta S = 0.05$  psu temperature-salinity grid. In both models a clear shift to lower temperatures is seen ( $\Delta T \sim 4\text{--}7^\circ\text{C}$ ) and little change in salinity.

Using the thermohaline properties of the particles, an estimate can be made to what extent the NIIC watermass contributes to the overflow waters in both models. Figures 4.9c and 4.9d show the mean volume transport of all the water crossing Denmark Strait as a function of temperature and salinity for MOM and POP, derived from the Eulerian mean velocity fields. The thick density contour shows the minimum density of the overflows defined in section 4.3.3. The same contour is also shown in Figures 4.9a and 4.9b. Using this threshold density, 27% (14.7%) of the water transported by the NIIC reaches a density that is larger than  $27.8\text{ kg/m}^3$  ( $28.0\text{ kg/m}^3$ ) when leaving the Nordic Seas in MOM (POP).

To investigate along which paths this dense water is transported, the outflow temperature and salinity of the particles is split over five T-S categories, indicated by the

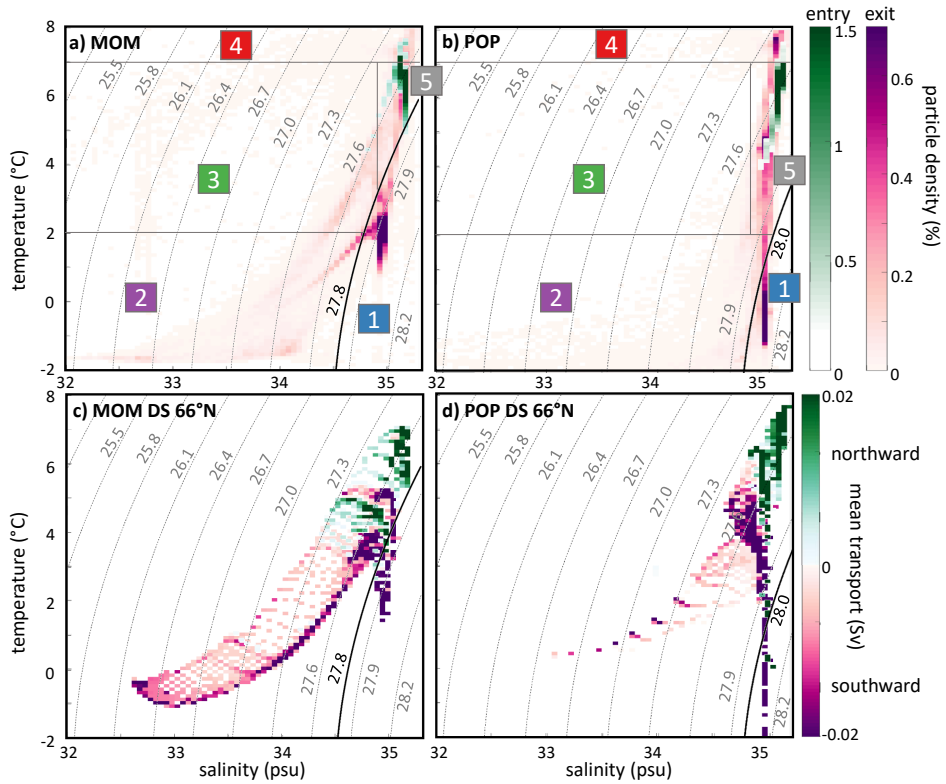


Figure 4.9: (a-b) T-S diagrams of the thermohaline properties of the particles when entering the Nordic Seas (in green) and exiting the Nordic Seas at any of the exit locations (in purple) for (a) MOM and (b) POP. The transport weighted particle density is shown per  $\Delta T = 0.1^\circ\text{C}$  and  $\Delta S = 0.05$  psu interval. The horizontal and vertical gray lines separate the T-S categories used in Figure 4.10. (c-d) Mean volume transport from the Eulerian velocity fields at Denmark Strait ( $66^\circ\text{N}$ ) as a function of temperature and salinity in MOM (left) and POP (right). Transport into the Nordic Seas is shown in green and transport out of the Nordic Seas in purple. In all panels, contours are density ( $\text{kg}/\text{m}^3$ ), where the thick black line indicates the density threshold for the overflow waters (see section 4.3.3) in MOM respectively POP.

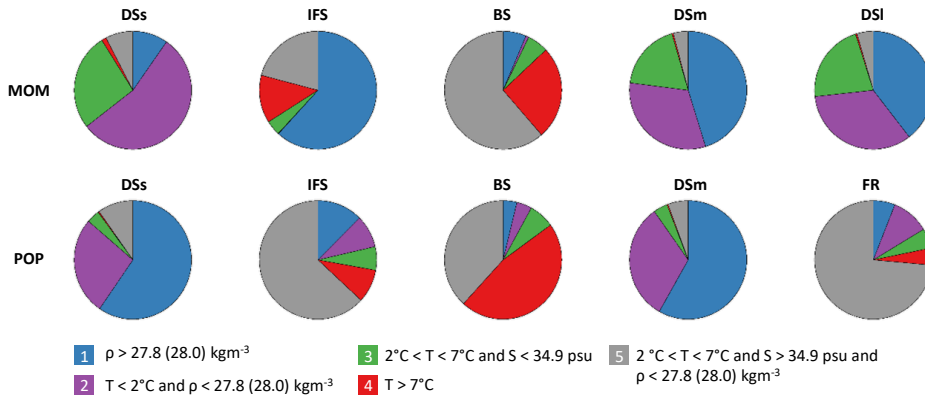


Figure 4.10: Fraction of particles per pathway leaving the Nordic Seas within specific T-S categories, described in Figures 4.9a-b. Only the paths that carry more than 5% of the NIIC water are shown.

gray lines in Figures 4.9a-b. The categories are based on whether the density along the pathway increased sufficiently to resemble the overflow (category 1), whether both temperature and salinity decreased (category 2), whether mainly the salinity decreased (category 3), whether the temperature increased (category 4), or whether the thermohaline properties of the particles remained roughly similar (category 5).

Applying this categorization process to each pathway (Figure 4.10) directly reveals along which pathways the dense water that eventually contributes to the overflows is transported (blue color in Figure 4.10). In MOM, the NIIC water that contributes to DSOW is transported mainly via the DSI and DS<sub>m</sub> path (18.2%, 0.20 Sv). In POP, 10.8% (0.19 Sv) of the NIIC water reaches Denmark Strait as DSOW, which is mainly transported via the DS<sub>s</sub> pathway and partly by the DS<sub>m</sub> path.

The NIIC watermass is also connected to the overflow between Iceland and Scotland (ISOW) in both models via the IFS path, and this connection is stronger in MOM than in POP (7.8%, 0.09Sv in MOM and 2.1%, 0.04Sv in POP). In MOM, the majority of the IFS particles are transformed to the overflow density (blue color Figure 4.10), whereas in POP most particles have T-S properties that are similar to those at entering the Nordic Seas (gray color Figure 4.10). However, just before entering the Iceland-Faroe Channel (at the transect shown in Figures 4.7c-d), the T-S properties of the particles in POP are very similar to those in MOM (not shown). A possible explanation for the sudden decrease in density is the slightly deeper mixed layer depths in the Iceland-Faroe Channel found in POP, making the IFS watermass more prone to mixing with the warm and salty Atlantic Water layer. This is linked to the fact that the IFS particles in MOM leave mainly through the deep channel east of the Faroe Islands, whereas the IFS particles in POP leave west of the Faroe Islands (section 4.4). In both models the isopycnal that serves as the upper threshold for the overflow waters is located at ~500m depth at the Iceland-Scotland Ridge. As the channel between Iceland and the Faroe Islands is only 500m deep, most of

the ISOW has to leave east of the Faroe Islands, where the channel is 1100m deep.

Most of the particles that flow into the Barents Sea show either similar temperatures or an increase in temperature with respect to their original properties when flowing into the Nordic Seas. As a result, both simulations show only few particles with an overflow density entering the Barents Sea and the Arctic Ocean (1% in MOM and 1.8% in POP). It is likely that a part of the watermass that enters the Barents Sea and the Arctic Ocean will transform to denser waters further north, but this is outside the scope of this study.

#### 4.5.2. LOCATION OF WATERMASS TRANSFORMATIONS

To shed more light on the differences and similarities between the two model simulations regarding the watermass transformation along the paths, the location of the thermohaline changes along the pathways is investigated (Figure 4.11). The rate of change of temperature and salinity is determined and spatially binned on a  $0.5^\circ \times 0.5^\circ$  latitude-longitude grid. Next, this rate of change is multiplied by the residence time of the particles at each gridbox, to obtain the total change in temperature and salinity that the particles undergo at each location. Then, the results are averaged at every gridbox when the particle number in the gridbox exceeds 100 particles.

The watermass transformation along the DSs path displays the largest difference between the two simulations. In MOM, the majority of the particles change their thermohaline properties to a fresher watermass (purple area Figure 4.10), whereas in POP a strong transformation to a cold and salty watermass takes place (blue area Figure 4.10). Figures 4.11a-b show the temperature change for the particles that leave the Nordic Seas as DSOW. Both simulations show strong cooling. In MOM, this cooling is confined to the region just north of Iceland, whereas in POP the water flowing along the DSs path cools over the entire area between Iceland and Greenland.

The differences between both model results become more apparent in Figures 4.11c-d, where the salinity change is shown for the particles that change their thermohaline properties to a colder and fresher watermass (T-S category 2, purple area Figure 4.10). Where in MOM the strongest cooling is found directly at the release location of the particles ( $66^\circ\text{N}$ , Figure 4.11a), the strongest freshening takes place further downstream ( $\sim 68^\circ\text{N}$ , Figure 4.11c). In POP, the reduction in salinity is significantly smaller and takes place closer to the Greenland coast (Figure 4.11d). The total density change along the DSs pathway (Figures 4.11e-f) indicates that the decrease in salinity in MOM outweighs the temperature decrease and most of the DSs particles become lighter along this path. In POP, the salinity decrease is small and most of the particles become denser along the DSs path (Figure 4.11f). This explains why the DSs particles are found at the surface in MOM and at depth in POP, when flowing south through Denmark Strait (Figures 4.7a-b).

The changes seen in the particles' properties along the DSs path can be related to the location of the sea ice (Figures 4.3a-b). As the maximum sea-ice edge extends to the center of Denmark Strait in MOM, cooling by the atmosphere is confined to the region close to Iceland as seen in Figure 4.11a. In POP, the region between Iceland and Greenland is ice free year-round, and atmospheric cooling is not blocked by sea ice. Further, it is likely that mixing takes place with the cold and fresh waters that flow south along the Greenland coast. In MOM, the salinity gradient in the Denmark Strait region is much larger than in POP (see Figures 4.2e-f). The fresher surface waters seen in MOM may be

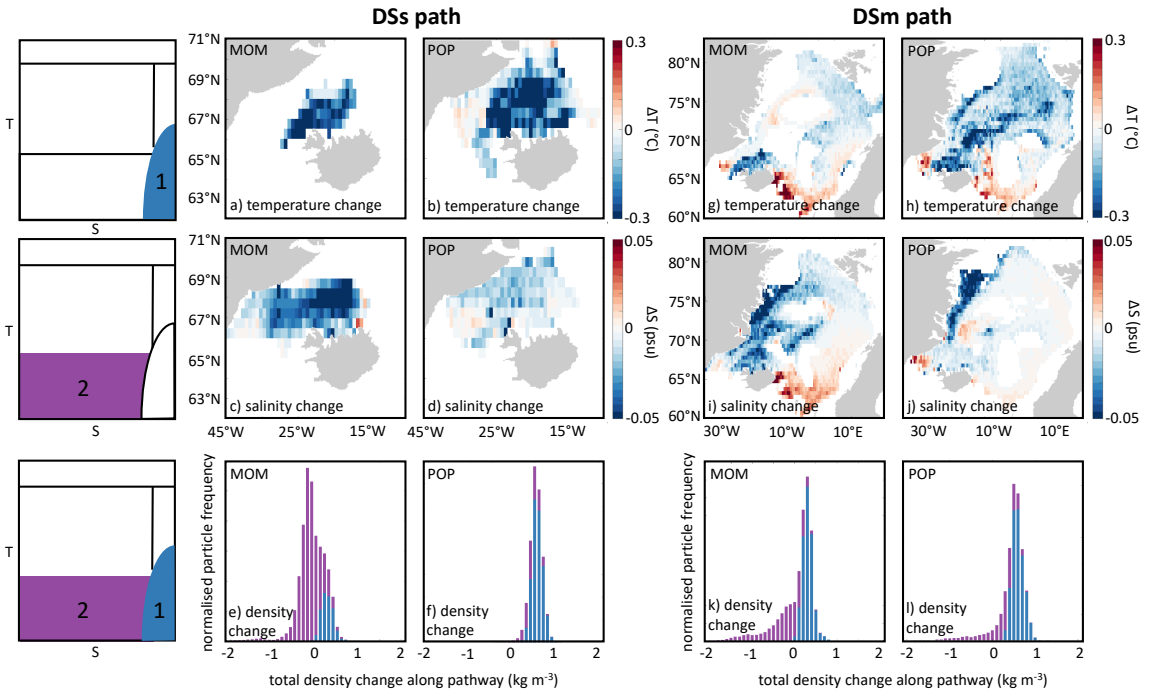


Figure 4.11: Temperature change per  $0.5 \times 0.5^\circ$  lon-lat gridbox (a-b, g-h), salinity change per  $0.5 \times 0.5^\circ$  lon-lat gridbox (c-d, i-j) and total density change (e-f, k-l) along the DSs path (a-f) and the DSm path (g-l). The upper row shows the temperature change of the particles that have a density larger than  $27.8$  ( $28.0$ )  $\text{kg}/\text{m}^3$  at leaving the Nordic Seas (T-S category 1, see Figures 4.9 and 4.10). The middle row shows the salinity change of the particles that have temperature and density properties smaller than respectively  $2^\circ\text{C}$  and  $27.8$  ( $28.0$ )  $\text{kg}/\text{m}^3$  at leaving the Nordic Seas (T-S category 2, see Figures 4.9 and 4.10). The third row shows the distribution of the total density change of each particle along the pathway (positive indicates a density increase), with the particles that connect to the DSOW (T-S category 1) in blue and the particles that leave the Nordic Seas with the T-S properties of T-S category 2 in purple.

a result of ice melt, but also due to the different surface freshwater boundary conditions. Therefore, similar mixing will lead to a stronger freshening in MOM than in POP.

The pathway along which the total density change is similar in both simulations is the DS<sub>m</sub> path (Figures 4.10 and 4.11k-l). However, the locations where the thermohaline changes take place are different. In MOM, the strongest cooling is found just north of Iceland, similar to the DS<sub>s</sub> path (Figure 4.11g), while in POP, cooling is also seen along the shelfbreak of Greenland and in the interior of the Nordic Seas (Figure 4.11h). Both models show freshening along the Greenland coast, where the water mixes with the Polar Water of the EGC (Figures 4.11i-j). In MOM, freshening is also seen just southeast of the Greenland Basin.

Both MOM and POP display local maxima of watermass transformation in the interior of the Nordic Seas (cooling in POP and freshening in MOM, Figures 4.11h-i). As seen in Figures 4.2h-i, the flow speed is significantly lower in the interior of the Nordic Seas than at the boundaries and therefore the local maxima seen in Figures 4.11h-i are a result of the larger residence time of the particles in these areas. Similar to the DS<sub>s</sub> path, the atmospheric cooling is limited by the sea-ice extent over the western side of the Nordic Seas in MOM as seen in Figure 4.11g and the freshening southwest of the Greenland Basin is likely a result of ice melt. The model simulations show an increase in both temperature and salinity southeast of Iceland. This transformation is a result of mixing with the Atlantic Water that flows into the Nordic Seas east of Iceland (Figure 4.1). The location of watermass transformation along the other pathways was investigated as well, but did not differ substantially from the watermass transformation along the DS<sub>m</sub> path shown in Figure 4.11g-j.

In summary, both simulations show a similar contribution of the NIIC to the DSOW of 0.2 Sv. However, the pathways along which the transformation takes place differ. This is a result of the differences in sea-ice cover in the Nordic Seas, and likely due to the different freshwater boundary conditions of the model simulations. As hypothesized in section 4.4, investigation of the thermohaline properties of the particles elucidated a weak connection between the NIIC and the ISOW.

## 4.6. DISCUSSION AND CONCLUSIONS

In this chapter Lagrangian particles have been used to investigate the pathways and the watermass transformation of the North Icelandic Irminger Current (NIIC) in the Nordic Seas in two ocean models. The volume of the NIIC water along each pathway and the contribution of the NIIC watermass to Denmark Strait Overflow Water (DSOW) and Iceland Scotland Overflow Water (ISOW) have been quantified. Further, the locations of the watermass transformation have been studied to investigate their relation to the location of the convection regions within the Nordic Seas.

Based on observations, some studies propose a strong connection between the NIIC and the DSOW, where the NIIC watermass is transformed northwest of the Iceland gyre and flows back into the Atlantic Ocean via the North Icelandic Jet (NIJ) through Denmark Strait (*Våge et al.*, 2011; *Pickart et al.*, 2017). The indication that both currents carry a similar volume transport and the assumption that the EIC does not contain a large part of the NIIC watermass, led to a suggested one-to-one connection between the NIIC and the NIJ (*e.g.* *Pickart et al.*, 2017). The results from this study provide a different view

than has been deduced from the observations. The models suggest that the inflowing NIIC watermass is divided over several pathways in the Nordic Seas, and that only 13% of the NIIC watermass flows until Kolbeinsey Ridge to follow the short suggested loop. The region north of Iceland seems to play a crucial role in diversifying these pathways. The connection from the NIIC to DSOW via the NIJ has only been found in POP, since in MOM strong freshening takes place near the surface.

As was shown in Figure 4.7, the particles that follow the short DSs path originate from the upper 100m of the NIIC, whereas the deeper part of the NIIC flows farther east along Iceland. This could explain why *Valdimarsson and Malmberg* (1999) concluded that the DSs path was the main route for the NIIC, since this was the only path they could observe using surface drifters. *Jónsson* (1992) observed the NIIC watermass at the northeast corner of Iceland, slightly deeper in the watercolumn. In light of the results of our study, it is possible that he measured the fraction of the NIIC watermass that eventually leaves between Iceland and Scotland (the IFS path). Both models used in this study show a very strong watermass transformation north of Iceland. Therefore it is possible that observations underestimate the Atlantic Water originating from the NIIC east of Iceland. Also, the part of the NIIC water that travels offshore of Iceland is indistinguishable from the EIC. Therefore, this study fits well with previous work that concluded that the EGC is most likely not the only source for the EIC (e.g. *Logemann et al.*, 2013).

The results of this study strongly indicate that the DSs path is topographically controlled and that the fraction of the NIIC water following this path is set by the vertical structure of the current. Our results indicate that the path itself is not sensitive to sea-ice cover and atmospheric conditions and hence it is likely that similar conclusions can be drawn when repeating this research in models with interannually varying forcing. Further, as the instability of the NIIC is only slightly underestimated in the model simulations presented in this study, it is not expected that a fully eddy-resolving simulation would show a significantly stronger connection between the NIIC and the NIJ.

Both models display only 0.2 Sv NIIC contribution to the Denmark Strait Overflow Water, although the paths along which this water is transported back to Denmark Strait differ. This means that in these models the NIIC can not be the main source for the NIJ watermass. This is in line with the Lagrangian analysis conducted previously by *Behrens et al.* (2017), who found that only a small part of the DSOW originated from the NIIC. Note that as their study concerned only backtracking of the DSOW, no statement could be made on what fraction of the NIIC watermass contributes to the overflow as is done in this study.

Interestingly, both MOM and POP show a small contribution of the NIIC watermass to the ISOW of 7.8% respectively 2.1%, which is a weak connection that might be hard to detect by observations (e.g. *Stefánnson*, 1962; *Perkins et al.*, 1998). Part of the Modified East Icelandic Water originates from the North Icelandic Shelf and is formed during winter convection and is modified due to strong mixing with surrounding watermasses (*Stefánnson*, 1962; *Read and Pollard*, 1992). It is likely that the IFS path found in the models resembles this contribution.

The model simulations used in this study show agreement on both the pathways of the NIIC watermass and the contribution to the overflows, regardless of the large differences in the sea-ice cover, the hydrography and the circulation patterns between the

simulations. This gives confidence that the conclusions drawn from the simulations regarding the NIIC pathways are not a model artifact, but apply to actual processes in the Nordic Seas.

The models do show some differences regarding the pathways along which DSOW is created. The agreement between the models in the NIIC contribution to DSOW of 0.2 Sv could therefore be a pure coincidence. In MOM, a mean freshening is seen along the DSs path and dense water is only transported to Denmark Strait along the deeper part of the EGC by the DSI and DSm paths. In POP, the EGC is weak and is only reached by a limited number of particles (2.2%). However, since the DSs path in POP does not display a strong decrease in salinity, this pathway serves as the main connection between the NIIC and the DSOW in this model.

The models have a very different approach regarding the sea ice, which might explain why the watermass transformation to DSOW is different. The sea-ice cover in MOM between Greenland and Iceland is substantial and in POP non-existent (see black lines Figures 4.2b and 4.2c). Therefore, the strong freshening seen in MOM along the DSs path could be a result of sea-ice melt northwest of Iceland. Also the strength of the EGC seems to be affected by the location of the sea ice. It could be that a reduction in the sea ice in MOM would lead to a smaller decrease in salinity along the DSs path, leading to a larger contribution to DSOW. At the same time, the reduction in sea ice might lead to a stronger cooling of the EGC by the atmosphere which could resolve into a reduction of this current as is seen in POP. These relations are hypothetical and require further research outside the scope of this chapter. What this study does show is that while the DSOW transport might be well captured by ocean models, the path of the dense water to Denmark Strait is highly sensitive to the hydrographic properties of the modeled ocean circulation.

In conclusion, this chapter has shown that the connection between the North Icelandic Irminger Current and the Denmark Strait Overflow Water in MOM and POP is not as strong as proposed by observations. Furthermore, this chapter confirms that the NIIC is connected to the Iceland Scotland Overflow Water as well. The watermass transformations taking place north of Iceland and the vertical structure of the NIIC play a crucial role in setting the future pathways of the NIIC watermass. The pathways along which the dense water is formed are different between the two models, highlighting the sensitivity to the model's representation of the hydrography and circulation in the Nordic Seas.

# 5

## DISCUSSION AND OUTLOOK

In summary, this thesis has provided new insights into the watermass transformation of Atlantic Water in the Nordic Seas. As such, it has improved our understanding of Nordic Seas dynamics and has elucidated the importance of asymmetries in the Nordic Seas for the dense water overflows, and hence the Atlantic Meridional Overturning Circulation. In this thesis, it has been shown that conceptual models are powerful tools to study asymmetries and eddy heat fluxes in a marginal sea such as the Nordic Seas. Moreover, Lagrangian methods have been shown to be an essential tool to examine flow connectivity and to provide insight into where and how watermass transformation takes place. In this final chapter, a short discussion is provided on each chapter (section 5.1-5.3) and on the implications of the various findings presented in this thesis (section 5.4). Finally, recommendations for further research are provided in section 5.5.

### 5.1. ASYMMETRY IN A TWO-BASIN MARGINAL SEA

*"How are the dynamics, circulation and mean hydrography controlled in a two-basin marginal sea subject to buoyancy loss such as the Nordic Seas?"*

One of the key characteristics of the Nordic Seas is the hydrographic asymmetry between east and west. This asymmetry is the result of the difference in dynamics between the Lofoten Basin and the Greenland Basin. The Lofoten Basin is in a so-called eddy-dominated regime. Here, the increased lateral eddy heat flux from the Norwegian Atlantic Slope Current near the Lofoten Islands can efficiently compensate for the surface heat loss to the atmosphere and as a result variations in atmospheric buoyancy forcing play a less dominant role. In the Greenland Basin, the East Greenland Current is not as unstable, and therefore the basin is more sensitive to changes in atmospheric buoyancy forcing. To investigate how these dynamical differences impact the hydrography and circulation in the Nordic Seas, a conceptual model was derived in **chapter 2**.

So far, conceptual models of a one-basin domain have proven valuable for understanding the buoyancy budget in a marginal sea like the Labrador Sea. Here, a framework is developed by applying a heat and volume budget to two basins, in which a front

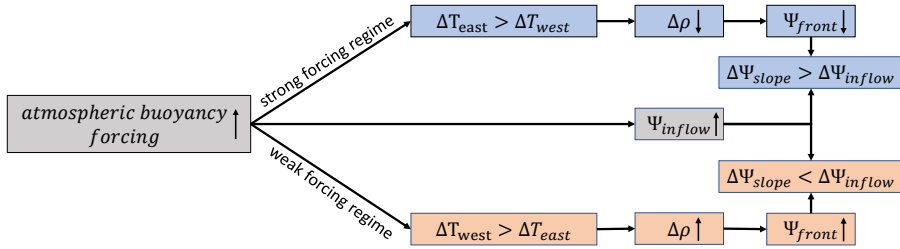


Figure 5.1: Schematic of the response of the temperature difference between the eastern and western basins ( $\Delta\rho$ ) and the transport of the inflow ( $\Psi_{inflow}$ ), slope current ( $\Psi_{slope}$ ) and front current ( $\Psi_{front}$ ) to an increase in atmospheric buoyancy forcing in a two-basin marginal sea. The blue (orange) boxes show the response of the marginal sea when the atmospheric forcing is relatively strong (weak).

## 5

current is added and the temperature of the mean flow decreases linearly. Results from this two-basin conceptual model show much better agreement with the characteristics of the Nordic Seas than the one-basin framework. The results presented in **chapter 2** elucidate the inter-dependence of the hydrography and circulation in the Lofoten Basin and the Greenland Basin as they are connected via the front current and the slope current. Not surprising, the hydrography of the Greenland Basin depends on the dynamics of the upstream Lofoten Basin. Counter-intuitively, the two-basin framework indicates that the opposite is true as well. As the strength of the front is set by the temperature difference between the two basins, the lateral eddy heat flux from the front to the eastern interior (the Lofoten Basin) as well as the strength of the slope current indirectly depend on the hydrography of the western basin interior (the Greenland Basin).

Furthermore, we show that the dynamical differences between east and west have a profound impact on the sensitivity of the marginal sea to changes in atmospheric buoyancy forcing (see schematic 5.1). The difference in eddy efficiency between east and west leads to a non-uniform response of the interior basin temperature. When the atmospheric buoyancy forcing is relatively weak (orange boxes in Figure 5.1), a small increase in forcing will lead to a stronger cooling of the interior basin in the west than in the east, as the efficient eddy heat flux in the east can compensate most of the heat loss. When the atmospheric forcing is relatively strong (blue boxes in Figure 5.1), a small increase in forcing will lead to a stronger cooling of the interior basin in the east instead. This is because the surface heat flux over the western basin is minimal as the ocean temperature is already similar to the atmospheric temperature, while the eddy heat flux in the east is no longer sufficient to compensate the additional atmospheric cooling.

It is not only the hydrographic properties, but also the circulation that responds in a non-linear way to changes in atmospheric buoyancy forcing. When assuming a buoyancy driven flow, increased cooling over a marginal sea leads to a stronger inflow into the basin (gray box in Figure 5.1). The inflow separates into a slope current and a front current. Therefore, the transport along the slope current ( $\Psi_{slope}$  in Figure 5.1) does not only depend on the total heat loss to the atmosphere, but also on the temperature difference between the two interior basins. The latter is important for the strength of the

front current ( $\Psi_{front}$  in Figure 5.1). As discussed in the previous paragraph, when the atmospheric forcing is weak, small changes in forcing lead to an increased temperature difference between the eastern and western basins and therefore to a stronger front current. The opposite is true when the atmospheric forcing is strong. In order to predict the response of a two-basin marginal sea to changes in atmospheric buoyancy forcing, it is therefore essential to know whether the system is in a weak-forcing or in a strong-forcing regime.

## 5.2. THE NORWEGIAN ATLANTIC FRONT CURRENT

*"How does the front current along the Mohn- and Knipovich Ridges affect the pathways and watermass transformation of Atlantic Water in the Nordic Seas?"*

The results from the two-basin conceptual framework presented in **chapter 2** highlight the important role of the front current in determining the heat and volume budget in the Nordic Seas. Observations have provided estimates of the strength of the front current and of the lateral heat fluxes from the front to the surroundings. However, little was known about the connection between the flow along the Mohn Ridge and the Knipovich Ridge and whether the transformation of the Atlantic Water along the front would be different from the transformation along other pathways. In **chapter 3** the connectivity of the frontal flow along the Mohn and Knipovich Ridges and its watermass transformation was studied in detail using observations and two model simulations.

The analyzed trajectories of surface drifters, ARGO floats and numerical particles in the regional model configuration indicate that the connection between the front current along the Mohn Ridge and the front current along the Knipovich Ridge is much weaker than implied by general schematics (see Figure 1.1). Of the observational drifters and floats near the mid-ocean ridges, only 8% followed the frontal pathway to the north. In corroboration with the observational data set, the trajectories from the realistic numerical simulations elucidate the various possible pathways emanating from the front along the Mohn Ridge; towards the slope current, along the eastern or western flank of the Knipovich Ridge, and across the ridge following the Greenland Fracture Zone. Substantial flow exchange between the front current and the slope current was seen, with a cross-basin exchange region following the 2500 m isobath at 72°N. Further north, the observed trajectories indicated multiple crossings from the slope current to the front current and vice versa, most likely steered by eddies.

Apart from the various pathways along the mid-ocean ridges, cross-ridge exchange was observed connecting the Lofoten and the Greenland Basins. Investigating the hydrographic changes along the various trajectories in the realistic numerical simulation in addition to an idealized simulation, we showed that the freshest and coldest watermasses are formed along the front, due to the frontal current instability. The results indicate that watermass transformation of Atlantic Water depends on the pathway that it takes through the basin.

### 5.3. THE NORTH ICELANDIC IRMINGER CURRENT

*"Which pathways does the Atlantic Water that enters the Nordic Seas west of Iceland take and where is this watermass transformed?"*

The dependence of the Atlantic watermass transformation on its pathways through the Nordic Seas is further investigated in **chapter 4**, but now for the pathways of the Atlantic Water that enters the Nordic Seas through Denmark Strait via the North Icelandic Irminger Current (NIIC). Based on hydrographic transects, it has previously been hypothesized that the NIIC transforms on the Icelandic Plateau to form the recently discovered North Icelandic Jet (NIJ), and therefore provides the densest watermasses to the Denmark Strait Overflow Water (DSOW). In **chapter 4** this hypothesis is tested by tracing the NIIC watermass in two model simulations; MOM and POP. The results indicate that only a small part of the NIIC is connected to the DSOW and only in one of the two models does this connection occur via the NIJ. So, according to these model simulations the NIIC does not form a one-to-one connection with the NIJ.

Results presented in **chapter 4** indicate that the fate of the NIIC watermass is determined by its vertical distribution at the inflow and by watermass transformation processes north of Iceland. The surface layer of the NIIC inflow is most likely to follow a short loop through the Icelandic Plateau that eventually exits through Denmark Strait. North of Iceland, transformation processes separate the remaining NIIC watermass in a deep (dense) and shallow branch, where the former contributes to the Iceland Scotland Overflow Water and the latter follows the branches of the Norwegian Atlantic Current through the eastern basin of the Nordic Seas.

The extensive model validation presented in **chapter 4** highlights the differences between the two model simulations. These differences most likely arise from a different sea-ice configuration and surface restoring used in these simulations. Although both models compare differently to observations, they are still valuable. By careful analysis one can hypothesize how these model differences are related to the NIIC pathways and watermass transformation. There are two NIIC pathways that can be linked to the sea-ice extent in each model. We hypothesize that the connection from the NIIC to the NIJ is missing in MOM due to the fresh bias of MOM at the surface in this region, therefore prohibiting the upper layer of the NIIC to become dense. Furthermore, the East Greenland Current is much stronger in MOM than in POP. This is likely related to the fact that the East Greenland Current is directly in contact with the atmosphere in POP, but isolated from the atmosphere by sea ice in MOM.

### 5.4. OVERARCHING CONCLUSIONS AND DISCUSSION

This thesis explored the circulation in the Nordic Seas, the importance of the hydrographic asymmetry in the Nordic Seas and the watermass transformation of Atlantic Water. Here, the implications of these findings are discussed.

#### 5.4.1. REVISED CIRCULATION SCHEME OF THE NORDIC SEAS

**Chapter 3** and **chapter 4** investigated pathways of Atlantic Water through the Nordic Seas using a Lagrangian approach. Doing so, knowledge on the circulation in the Nordic

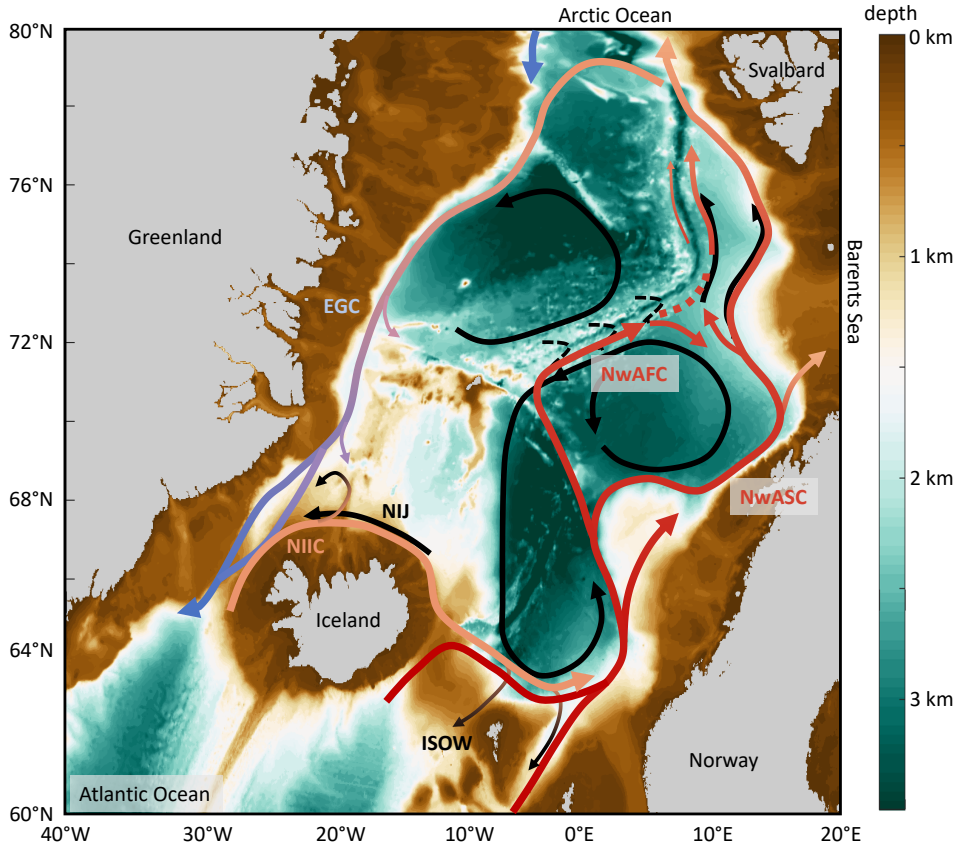


Figure 5.2: Revised circulation scheme of the Nordic Seas. The inflow of warm and saline Atlantic Water and the subsequent pathways are colored red and orange (North Icelandic Irminger Current, NIIC, Norwegian Atlantic Slope Current, NwASC, Norwegian Atlantic Front Current, NwAFC). The East Greenland Current (EGC) is represented by the blue path. In black, the circulation at mid-depth is schematized, as derived from the results presented in **chapter 3** and **chapter 4** (North Icelandic Jet, NIJ, Iceland Scotland Overflow Water, ISOW). Dashed lines indicate weak connections between different flow branches.

Seas has been advanced as schematized in Figure 5.2. The main differences with the schematic overview provided in the introduction (Figure 1.1) are the pathway of the NIIC and the pathway of the NwAFC. In the revised circulation map, the main pathway of the NIIC continues to the east to join the NwAC, instead of terminating north of Iceland. The connection from the NIIC to the DSOW and ISOW is denoted by small arrows leaving this main branch. The continuation of the NwAFC from the Mohn Ridge northward is schematized in more detail as well, indicating the cross-basin exchange region at 72°N.

These results were obtained by applying a Lagrangian approach and using a numerical simulation, highlighting the value of Lagrangian simulations. As discussed in **chapter 3**, previous schematics of the two-branch structure of the NwAC were based on only

7 observed trajectories along the Mohn and Knipovich Ridges. It is important to understand how to interpret Lagrangian data when it is used to derive Eulerian properties of a region. Deriving mean velocities from observed float trajectories can provide a valuable addition to observations taken at fixed locations. However, once these gridded products are derived, all information about connectivity is lost and care should be taken regarding the statistical significance of the results when the number of floats is limited.

However, it is of utmost importance to know how the different flow branches are connected, if one wants to understand how anomalies propagate through basins. The revised circulation scheme in Fig. 5.2 therefore shows a combination of both the Eulerian-mean circulation as the connections between different branches due to Lagrangian processes like eddy advection. Both the observed trajectories as well as the numerical trajectories analyzed in **chapter 3** and **chapter 4** show significant variability. Regions with strong eddy activity could delay anomalies from propagating further north or south and even diminish correlations between different regions. This is not only true for the Nordic Seas, the entire AMOC is known for regions where the main transport is not carried by the mean flow, but by eddies instead (*Bower et al.*, 2019). Therefore, Lagrangian studies are a powerful means with which to address flow connectivity.

5

#### 5.4.2. THE IMPORTANCE OF THE HYDROGRAPHIC ASYMMETRY

The variability in the hydrographic asymmetry of the Nordic Seas plays an important role for the circulation. Results presented in **chapter 2** conclude that due to the different dynamics in the eastern and western basins, the basins will respond differently to the same change in forcing. It is very likely that the density gradient across the Mohn and Knipovich Ridges is not constant, as the atmospheric forcing across the Nordic Seas is not uniform and the hydrography in the Lofoten and Greenland Basins is sensitive to anomalies in the Atlantic Ocean and the Arctic Ocean. On decadal timescales, this variation in the density gradient across the mid-ocean ridge can impact the strength of the front current. If the warming across the Arctic region continues as predicted, both the density gradient across the mid-ocean ridge and the baroclinic component of the front current are expected to weaken. Our results suggest that this variability will also be reflected in the strength of the slope current and in the overall inflow into the Nordic Seas as schematized in Figure 5.1.

The conclusions drawn on the importance of the hydrographic asymmetry for the circulation are not only based on the conceptual framework and idealized model simulation, but also on the more realistic MOM and POP simulations analyzed in **chapter 4**. A cold bias of the Lofoten Basin was seen in the POP simulation, whereas in MOM the basin temperature compared better to observations. As the wind forcing in these simulations was identical, the resulting southward (instead of northward) flow along the Mohn Ridge in POP can be attributed to the anomalously weak density gradient across the ridge. This highlights that in order to gain further insight in Atlantic Water pathways in the Nordic Seas, it is of utmost importance to correctly capture the hydrography and dynamics of this region.

### 5.4.3. THE IMPORTANCE OF THE FRONT CURRENT INSTABILITY

As discussed in the previous section, the hydrographic asymmetry impacts the front current strength, and therefore also the instability of the front current along the mid-ocean ridge. This has several implications for the watermass transformation of Atlantic Water that takes the frontal pathway. The particle trajectories from the idealized simulation in **chapter 3** elucidate how water transforms when transported by eddies from the front to the west. This process is very similar to the process discussed by *Brüggemann and Katsman* (2019). When a water parcel is captured by the instability of the front current, its propagation to the north is delayed. Therefore, the water will be exposed to the atmospheric cooling longer (while it is in the mixed layer). Through mixing with the cold and fresh surroundings this water parcel can also experience freshening. Most of these particles stay close to the front current, and return to their path northward within the front current; notably, now within a different density class deeper in the water column than before.

The modeled trajectories analyzed in **chapter 3** show that a stronger cooling and freshening takes place along the front current if Atlantic Water is steered towards the western basin by meandering of the flow or by eddies as described above. This could be one of the reasons why multiple fronts have been observed along the Knipovich Ridge (e.g. *van Aken et al.*, 1995). The water that transforms along a continuous pathway by gradual atmospheric cooling will obtain different hydrographic properties than water that is fluxed away from the mean flow towards a colder and fresher basin before returning to the main front current. Furthermore, the trajectories in the realistic simulation MOM in **chapter 4** indicate cooling and freshening along the frontal pathway as well (the DS<sub>m</sub> path).

The instability of the front current is different from the instability of the slope current near the Lofoten Islands. There, large anticyclonic eddies are shed that travel through the entire domain of the Lofoten Basin. As far as one can tell using the idealized and realistic simulations, the instability of the front current is mainly confined to the frontal region itself. Observational trajectories and the trajectories in the realistic simulation presented in **chapter 3** show that the number of floats that do travel into the Greenland Basin is limited. Therefore, the instability of the front current might be more important for the watermass transformation of Atlantic Water in the Lofoten Basin, than for the convection processes in the Greenland Basin. However, as the total number of observed floats near the mid-ocean ridge in the Nordic Seas is limited as well, further research is needed to address these questions.

## 5.5. OUTLOOK

The Nordic Seas remain a challenging region to fully understand. It is of global interest to be able to predict how the Nordic Seas will change in the future and how this will impact the overflows and hence the Atlantic Meridional Overturning Circulation. Therefore, it is necessary to quantify environmental changes that are expected to occur regarding atmospheric warming, increased sea-ice melt and freshwater runoff. Furthermore, the impact of these changes on Nordic Seas processes, like Greenland Basin convection and overflow variability, needs to be studied. This is only possible if one understands which process is dominant where. To help reach more consensus on the sensitivity of

the Nordic Seas to a changing climate, three recommendations will be provided based on the results presented in this thesis.

The first recommendation concerns the conceptual model presented in **chapter 2**, which can provide future predictions of the changing hydrography and circulation in the Nordic Seas. So far, this theory has only been tested against idealized model simulations of the Nordic Seas. A next step would be to look for correlations between various diagnostics on decadal time scales using observations or more realistic simulations. Based on the research presented here, sensible suggestions are the density gradient across the mid-ocean ridges, transport estimates of the front and slope currents and atmospheric temperatures across the eastern and western basins of the Nordic Seas. These results would provide insight in the importance of the hydrographic asymmetry for the Nordic Seas system in relation to for example wind forcing.

The second recommendation is that research in general could benefit from a closer collaboration between people who obtain ocean observations and people who model the ocean system. The ocean modeling community uses observational data sets to validate their simulations. However, the results obtained from model studies can also be beneficial for pointing out where additional observations are needed. In case of the Nordic Seas and results presented in this thesis, an increase in the number of surface drifters and RAFOS floats near the mid-ocean ridges could help to gain better understanding of the Atlantic Water pathways through the Nordic Seas (**chapter 3**). Furthermore, if there is only a weak connection between the North Icelandic Irminger Current and the North Icelandic Jet (as discussed in **chapter 4**), the North Icelandic Jet might originate from a flow along the Jan Mayen Ridge coming from the Greenland Basin. Hydrographic transects across this ridge could provide more insight regarding this potential pathway.

Last, the watermass transformation of Atlantic Water studied in this thesis shows a dependence on the pathway the Atlantic Water takes through the Nordic Seas. Therefore, in order to fully understand the cycle from Atlantic Water inflow to dense water overflow, the distribution of Atlantic Water across these possible pathways needs to be quantified. This would require additional Lagrangian analysis in ocean models that capture the asymmetry and dynamics of the Nordic Seas as discussed in this thesis and that are eddy resolving at high latitudes. Furthermore, as the watermass transformations at different locations take place on different timescales and are controlled by different mechanisms, they will not respond equally to a changing climate. Although a challenge, improving our knowledge on Atlantic Water pathways and its transformation will help the scientific community to gain a better understanding of overflow variability and its response to anthropogenic forcing.

# BIBLIOGRAPHY

- Aagaard, K., J. Swift, and E. Carmack (1985), Thermohaline circulation in the Arctic Mediterranean seas, *Journal of Geophysical Research: Oceans*, 90(C3), 4833–4846.
- Abernathy, R., D. Ferreira, and A. Klocker (2013), Diagnostics of isopycnal mixing in a circumpolar channel, *Ocean Modelling*, 72, 1–16.
- Andersen, C., N. Koc, A. Jennings, and J. Andrews (2004), Nonuniform response of the major surface currents in the Nordic Seas to insolation forcing: implications for the Holocene climate variability, *Paleoceanography*, 19(2).
- Årthun, M., T. Eldevik, E. Viste, H. Drange, T. Furevik, H. L. Johnson, and N. S. Keenlyside (2017), Skillful prediction of northern climate provided by the ocean, *Nature communications*, 8, 15,875.
- Årthun, M., B. Bogstad, U. Daewel, N. S. Keenlyside, A. B. Sandø, C. Schrum, and G. Ottersen (2018), Climate based multi-year predictions of the Barents Sea cod stock, *PLoS one*, 13(10), e0206319.
- Behrens, E., K. Våge, B. Harden, A. Biastoch, and C. W. Böning (2017), Composition and variability of the Denmark Strait Overflow Water in a high-resolution numerical model hindcast simulation, *Journal of Geophysical Research: Oceans*, 122(4), 2830–2846.
- Blindheim, J., and S. Østerhus (2005), The Nordic Seas, main oceanographic features, *The Nordic seas: an integrated perspective*, pp. 11–37.
- Blumsack, S. L., and P. Gierasch (1972), Mars: The effects of topography on baroclinic instability, *Journal of the Atmospheric Sciences*, 29(6), 1081–1089.
- Bosse, A., and I. Fer (2019), Mean structure and seasonality of the Norwegian Atlantic Front Current along the Mohn Ridge from repeated glider transects, *Geophysical Research Letters*, 46(22), 13,170–13,179.
- Bosse, A., I. Fer, H. Søyland, and T. Rossby (2018), Atlantic water transformation along its poleward pathway across the Nordic Seas, *Journal of Geophysical Research: Oceans*, 123(9), 6428–6448.
- Bower, A., S. Lozier, A. Biastoch, K. Drouin, N. Foukal, H. Furey, M. Lankhorst, S. Rühls, and S. Zou (2019), Lagrangian views of the pathways of the Atlantic Meridional Overturning Circulation, *Journal of Geophysical Research: Oceans*, 124(8), 5313–5335.
- Bower, A. S. (1991), A simple kinematic mechanism for mixing fluid parcels across a meandering jet, *Journal of Physical Oceanography*, 21(1), 173–180.

- Bower, A. S., M. S. Lozier, S. F. Gary, and C. W. Böning (2009), Interior pathways of the North Atlantic meridional overturning circulation, *Nature*, 459(7244), 243.
- Bracco, A., J. Pedlosky, and R. S. Pickart (2008), Eddy formation near the west coast of Greenland, *Journal of physical oceanography*, 38(9), 1992–2002.
- Brakstad, A., K. Våge, L. Håvik, and G. Moore (2019), Water Mass Transformation in the Greenland Sea during the Period 1986–2016, *Journal of Physical Oceanography*, 49(1), 121–140.
- Bringedal, C., T. Eldevik, Ø. Skagseth, M. A. Spall, and S. Østerhus (2018), Structure and Forcing of Observed Exchanges across the Greenland–Scotland Ridge, *Journal of Climate*, 31(24), 9881–9901.
- Broomé, S., L. Chafik, and J. Nilsson (2019), Mechanisms of the time-varying sea surface height and heat content trends in the eastern Nordic Seas, *Ocean Science Discussions*, pp. 1–25, doi:10.5194/os-2019-109.
- Brüggemann, N., and C. A. Katsman (2019), Dynamics of downwelling in an eddying marginal sea: contrasting the Eulerian and the isopycnal perspective, *Journal of Physical Oceanography*, 49(11), 3017–3035.
- Buckley, M. W., and J. Marshall (2016), Observations, inferences, and mechanisms of the Atlantic Meridional Overturning Circulation: A review, *Reviews of Geophysics*, 54(1), 5–63.
- Budéus, G., and S. Ronski (2009), An integral view of the hydrographic development in the Greenland Sea over a decade, *The Open Oceanography Journal*, 3, 8–39.
- Carmack, E., and K. Aagaard (1973), On the deep water of the Greenland Sea, in *Deep Sea Research and Oceanographic Abstracts*, vol. 20, pp. 687–715, Elsevier.
- Carmack, E., I. Polyakov, L. Padman, I. Fer, E. Hunke, J. Hutchings, J. Jackson, D. Kelley, R. Kwok, C. Layton, et al. (2015), Toward quantifying the increasing role of oceanic heat in sea ice loss in the new Arctic, *Bulletin of the American Meteorological Society*, 96(12), 2079–2105.
- Cenedese, C. (2012), Downwelling in basins subject to buoyancy loss, *Journal of Physical Oceanography*, 42(11), 1817–1833.
- Chafik, L., and T. Rossby (2019), Volume, Heat, and Freshwater Divergences in the Sub-polar North Atlantic Suggest the Nordic Seas as Key to the State of the Meridional Overturning Circulation, *Geophysical Research Letters*, 46(9), 4799–4808.
- Chassignet, E. P., and D. P. Marshall (2008), Gulf Stream separation in numerical ocean models, *Geophysical Monograph Series*, 177.
- Courtois, P., X. Hu, C. Pennelly, P. Spence, and P. G. Myers (2017), Mixed layer depth calculation in deep convection regions in ocean numerical models, *Ocean Modelling*, 120, 60–78.

- Da Costa, M. V., and B. Blanke (2004), Lagrangian methods for flow climatologies and trajectory error assessment, *Ocean Modelling*, 6(3-4), 335–358.
- Dagestad, K.-F., J. Röhrs, Ø. Breivik, and B. Ådlandsvik (2018), OpenDrift v1. 0: a generic framework for trajectory modelling, *Geoscientific Model Development*, 11(4), 1405–1420.
- Danabasoglu, G., S. G. Yeager, D. Bailey, E. Behrens, M. Bentsen, D. Bi, A. Biastoch, C. Böning, A. Bozec, V. M. Canuto, et al. (2014), North Atlantic simulations in coordinated ocean-ice reference experiments phase II (CORE-II). Part I: mean states, *Ocean Modelling*, 73, 76–107.
- Davis, R. E. (1991), Observing the general circulation with floats, *Deep Sea Research Part A. Oceanographic Research Papers*, 38, S531–S571.
- de Jong, M. F., H. Søiland, A. S. Bower, and H. H. Furey (2018), The subsurface circulation of the Iceland Sea observed with RAFOS floats, *Deep Sea Research Part I: Oceanographic Research Papers*, 141, 1–10.
- Dengler, M., F. Schott, C. Eden, P. Brandt, J. Fischer, and R. J. Zantopp (2004), Break-up of the Atlantic deep western boundary current into eddies at 8°S, *Nature*, 432(7020), 1018.
- Dickson, R. R., and J. Brown (1994), The production of North Atlantic Deep Water: sources, rates, and pathways, *Journal of Geophysical Research: Oceans*, 99(C6), 12,319–12,341.
- Döös, K. (1995), Inter-ocean exchange of water masses, *Journal of Geophysical Research: Oceans*, 100(C7), 13,499–13,514.
- Dugstad, J., I. Koszalka, P. E. Isachsen, K.-F. Dagestad, and I. Fer (2019a), Vertical structure and seasonal variability of the inflow to the Lofoten Basin inferred from high resolution Lagrangian simulations, *Journal of Geophysical Research: Oceans*, doi: 10.1029/2019JC015474.
- Dugstad, J., I. Fer, J. LaCasce, M. Sanchez de La Lama, and M. Trodahl (2019b), Lateral heat transport in the lofoten basin: Near-surface pathways and subsurface exchange, *Journal of Geophysical Research: Oceans*, 124(5), 2992–3006.
- Eady, E. T. (1949), Long waves and cyclone waves, *Tellus*, 1(3), 33–52.
- Eldevik, T., F. Straneo, A. B. Sandø, and T. Furevik (2005), Pathways and export of Greenland Sea water, *The Nordic Seas: An integrated perspective*, pp. 89–103.
- Eldevik, T., J. E. Ø. Nilsen, D. Iovino, K. A. Olsson, A. B. Sandø, and H. Drange (2009), Observed sources and variability of Nordic Seas overflow, *Nature Geoscience*, 2(6), 406.
- Fer, I., A. Bosse, B. Ferron, and P. Bouruet-Aubertot (2018), The dissipation of kinetic energy in the Lofoten Basin Eddy, *Journal of Physical Oceanography*, 48(6), 1299–1316.

- Fetterer, F., K. Knowles, W. Meier, M. Savoie, and A. K. Windnagel (2017), Sea Ice Index, Version 3, pp. Boulder, Colorado USA. NSIDC: National Snow and Ice Data Center.
- Fronval, T., and E. Jansen (1996), Rapid changes in ocean circulation and heat flux in the Nordic seas during the last interglacial period, *Nature*, 383(6603), 806.
- Furevik, T., J. Nilsen, et al. (2005), Large-scale atmospheric circulation variability and its impacts on the Nordic Seas ocean climate—a review, *GEOPHYSICAL MONOGRAPH-AMERICAN GEOPHYSICAL UNION*, 158, 105.
- Gary, S. F., M. S. Lozier, A. Biastoch, and C. W. Böning (2012), Reconciling tracer and float observations of the export pathways of Labrador Sea Water, *Geophysical Research Letters*, 39(24).
- Gelderloos, R., C. A. Katsman, and S. S. Drijfhout (2011), Assessing the roles of three eddy types in restratifying the Labrador Sea after deep convection, *Journal of Physical Oceanography*, 41(11), 2102–2119.
- Gelderloos, R., T. W. Haine, I. M. Koszalka, and M. G. Magaldi (2017), Seasonal Variability in Warm-Water Inflow toward Kangerdlugssuaq Fjord, *Journal of Physical Oceanography*, 47(7), 1685–1699.
- Georgiou, S., C. G. van der Boog, N. Brüggemann, S. L. Ypma, J. D. Pietrzak, and C. A. Katsman (2019), On the interplay between downwelling, deep convection and mesoscale eddies in the Labrador Sea, *Ocean Modelling*, 135, 56–70.
- Georgiou, S., S. L. Ypma, N. Brüggemann, J.-M. Sayol, J. D. Pietrzak, and C. A. Katsman (2020), Pathways of the water masses exiting the Labrador Sea: The importance of boundary-interior exchanges, *Ocean Modelling*, p. 101623.
- Gill, A. E. (1982), *Atmosphere-Ocean dynamics (International Geophysics Series)*, academic press.
- Griffies, S. M., A. Biastoch, C. Böning, F. Bryan, G. Danabasoglu, E. P. Chassignet, M. H. England, R. Gerdes, H. Haak, R. W. Hallberg, et al. (2009), Coordinated ocean-ice reference experiments (COREs), *Ocean Modelling*, 26(1-2), 1–46.
- Hallberg, R. (2013), Using a resolution function to regulate parameterizations of oceanic mesoscale eddy effects, *Ocean Modelling*, 72, 92–103.
- Hanna, E., J. Cappelen, X. Fettweis, P. Huybrechts, A. Luckman, and M. Ribergaard (2009), Hydrologic response of the Greenland ice sheet: the role of oceanographic warming, *Hydrological Processes: An International Journal*, 23(1), 7–30.
- Hansen, B., and S. Østerhus (2000), North Atlantic–Nordic Seas exchanges, *Progress in Oceanography*, 45(2), 109–208.
- Hansen, B., H. Hátún, R. Kristiansen, S. Olsen, and S. Østerhus (2010), Stability and forcing of the Iceland–Faroe inflow of water, heat, and salt to the Arctic, *Ocean Science*, 6(4), 1013–1026.

- Harden, B. E., I. A. Renfrew, and G. N. Petersen (2015), Meteorological buoy observations from the central Iceland Sea, *Journal of Geophysical Research: Atmospheres*, 120(8), 3199–3208.
- Harden, B. E., R. S. Pickart, H. Valdimarsson, K. Våge, L. de Steur, C. Richards, F. Bahr, D. Torres, E. Børve, S. Jónsson, et al. (2016), Upstream sources of the Denmark Strait Overflow: Observations from a high-resolution mooring array, *Deep Sea Research Part I: Oceanographic Research Papers*, 112, 94–112.
- Håvik, L., R. S. Pickart, K. Våge, D. Torres, A. M. Thurnherr, A. Beszczynska-Möller, W. Walczowski, and W.-J. von Appen (2017), Evolution of the East Greenland Current from Fram Strait to Denmark Strait: Synoptic measurements from summer 2012, *Journal of Geophysical Research: Oceans*, 122(3), 1974–1994.
- Helland-Hansen, B., and F. Nansen (1909), *The Norwegian Sea: its physical oceanography based upon the Norwegian researches 1900-1904*, Det Mallingske bogtrykkeri.
- Henry, L., J. F. McManus, W. B. Curry, N. L. Roberts, A. M. Piotrowski, and L. D. Keigwin (2016), North Atlantic ocean circulation and abrupt climate change during the last glaciation, *Science*, 353(6298), 470–474.
- Hurrell, J. W., Y. Kushnir, and M. Visbeck (2001), The North Atlantic oscillation, *Science*, 291(5504), 603–605.
- Iovino, D., F. Straneo, and M. A. Spall (2008), On the effect of a sill on dense water formation in a marginal sea, *Journal of Marine Research*, 66(3), 325–345.
- IPCC (2013), *Climate Change 2013: The Physical Science Basis. Contribution of Working Group I to the Fifth Assessment Report of the Intergovernmental Panel on Climate Change*, 1535 pp., Cambridge University Press, Cambridge, United Kingdom and New York, NY, USA, doi:10.1017/CBO9781107415324.
- Isachsen, P., I. Koszalka, and J. LaCasce (2012), Observed and modeled surface eddy heat fluxes in the eastern Nordic Seas, *Journal of Geophysical Research: Oceans*, 117(C8).
- Isachsen, P. E. (2015), Baroclinic instability and the mesoscale eddy field around the Lofoten Basin, *Journal of Geophysical Research: Oceans*, 120(4), 2884–2903.
- Isachsen, P. E., and O. A. Nøst (2012), The air-sea transformation and residual overturning circulation within the Nordic Seas, *Journal of Marine Research*, 70(1), 31–68.
- Isachsen, P. E., J. LaCasce, C. Mauritzen, and S. Häkkinen (2003), Wind-driven variability of the large-scale recirculating flow in the Nordic Seas and Arctic Ocean, *Journal of Physical Oceanography*, 33(12), 2534–2550.
- Isachsen, P. E., C. Mauritzen, and H. Svendsen (2007), Dense water formation in the Nordic Seas diagnosed from sea surface buoyancy fluxes, *Deep Sea Research Part I: Oceanographic Research Papers*, 54(1), 22–41.

- Isachsen, P. E., S. R. Sørli, C. Mauritzen, C. Lydersen, P. Dodd, and K. M. Kovacs (2014), Upper-ocean hydrography of the Nordic Seas during the International Polar Year (2007–2008) as observed by instrumented seals and Argo floats, *Deep Sea Research Part I: Oceanographic Research Papers*, 93, 41–59.
- Jakobsen, P. K., M. H. Ribergaard, D. Quadfasel, T. Schmith, and C. W. Hughes (2003), Near-surface circulation in the northern North Atlantic as inferred from Lagrangian drifters: Variability from the mesoscale to interannual, *Journal of Geophysical Research: Oceans*, 108(C8).
- Jochumsen, K., M. Moritz, N. Nunes, D. Quadfasel, K. M. Larsen, B. Hansen, H. Valdimarsson, and S. Jonsson (2017), Revised transport estimates of the Denmark Strait overflow, *Journal of Geophysical Research: Oceans*, 122(4), 3434–3450.
- Johansen, U., H. Bull-Berg, L. H. Vik, A. M. Stokka, R. Richardsen, and U. Winther (2019), The Norwegian seafood industry—Importance for the national economy, *Marine Policy*, p. 103561.
- Johnson, H. L., P. Cessi, D. P. Marshall, F. Schloesser, and M. A. Spall (2019), Recent contributions of theory to our understanding of the Atlantic Meridional Overturning Circulation, *Journal of Geophysical Research: Oceans*, 124(8), 5376–5399.
- Jónsson, S. (1992), Sources of fresh water in the Iceland Sea and the mechanisms governing its interannual variability, in *ICES Marine Science Symposia*, vol. 195, pp. 62–67.
- Jonsson, S., and H. Valdimarsson (2004), A new path for the Denmark Strait overflow water from the Iceland Sea to Denmark Strait, *Geophysical Research Letters*, 31(3).
- Jónsson, S., and H. Valdimarsson (2005), The flow of Atlantic water to the North Icelandic Shelf and its relation to the drift of cod larvae, *ICES Journal of Marine Science*, 62(7), 1350–1359.
- Jónsson, S., and H. Valdimarsson (2012), Water mass transport variability to the North Icelandic shelf, 1994–2010, *ICES journal of marine science*, 69(5), 809–815.
- Katsman, C. A., M. A. Spall, and R. S. Pickart (2004), Boundary current eddies and their role in the restratification of the Labrador Sea, *Journal of Physical Oceanography*, 34(9), 1967–1983.
- Katsman, C. A., S. Drijfhout, H. A. Dijkstra, and M. A. Spall (2018), Sinking of dense North Atlantic waters in a global ocean model: Location and controls, *Journal of Geophysical Research: Oceans*, 123(5), 3563–3576.
- Köhl, A. (2007), Generation and stability of a quasi-permanent vortex in the Lofoten Basin, *Journal of Physical Oceanography*, 37(11), 2637–2651.
- Köhl, A. (2010), Variable source regions of Denmark Strait and Faroe Bank Channel overflow waters, *Tellus A*, 62(4), 551–568.

- Köhl, A., R. H. Käse, D. Stammer, and N. Serra (2007), Causes of changes in the Denmark Strait overflow, *Journal of physical oceanography*, 37(6), 1678–1696.
- Korablev, A., O. K. Baranova, A. D. Smirnov, D. Seidov, and A. R. Parsons (2014), Climatological atlas of the Nordic Seas and northern North Atlantic.
- Koszalka, I., J. LaCasce, M. Andersson, K. Orvik, and C. Mauritzen (2011), Surface circulation in the Nordic Seas from clustered drifters, *Deep Sea Research Part I: Oceanographic Research Papers*, 58(4), 468–485.
- Koszalka, I., J. LaCasce, and C. Mauritzen (2013a), In pursuit of anomalies—Analyzing the poleward transport of Atlantic Water with surface drifters, *Deep Sea Research Part II: Topical Studies in Oceanography*, 85, 96–108.
- Koszalka, M. I., T. W. Haine, and M. G. Magaldi (2013b), Fates and travel times of Denmark Strait overflow water in the Irminger Basin, *Journal of Physical Oceanography*, 43(12), 2611–2628.
- Kuhlbrodt, T., A. Griesel, M. Montoya, A. Levermann, M. Hofmann, and S. Rahmstorf (2007), On the driving processes of the Atlantic meridional overturning circulation, *Reviews of Geophysics*, 45(2).
- Lambert, E., T. Eldevik, and M. A. Spall (2018), On the Dynamics and Water Mass Transformation of a Boundary Current Connecting Alpha and Beta Oceans, *Journal of Physical Oceanography*, 48(10), 2457–2475.
- Langehaug, H., D. Matei, T. Eldevik, K. Lohmann, and Y. Gao (2017), On model differences and skill in predicting sea surface temperature in the Nordic and Barents Seas, *Climate Dynamics*, 48(3-4), 913–933.
- Langehaug, H. R., I. Medhaug, T. Eldevik, and O. H. Otterå (2012), Arctic/Atlantic exchanges via the subpolar gyre, *Journal of Climate*, 25(7), 2421–2439.
- Large, W. G., and S. Yeager (2009), The global climatology of an interannually varying air–sea flux data set, *Climate Dynamics*, 33(2-3), 341–364.
- Large, W. G., J. C. McWilliams, and S. C. Doney (1994), Oceanic vertical mixing: A review and a model with a nonlocal boundary layer parameterization, *Reviews of Geophysics*, 32(4), 363–403.
- Latarius, K., and D. Quadfasel (2016), Water mass transformation in the deep basins of the Nordic Seas: Analyses of heat and freshwater budgets, *Deep Sea Research Part I: Oceanographic Research Papers*, 114, 23–42.
- Ledwell, J. R., A. J. Watson, and C. S. Law (1993), Evidence for slow mixing across the pycnocline from an open-ocean tracer-release experiment, *Nature*, 364(6439), 701.
- Levermann, A., A. Griesel, M. Hofmann, M. Montoya, and S. Rahmstorf (2005), Dynamic sea level changes following changes in the thermohaline circulation, *Climate Dynamics*, 24(4), 347–354.

- Levitus, S., J. Antonov, and T. Boyer (2005), Warming of the world ocean, 1955–2003, *Geophysical Research Letters*, 32(2).
- Logemann, K., J. Ólafsson, Á. Snorrason, H. Valdimarsson, and G. Marteinsdóttir (2013), The circulation of Icelandic waters - a modelling study., *Ocean Science Discussions*, 10(2).
- Lozier, M., F. Li, S. Bacon, F. Bahr, A. Bower, S. Cunningham, M. De Jong, L. De Steur, B. Deyoung, J. Fischer, et al. (2019), A sea change in our view of overturning in the subpolar North Atlantic, *Science*, 363(6426), 516–521.
- Lozier, M. S., S. F. Gary, and A. S. Bower (2013), Simulated pathways of the overflow waters in the North Atlantic: Subpolar to subtropical export, *Deep Sea Research Part II: Topical Studies in Oceanography*, 85, 147–153.
- Lumpkin, R., and M. Pazos (2007), *Measuring surface currents with Surface Velocity Program drifters: the instrument, its data, and some recent results*, 39–67 pp., Cambridge University Press Cambridge.
- Malmberg, S.-A. (1983), Hydrographic investigations in the Iceland and Greenland Seas in late winter 1971-Deep Water Project, *Jokull Reykjavik*, 33, 133–140.
- Marnela, M., B. Rudels, M.-N. Houssais, A. Beszczynska-Möller, and P. Eriksson (2013), Recirculation in the Fram Strait and transports of water in and north of the Fram Strait derived from CTD data., *Ocean Science Discussions*, 9(5).
- Marshall, J., and F. Schott (1999), Open-ocean convection: Observations, theory, and models, *Reviews of Geophysics*, 37(1), 1–64.
- Marshall, J., A. Adcroft, C. Hill, L. Perelman, and C. Heisey (1997), A finite-volume, incompressible Navier Stokes model for studies of the ocean on parallel computers, *Journal of Geophysical Research: Oceans*, 102(C3), 5753–5766.
- Mauritzen, C. (1996), Production of dense overflow waters feeding the North Atlantic across the Greenland-Scotland Ridge. Part 1: Evidence for a revised circulation scheme, *Deep Sea Research Part I: Oceanographic Research Papers*, 43(6), 769–806.
- Meincke, J., S. Jonsson, and J. H. Swift (1992), Variability of convective conditions in the Greenland Sea, in *ICES Mar. Sci. Symp*, vol. 195, pp. 32–39.
- Messias, M.-J., A. Watson, T. Johannessen, K. Oliver, K. Olsson, E. Fogelqvist, J. Olafsson, S. Bacon, J. Balle, N. Bergman, et al. (2008), The Greenland Sea tracer experiment 1996–2002: horizontal mixing and transport of Greenland Sea intermediate water, *Progress in Oceanography*, 78(1), 85–105.
- Millero, F. J., and A. Poisson (1981), International one-atmosphere equation of state of seawater, *Deep Sea Research Part A. Oceanographic Research Papers*, 28(6), 625–629.
- Moore, G. W. K., K. Våge, R. S. Pickart, and I. A. Renfrew (2015), Decreasing intensity of open-ocean convection in the Greenland and Iceland seas, *Nature Climate Change*, 5(9), 877.

- Mork, K. A., and J. Blindheim (2000), Variations in the Atlantic inflow to the Nordic Seas, 1955–1996, *Deep Sea Research Part I: Oceanographic Research Papers*, 47(6), 1035–1057.
- Mork, K. A., and O. Skagseth (2005), Annual sea surface height variability in the Nordic Seas, *GEOPHYSICAL MONOGRAPH-AMERICAN GEOPHYSICAL UNION*, 158, 51.
- Mork, K. A., and Ø. Skagseth (2010), A quantitative description of the Norwegian Atlantic Current by combining altimetry and hydrography, *Ocean Science*, 6(4), 901–911.
- Nilsen, J. E. Ø., and E. Falck (2006), Variations of mixed layer properties in the Norwegian Sea for the period 1948–1999, *Progress in Oceanography*, 70(1), 58–90.
- Nøst, O. A., and P. E. Isachsen (2003), The large-scale time-mean ocean circulation in the Nordic Seas and Arctic Ocean estimated from simplified dynamics, *Journal of Marine Research*, 61(2), 175–210.
- Nurser, A., and S. Bacon (2014), The Rossby radius in the Arctic Ocean, *Ocean Science*, 10(6), 967–975.
- Olbers, D., J. Willebrand, and C. Eden (2012), *Ocean dynamics*, Springer Science & Business Media.
- Olsson, K. A., E. Jeansson, L. G. Anderson, B. Hansen, T. Eldevik, R. Kristiansen, M.-J. Messias, T. Johannessen, and A. J. Watson (2005), Intermediate water from the Greenland Sea in the Faroe Bank Channel: spreading of released sulphur hexafluoride, *Deep Sea Research Part I: Oceanographic Research Papers*, 52(2), 279–294.
- Onarheim, I. H., L. H. Smedsrud, R. B. Ingvaldsen, and F. Nilsen (2014), Loss of sea ice during winter north of Svalbard, *Tellus A: Dynamic Meteorology and Oceanography*, 66(1), 23,933.
- Orvik, K. A., and P. Niiler (2002), Major pathways of Atlantic water in the northern North Atlantic and Nordic Seas toward Arctic, *Geophysical Research Letters*, 29(19), 2–1.
- Orvik, K. A., and Ø. Skagseth (2005), Heat flux variations in the eastern Norwegian Atlantic Current toward the Arctic from moored instruments, 1995–2005, *Geophysical Research Letters*, 32(14).
- Orvik, K. A., Ø. Skagseth, and M. Mork (2001), Atlantic inflow to the Nordic Seas: current structure and volume fluxes from moored current meters, VM-ADCP and SeaSoar-CTD observations, 1995–1999, *Deep Sea Research Part I: Oceanographic Research Papers*, 48(4), 937–957.
- Østerhus, S., R. Woodgate, H. Valdimarsson, B. Turrell, L. de Steur, D. Quadfasel, S. M. Olsen, M. Moritz, C. M. Lee, K. M. H. Larsen, S. Jónsson, C. Johnson, K. Jochumsen, B. Hansen, B. Curry, S. Cunningham, and B. Berx (2019), Arctic Mediterranean exchanges: a consistent volume budget and trends in transports from two decades of observations, *Ocean Science*, 15, 379–399.

- Paris, C. B., J. Helgers, E. Van Sebille, and A. Srinivasan (2013), Connectivity Modeling System: A probabilistic modeling tool for the multi-scale tracking of biotic and abiotic variability in the ocean, *Environmental Modelling & Software*, 42, 47–54.
- Perkins, H., T. Hopkins, S.-A. Malmberg, P.-M. Poulain, and A. Warn-Varnas (1998), Oceanographic conditions east of Iceland, *Journal of Geophysical Research: Oceans*, 103(C10), 21,531–21,542.
- Pickart, R. S., M. A. Spall, D. J. Torres, K. Våge, H. Valdimarsson, C. Nobre, G. Moore, S. Jonsson, and D. Mastropole (2017), The North Icelandic Jet and its relationship to the North Icelandic Irminger Current, *Journal of Marine Research*, 75(5), 605–639.
- Piechura, J., and W. Walczowski (1995), The Arctic Front: structure and dynamics, *Oceanologia*, 37(1), 47–73.
- Polyakov, I. V., A. V. Pnyushkov, M. B. Alkire, I. M. Ashik, T. M. Baumann, E. C. Carmack, I. Goszczko, J. Guthrie, V. V. Ivanov, T. Kanzow, et al. (2017), Greater role for Atlantic inflows on sea-ice loss in the Eurasian Basin of the Arctic Ocean, *Science*, 356(6335), 285–291.
- Poulain, P.-M., A. Warn-Varnas, and P. Niiler (1996), Near-surface circulation of the Nordic Seas as measured by Lagrangian drifters, *Journal of Geophysical Research: Oceans*, 101(C8), 18,237–18,258.
- Qin, X., E. van Sebille, and A. S. Gupta (2014), Quantification of errors induced by temporal resolution on Lagrangian particles in an eddy-resolving model, *Ocean Modelling*, 76, 20–30.
- Rahmstorf, S., and A. Ganopolski (1999), Long-term global warming scenarios computed with an efficient coupled climate model, *Climatic change*, 43(2), 353–367.
- Rahmstorf, S., J. E. Box, G. Feulner, M. E. Mann, A. Robinson, S. Rutherford, and E. J. Schaffernicht (2015), Exceptional twentieth-century slowdown in Atlantic Ocean overturning circulation, *Nature climate change*, 5(5), 475.
- Raj, R. P., S. Chatterjee, L. Bertino, A. Turiel, and M. Portabella (2019), The Arctic Front and its variability in the Norwegian Sea, *Ocean Science*, 15(6), 1729–1744.
- Rayner, D., J. J.-M. Hirschi, T. Kanzow, W. E. Johns, P. G. Wright, E. Frajka-Williams, H. L. Bryden, C. S. Meinen, M. O. Baringer, J. Marotzke, et al. (2011), Monitoring the Atlantic meridional overturning circulation, *Deep Sea Research Part II: Topical Studies in Oceanography*, 58(17-18), 1744–1753.
- Read, J., and R. Pollard (1992), Water masses in the region of the Iceland–Faeroes Front, *Journal of Physical Oceanography*, 22(11), 1365–1378.
- Rhines, P., S. Häkkinen, and S. A. Josey (2008), Is oceanic heat transport significant in the climate system?, in *Arctic–subarctic ocean fluxes*, pp. 87–109, Springer.

- Richards, C. G., and F. Straneo (2015), Observations of water mass transformation and eddies in the Lofoten Basin of the Nordic seas, *Journal of Physical Oceanography*, 45(6), 1735–1756.
- Rossby, T., M. Prater, and H. Søliland (2009a), Pathways of inflow and dispersion of warm waters in the Nordic Seas, *Journal of Geophysical Research: Oceans*, 114(C4).
- Rossby, T., V. Ozhigin, V. Ivshin, and S. Bacon (2009b), An isopycnal view of the Nordic Seas hydrography with focus on properties of the Lofoten Basin, *Deep Sea Research Part I: Oceanographic Research Papers*, 56(11), 1955–1971.
- Ruan, X., and J. Callies (2019), Mixing-driven mean flows and submesoscale eddies over mid-ocean ridge flanks and fracture zone canyons, *Journal of Physical Oceanography*, doi:10.1175/JPO-D-19-0174.1.
- Rudels, B., D. Quadfasel, H. Friedrich, and M.-N. Houssais (1989), Greenland Sea convection in the winter of 1987–1988, *Journal of Geophysical Research: Oceans*, 94(C3), 3223–3227.
- Rühs, S., J. V. Durgadoo, E. Behrens, and A. Biastoch (2013), Advective timescales and pathways of Agulhas leakage, *Geophysical Research Letters*, 40(15), 3997–4000.
- Saloranta, T. M., and H. Svendsen (2001), Across the Arctic front west of Spitsbergen: high-resolution CTD sections from 1998–2000, *Polar Research*, 20(2), 177–184.
- Sandø, A. B., and T. Furevik (2008), Relation between the wind stress curl in the North Atlantic and the Atlantic inflow to the Nordic Seas, *Journal of Geophysical Research: Oceans*, 113(C6).
- Sayol, J.-M., H. Dijkstra, and C. Katsman (2019), Seasonal and regional variations of sinking in the subpolar North Atlantic from a high-resolution ocean model, *Ocean Science*, 15(4), 1033–1053.
- Screen, J. A., and I. Simmonds (2010), The central role of diminishing sea ice in recent arctic temperature amplification, *Nature*, 464(7293), 1334.
- Segtnan, O., T. Furevik, and A. Jenkins (2011), Heat and freshwater budgets of the Nordic seas computed from atmospheric reanalysis and ocean observations, *Journal of Geophysical Research: Oceans*, 116(C11).
- Semper, S., K. Våge, R. S. Pickart, H. Valdimarsson, D. J. Torres, and S. Jónsson (2019), The emergence of the North Icelandic Jet and its evolution from northeast Iceland to Denmark Strait, *Journal of Physical Oceanography*, 49(10), 2499–2521.
- Send, U., and J. Marshall (1995), Integral effects of deep convection, *Journal of physical oceanography*, 25(5), 855–872.
- Shao, Q., J. Zhao, K. F. Drinkwater, X. Wang, and Y. Cao (2019), Internal overflow in the Nordic Seas and the cold reservoir in the northern Norwegian Basin, *Deep Sea Research Part I: Oceanographic Research Papers*, 148, 67–79.

- Skogen, M. D., W. P. Budgell, and F. Rey (2007), Interannual variability in Nordic seas primary production, *ICES Journal of Marine Science*, 64(5), 889–898.
- Skreslet, S. (2007), History of Norwegian marine science, *Océanis*, 33(3-4), 139–165.
- Smith, W. H., and D. T. Sandwell (1997), Global sea floor topography from satellite altimetry and ship depth soundings, *Science*, 277(5334), 1956–1962.
- Søiland, H., L. Chafik, and T. Rossby (2016), On the long-term stability of the Lofoten Basin Eddy, *Journal of Geophysical Research: Oceans*, 121(7), 4438–4449.
- Spall, M. A. (2004), Boundary currents and watermass transformation in marginal seas, *Journal of Physical Oceanography*, 34(5), 1197–1213.
- Spall, M. A. (2010), Non-local topographic influences on deep convection: An idealized model for the Nordic Seas, *Ocean Modelling*, 32(1), 72–85.
- Spall, M. A. (2011), On the role of eddies and surface forcing in the heat transport and overturning circulation in marginal seas, *Journal of Climate*, 24(18), 4844–4858.
- Spall, M. A. (2012), Influences of precipitation on water mass transformation and deep convection, *Journal of Physical Oceanography*, 42(10), 1684–1700.
- Spall, M. A., and R. S. Pickart (2001), Where does dense water sink? A subpolar gyre example, *Journal of Physical Oceanography*, 31(3), 810–826.
- Spence, P., R. M. Holmes, A. M. Hogg, S. M. Griffies, K. D. Stewart, and M. H. England (2017), Localized rapid warming of West Antarctic subsurface waters by remote winds, *Nature Climate Change*, 7(8), 595.
- Spielhagen, R. F., K. Werner, S. A. Sørensen, K. Zamelczyk, E. Kandiano, G. Budeus, K. Husum, T. M. Marchitto, and M. Hald (2011), Enhanced modern heat transfer to the Arctic by warm Atlantic water, *Science*, 331(6016), 450–453.
- Stefánsson, U. (1962), *North Icelandic waters*, Atvinnudeild Háskólans, Fiskideild.
- Stommel, H. (1961), Thermohaline convection with two stable regimes of flow, *Tellus*, 13(2), 224–230.
- Straneo, F. (2006a), On the connection between dense water formation, overturning, and poleward heat transport in a convective basin, *Journal of physical oceanography*, 36(9), 1822–1840.
- Straneo, F. (2006b), Heat and freshwater transport through the central Labrador Sea, *Journal of Physical Oceanography*, 36(4), 606–628.
- Straneo, F., and P. Heimbach (2013), North Atlantic warming and the retreat of Greenland’s outlet glaciers, *Nature*, 504(7478), 36–43.
- Straneo, F., G. S. Hamilton, D. A. Sutherland, L. A. Stearns, F. Davidson, M. O. Hammill, G. B. Stenson, and A. Rosing-Asvid (2010), Rapid circulation of warm subtropical waters in a major glacial fjord in East Greenland, *Nature Geoscience*, 3(3), 182.

- Swift, J. H., and K. Aagaard (1981), Seasonal transitions and water mass formation in the Iceland and Greenland seas, *Deep Sea Research Part A. Oceanographic Research Papers*, 28(10), 1107–1129.
- Takahashi, T., S. C. Sutherland, R. Wanninkhof, C. Sweeney, R. A. Feely, D. W. Chipman, B. Hales, G. Friederich, F. Chavez, C. Sabine, et al. (2009), Climatological mean and decadal change in surface ocean pCO<sub>2</sub>, and net sea–air CO<sub>2</sub> flux over the global oceans, *Deep Sea Research Part II: Topical Studies in Oceanography*, 56(8–10), 554–577.
- Tréguier, A.-M., S. Theetten, E. P. Chassignet, T. Penduff, R. Smith, L. Talley, J. Beismann, and C. Böning (2005), The North Atlantic subpolar gyre in four high-resolution models, *Journal of Physical Oceanography*, 35(5), 757–774.
- Trodahl, M., and P. E. Isachsen (2018), Topographic influence on baroclinic instability and the mesoscale eddy field in the northern North Atlantic Ocean and the Nordic Seas, *Journal of Physical Oceanography*, 48(11), 2593–2607.
- Våge, K., R. S. Pickart, M. A. Spall, H. Valdimarsson, S. Jónsson, D. J. Torres, S. Østerhus, and T. Eldevik (2011), Significant role of the North Icelandic Jet in the formation of Denmark Strait overflow water, *Nature Geoscience*, 4(10), 723.
- Våge, K., R. S. Pickart, M. A. Spall, G. Moore, H. Valdimarsson, D. J. Torres, S. Y. Erofeeva, and J. E. Ø. Nilsen (2013), Revised circulation scheme north of the Denmark Strait, *Deep Sea Research Part I: Oceanographic Research Papers*, 79, 20–39.
- Våge, K., G. W. K. Moore, S. Jónsson, and H. Valdimarsson (2015), Water mass transformation in the Iceland Sea, *Deep Sea Research Part I: Oceanographic Research Papers*, 101, 98–109.
- Våge, K., L. Papritz, L. Håvik, M. A. Spall, and G. Moore (2018), Ocean convection linked to the recent ice edge retreat along east Greenland, *Nature Communications*, 9(1), 1287.
- Valdimarsson, H., and S.-A. Malmberg (1999), Near-surface circulation in Icelandic waters derived from satellite tracked drifters, *Rit Fiskideild*, 16, 23–40.
- van Aken, H. M., G. Budeus, and M. Hähnel (1995), The anatomy of the Arctic frontal zone in the Greenland Sea, *Journal of Geophysical Research: Oceans*, 100(C8), 15,999–16,014.
- van Sebille, E., P. Spence, M. R. Mazloff, M. H. England, S. R. Rintoul, and O. A. Saenko (2013), Abyssal connections of Antarctic Bottom Water in a Southern Ocean state estimate, *Geophysical Research Letters*, 40(10), 2177–2182.
- Van Sebille, E., S. M. Griffies, R. Abernathy, T. P. Adams, P. Berloff, A. Biastoch, B. Blanke, E. P. Chassignet, Y. Cheng, C. J. Cotter, et al. (2018), Lagrangian ocean analysis: Fundamentals and practices, *Ocean Modelling*, 121, 49–75.
- Voet, G., D. Quadfasel, K. A. Mork, and H. Søliland (2010), The mid-depth circulation of the Nordic Seas derived from profiling float observations, *Tellus A*, 62(4), 516–529.

- Volkov, D. L., T. V. Belonenko, and V. R. Foux (2013), Puzzling over the dynamics of the Lofoten Basin—a sub-Arctic hot spot of ocean variability, *Geophysical Research Letters*, 40(4), 738–743.
- Wagner, P., S. Rühls, F. U. Schwarzkopf, I. M. Koszalka, and A. Biastoch (2019), Can Lagrangian tracking simulate tracer spreading in a high-resolution Ocean General Circulation Model?, *Journal of Physical Oceanography*, 49(5), 1141–1157.
- Walczowski, W. (2013), Frontal structures in the West Spitsbergen Current margins., *Ocean Science*, 9(6), 957–975.
- Walin, G., G. Broström, J. Nilsson, and O. Dahl (2004), Baroclinic boundary currents with downstream decreasing buoyancy: A study of an idealized Nordic Seas system, *Journal of Marine Research*, 62(4), 517–543.
- Weijer, W., M. Maltrud, M. Hecht, H. Dijkstra, and M. Kliphuis (2012), Response of the Atlantic Ocean circulation to Greenland Ice Sheet melting in a strongly-eddy ocean model, *Geophysical Research Letters*, 39(9).
- Wekerle, C., Q. Wang, S. Danilov, V. Schourup-Kristensen, W.-J. von Appen, and T. Jung (2017), Atlantic Water in the Nordic Seas: Locally eddy-permitting ocean simulation in a global setup, *Journal of Geophysical Research: Oceans*, 122(2), 914–940.
- Wijffels, S. E., R. W. Schmitt, H. L. Bryden, and A. Stigebrandt (1992), Transport of freshwater by the oceans, *Journal of Physical Oceanography*, 22(2), 155–162.
- Willebrand, J., B. Barnier, C. Böning, C. Dieterich, P. D. Killworth, C. Le Provost, Y. Jia, J.-M. Molines, and A. L. New (2001), Circulation characteristics in three eddy-permitting models of the North Atlantic, *Progress in Oceanography*, 48(2-3), 123–161.
- Yeager, S., and G. Danabasoglu (2012), Sensitivity of Atlantic meridional overturning circulation variability to parameterized Nordic Sea overflows in CCSM4, *Journal of Climate*, 25(6), 2077–2103.
- Ypma, S., E. van Sebille, A. Kiss, and P. Spence (2016), The separation of the East Australian Current: A Lagrangian approach to potential vorticity and upstream control, *Journal of Geophysical Research: Oceans*, 121(1), 758–774.

# ACKNOWLEDGEMENTS

The pathway through my PhD was as the quote on the first page describes; I've changed direction many times. There are many people to thank who have made sure that I did not get lost and who contributed to me completing this chapter of my life.

First of all, the level of coherence between the original proposal and the contents of this thesis proof the degree of freedom you gave me, Caroline. As a supervisor and promotor you allowed me to visit an insane number of conferences, without which I would not have had the scientific network I have now. You allowed me to visit other institutes in Norway and in Boston, without which I would have never finished this PhD on time. You allowed me to collaborate, something I now know one can not take for granted. You allowed me to work parttime, so I could get a taste of another career path. But above all, you allowed me to be open, honest, to work in an inclusive and protective environment, growing with the positive and learning from the negative. Thank you.

Julie, I valued our conversations in your office, at dinners and at conferences. Although coastal processes never entered my thesis, you believed in me as a researcher and almost danced in your chair when I announced I would proceed as a PostDoc. You surprised me with new insights (not necessarily PhD related) and made me question my own firm opinions, showing the truth behind the quote on the first page of this thesis.

Although I might have envisioned my PhD defence ceremony in a slightly different way, I would like to thank my committee for being there, whether it was in real life or via a screen. Thank you for reading my thesis, thank you for some great chats at conferences and thank you for all your input.

What a team we had. The two people that made me feel most welcome, already before I officially started my PhD, were Nils and Sotiria. Nils might be the most precise person I know, sometimes having made me wonder whether I should retake all my oceanography courses, maybe even my Physics bachelor. But the patience you have Nils, it is something you should cherish. I'm extremely grateful to have had you around during the first steps of my PhD.

Sotiria, we stuck together from the beginning to the end. Thank you for always being there, thank you for all the nice food, cookies and cakes, thank you for the reminders for everyone else's birthday (and name). And Sabine, thank you for always being there to help us with anything and for letting me stay at your place whenever I needed to be in Delft early. You both took care of me during the interesting little adventures we had; when I got kicked off a flight home, when I fell ill during our conference in New Orleans. Every time I was at home and something needed to be done in Delft, one of you was ready to jump in. I could not have wished for better colleagues, let alone friends. We saw each other grow and I can't wait to celebrate our victories together in Greece and

Switzerland. *θα μου λειψει!*

I could not have written this thesis without the input and help from researchers all over the world. Thank you for sharing your model data, Paul Spence and Johannes Dugstad, for sharing observations, Benjamin Harden or pointing me to the right observational data sets, Stephanie Semper. Thank you for the immense input of knowledge on the Nordic Seas and theoretical processes, Kjetil Våge, Mike Spall, Pål Erik Isachsen and Jan Even Nilsen. And thank you, Erwin, for coincidentally choosing a similar PhD topic as mine, welcoming me in Bergen, introducing me to the right people, sharing your knowledge on idealized models and theoretical frameworks and allowing me to crash in your office every time my home desk felt less appealing.

Yes, the right office mates make a PhD that little bit more doable. Floris, Carine and Gal, thank you for always being there, even when I was barely around, you were always in for a chat and a coffee. Although you left soon after I started my PhD, thank you Dirk and James for helping us newbies - 'we have no idea what we got ourselves into' - with your veteran PhD-experiences. And thank you, Silke, Alejandra, Lennart, Juanma, Marion, Adam and Olga for always joining the second-floor lunches and coffee walks across campus. And not to forget, thank you Otti for being a great secretary, for arranging the annual bbq and scheduling the endless oral exams of Stratified Flows. I was lucky enough to have had more than one office to limit the travel time between Soest and Delft. A special thanks to Andre for providing me with a spot in your jungle office in Utrecht and thank you Tjebbe for your exquisite coffee knowledge. You both made me feel very welcome every time I went to Utrecht University.

And then there are all these people, who have nothing to do with my thesis and who were willing to listen to me talk (complain) on a daily basis for four years long about some ocean...

Rebekka en Saskia, wij snorren ons door elke belangrijke gebeurtenis in ons leven. Ode aan onze traditiegetrouwe weekenden met enerzijds een zeer hoog intelligente film, een zak chips en een bezoek aan het zwembad en anderzijds de meest uiteenlopende en diepe gesprekken. Een betere manier om de PhD-druk te relativeren bestaat er niet.

En dan uiteraard de muzikwereld niet te vergeten. Dank, lief strijkkwartet, Clara, Margriet en Roos, voor de fijne concerten, repetities en etentjes. Bedankt voor die inspirerende toiletmuur Roos, één van de quotes is me iets langer bijgebleven. Dank lieve muziekvrienden, voor alle mooie projecten die we gespeeld hebben in verscheidene orkesten, de tournee naar China en de Queen Symfonie die we in de aula van de TU Delft uitvoerden.

MPOCers, bedankt voor een onvergetelijk masterjaar en de daarop volgende uitjes, vakanties, gekkigheid en oneindige steun aan elkaar. En dank Erik, voor het inspireren tot het doen van onderzoek, voor het wijzen op deze PhD positie, en voor het aanbieden van een prachtige postdoc. Kim, wat was het fijn om af en toe samen te lunchen en trots te zijn dat we toch echt in Leiden onze bachelor hadden gedaan en nu, met maar een week verschil, beiden onze promotie in Delft tot een succesvol einde hebben gebracht. Ik ben benieuwd wat de toekomst in petto heeft.

Lieve mam en pap, dank voor het volste vertrouwen in mij dat het allemaal wel goed zou komen. Mijn broertjes, dank voor jullie wijsheid, het relativeren en de gezelligheid. En Eva, ja, je staat in de familiecategorie, wat onwijs fijn dat wij elkaar door en door kennen.

En aan mijn lieve Olfert, dank voor dat stukje fruit tijdens Denisov, dank voor het dekbed met de kaart van de Nordic Seas erop, dank voor onze buurman die een Fokke & Sukke tekening maakte als laatste steuntje in de rug, dank voor het overtuigen dat parkietjes de leukste huisdieren ooit zijn (Dreki, dankzij jou ben ik nooit alleen!) en dank voor het luisteren naar het dag in en uit geratel over mijn werk. Hoeveel pauken je ook in ons huis verstoopt, ik zal altijd van je houden.



# LIST OF PUBLICATIONS

## JOURNAL ARTICLES AS FIRST AUTHOR

**Ypma, S.L.**, Georgiou, S., Dugstad, J.S., Pietrzak, J.D., Katsman, C.A. (2020): Pathways and watermass transformation along and across the Mohn-Knipovich Ridge in the Nordic Seas. *Journal of Geophysical Research: Oceans*, 125, DOI:10.1029/2020JC016075 [**Chapter 3**]

**Ypma, S.L.**, Spall, M.A., Lambert, E., Georgiou, S., Pietrzak, J.D., Katsman, C.A. (2020): The contrasting dynamics of the buoyancy-forced Lofoten and Greenland Basins. *Journal of Physical Oceanography*, 50(5), 1227–1244. [**Chapter 2**]

**Ypma, S.L.**, Brüggemann, N., Georgiou, S., Spence, P., Dijkstra, H. A., Pietrzak, J. D., Katsman, C. A. (2019): Pathways and watermass transformation of Atlantic Water entering the Nordic Seas through Denmark Strait in two high resolution ocean models. *Deep Sea Research Part I: Oceanographic Research Papers*, 145, 59–72. [**Chapter 4**]

**Ypma, S.L.**, van Sebille, E., Kiss, A.E., Spence, P. (2016): The separation of the East Australian Current: A Lagrangian approach to potential vorticity and upstream control. *Journal of Geophysical Research: Oceans*, 121(1), 758–774.

## JOURNAL ARTICLES AS CO-AUTHOR

Georgiou, S., **Ypma, S.L.**, Brüggemann, N., Sayol, J.M., van der Boog, C.G., Spence, P., Pietrzak, J.D., Katsman, C. A. (*submitted*): Impact of direct and indirect pathways of water masses found in the Labrador Sea on its overturning dynamics. *Journal of Geophysical Research: Oceans*.

Georgiou, S., **Ypma, S.L.**, Brüggemann, N., Sayol, J.M., Pietrzak, J.D., Katsman, C. A. (2020): Pathways of the water masses exiting the Labrador Sea: The importance of boundary-interior exchanges. *Ocean Modelling*, 101623.

Georgiou, S., van der Boog, C.G., Brüggemann, N., **Ypma, S.L.**, Pietrzak, J.D., Katsman, C. A. (2019): On the interplay between downwelling, deep convection and mesoscale eddies in the Labrador Sea. *Ocean Modelling*, 135, 56–70.



## ABOUT THE AUTHOR

Stefanie (Steffie) Leonore Ypma was born in Wijchen, the Netherlands, on the 7th of March 1991. From 2003 until 2009 she attended the Stedelijk Gymnasium in Nijmegen. In 2012 she obtained her BSc degree in Physics from Leiden University and finished the Practicum Musicae in piano at the Royal Conservatoire The Hague. In 2015 she received her MSc degree in Meteorology, Physical Oceanography and Climate from Utrecht University. For her master thesis, she visited the Climate Change Research Centre in Sydney, Australia, to study the separation of the East Australian Current, which resulted in her first publication. Due to the positive experiences during her masters, she decided to stay in academia and start a PhD position at Delft University of Technology where she studied the dynamics of the Nordic Seas. During that time she also followed courses from the Science Education track at TU Delft and did an internship at the Alberdingk Thijm College in Hilversum as a Physics teacher.

In March 2020, Steffie started as a postdoctoral researcher at Utrecht University to work on the development of a tool to effectively clean-up beaches by predicting where and when marine plastic debris washes ashore.

